Managing Uncertainties in Legged Robots

Nahuel Villa

Communauté
UNIVERSITÉ Grenoble Alpes

THÈSE

Pour obtenir le grade de

DOCTEUR DE LA COMMUNAUTÉ UNIVERSITÉ GRENOBLE ALPES

Spécialité : **Automatique-Productique**

Arrêté ministériel : 7 août 2006

Présentée par

Nahuel Alejandro Villa

Thèse dirigée par **Bernard Brogliato**
et co-encadrée par **Pierre-Brice Wieber**

préparée au sein **de l'INRIA**
dans **l'École Doctorale EEATS**

Managing Uncertainties in Legged Robots

Thèse soutenue publiquement le **20 Dec 2019**,
devant le jury composé de :

Nicolas Mansard
Directeur de Recherche LAAS-CNRS, Président
Christine Chevallereau
Directrice de recherche CNRS, Directrice adjointe du LS2N, Rapporteur
Daniel Limón Marruedo
Full Professor at Seville University, Examinateur
Mirko Fiacchini
Chargé de recherche Gipsa-Lab, Examinateur
Bernard Brogliato
Directeur de Recherche INRIA, Directeur de thèse
Pierre-Brice Wieber
Chargé de Recherche INRIA, Co-encadrant de thèse

Abstract

Legged robots have a huge potential field of application that ranges from routine and dangerous works, to help in the treatment of children with autism. Nevertheless, employing these complex machines on a real application requires safety guarantees on their functioning. This is traditionally approached by over-sizing the robot design, but, since how resources should be distributed is unknown, these robots are still quite restricted in their capabilities, yet without formal safety guarantees and too expensive for most simple tasks. A quantitative analysis to determine how fast and precise, and therefore how expensive should sensors, actuators and computers be has never been investigated in the existing scientific literature. There is a long theoretical and practical work to be done in this regard and it is the goal of this thesis to initiate this discussion.

Based on concepts from robust control theory, considering bounded uncertainties, we propose to quantify the effect of main sources of uncertainty on the balance control of the center of mass of the robot, since it is unstable and fundamental to develop any other task. As a first result, we established conditions to ensure the safe balance of the robot. Then, we provided control choices to reduce the restrictiveness on the motion of the robot and its cost.

Résumé

Les robots à pattes ont un énorme champ d'applications potentiel, allant des travaux routiniers et dangereux, à l'assistance comme intermédiaires rassurants entre des enfants autistes et leur entourage. Cependant, l'utilisation de ces machines complexes requiert des garanties de sécurité sur leur fonctionnement. Ceci est traditionnellement abordé en sur-dimensionnant la conception du robot. Toutefois, comme la répartition des ressources est inconnue, leurs capacités sont encore assez limitées, sans garanties de sécurité formelles et trop coûteux pour la plupart des tâches simples. Une analyse quantitative visant à déterminer la rapidité et la précision, et donc le coût, des capteurs, des actionneurs et des calculateurs n'a jamais été étudiée dans la littérature scientifique existante. Il y a là tout un travail théorique et pratique qui reste à réaliser et le but de cette thèse est d'initier cette discussion.

Sur la base des concepts de la théorie du contrôle robuste, prenant en compte des incertitudes bornées, nous proposons de quantifier l'effet des principales sources d'incertitude sur le contrôle de l'équilibre du centre de gravité du robot, car il est instable et fondamental pour développer toute autre tâche. Comme premier résultat, nous avons déterminé les conditions nécessaires pour assurer l'équilibre du robot en toute sécurité. Ensuite, nous fournissons des choix de contrôle pour réduire le caractère restrictif du mouvement du robot et de son cout.

Acknowledgements

With this thesis report, I conclude my PhD research, which I had the chance and honor to develop at Inria Grenoble-Rhône-Alpes during the last 3 years.

I want to express my thankfulness to all the people that supported and helped me during this period of my life. In particular, I want to thank my PhD advisor Pierre-Brice Wieber for his patience when I was a newcomer in this field, and for his clear guidance preventing me from waste time and effort on pointless problems, but still allowing me to freely develop my own ideas.

My office mates and friends Nestor Bohorquez and Matteo Ciocca were always willing to discuss and help on all kind of problems inside and outside the equations, which I really appreciate. I am also grateful to Diane Courtiol, for her administrative assistance with all issues related to being in a foreign country, which are beyond her liability, and made a difference to me.

I want to express my gratitude to Johannes Englsberger and Stéphane Caron for long and fruitful scientific discussions, and to my *comité de suivi:* Nicolas Mansard and Christine Chevallereau for their valuable feedback and effort in evaluating the evolution of this work each year.

Aside from research, during this thesis, I married Maribel, whom I thank for twelve years of sincere love and support. I also want to give thanks to my friends in Grenoble, in Argentina and dispersed around the word for all the time they have dedicated to me.

Finally, thanks to my family for the values and priorities they have impressed on me from the first moment.

Contents

List of Figures

List of Acronyms

cCoP compensated Center of Pressure
CoF Center of Foot
CoM Center of Mass
CoP Center of Pressure
CPU Central Processing Unit
DCM Divergent Component of the Motion
DLR German Aerospace Center
IMU Inertial Measurement Unit
MPC Model Predictive Control
QP Quadratic Program
RPI Robust Positively Invariant
SQP Series Quadratic Programming
WBC Whole Body Controller
WCS Worst-Case Sequence

Chapter 1

Introduction

1.1 Context and motivation

Biped and quadruped robots are facing today a transition to become a versatile tool with applications in entertainment [Nakaoka 2011, Ramos 2015], manufacturing [Bolotnikova 2017] and providing services [Kemp 2008, Pandey 2014], among others. This year (2019) alone, the EU project Comanoid demonstrated successfully that biped robots could soon be employed on aircraft manufacturing operations at an Airbus civilian airliner plant [Kheddar 2019]; Anybotics started the commercialization of its quadruped robot ANYmal C employed for autonomous industrial inspection [Gehring 2019]; and NASA is soon sending back to the International Space Station its humanoid robot Robonaut 2, after some repairs on earth, to continue testing the plausibility of using this kind of robots working alongside astronauts in the station.

A widespread practical use of legged robots requires, however, guarantees about their safety and operational performance: guaranteeing that all constraints, those imposed for balance and the task-specific ones, are always satisfied.

The dynamics of the Center of Mass (CoM) of these robots over the support feet is unstable, and therefore very sensitive to all sources of uncertainty, which abound: noisy sensors, inaccurate actuators, unmodeled dynamics, unexpected environment interactions, *etc.* This results in tracking errors when trying to follow a given reference motion which can easily lead to a failure: malfunctioning, objectives not achieved, loss of balance, *etc.* In research prototypes, the risk of failure is usually contained using very fast and precise (and therefore, very expensive) sensors, actuators and computers, resulting in robots that are too expensive for commercial purposes, and yet without safe operation guarantees. In order to account for the tracking error, the reference motion is normally tightened using hand tuned safety margins, which results either over-restrictive (as in [Feng 2016b] where point feet are assumed for the robot Atlas) or unsafe.

Assuming bounded uncertainties and introducing the key concept of Robust Positively Invariant (RPI) sets, we ensure a bounded tracking error and precisely specify such bound. So, with a corresponding adaptation of the reference motion, we can guarantee the safe operation of the robot.

Since the tracking error bound is linearly related to the uncertainty bound, a bigger uncertainty produces bigger tracking errors and, therefore, the safety guarantees require a more restricted reference motion. Studying this relation between bounds, we propose control choices to minimize it, allowing for less constrained motions, handling of larger uncertainty sources or reduction of the cost of the robot.

1.2 Contribution

In this thesis, we implement tools from the robust control theory to guarantee a safe operation of legged robots while reducing the resources required for such purpose.

- In order to identify and reduce uncertainty sources, we worked with the complete non-linear CoM dynamics. We showed that it can be linearized without approximations by a simple change of variables, relying on the Whole Body Controller (WBC) to compensate for the non-linear part (Sections 2.3 and 3.3).
- We obtained analytical expressions for the tracking error bound (Chapter 4). As a consequence of this:
  - We proposed feedback gains to minimize the relation between uncertainty and tracking error bounds, allowing for less constrained motions, handling of larger uncertainty sources or reduction of the robot cost (Sections 5.3.2 and 5.5.2).
  - We analyzed the sensitivity of the tracking error to the system parameters, obtaining that it is independent of the sampling period and is weakly related to the ground interaction compliance (Sections 5.3.3 and 5.5.2).
  - We obtained the sequence of disturbances that maximizes the tracking error for any choice of feedback gain (Sections 4.4.1.2 and 4.4.2.2).
  - We obtained analytically the vertices of the minimum RPI set (Sections 4.4.1.5 and 4.4.2.2).
- Using the initial constraint proposed in [Mayne 2005] for a robust MPC scheme, which is new in the context of legged robots, we ensured a bounded tracking error. Thanks to this bound, we stated conditions to guarantee the safe operation of the robot (Sections 4.5 and 6.3.4).

1.2.1 List of publications

The work on this thesis resulted in a publication in a peer-reviewed journal:

- N. A. Villa, J. Englsberger and P.-B. Wieber. *Sensitivity of legged balance control to uncertainties and sampling period.* IEEE Robotics and Automation Letters (RA-L), vol. 4, no. 4, pages 3665–3670, 2019

  Also accepted on the 2019 IEEE/RSJ International Conference on Intelligent Robots and Systems (IROS)

And a publication in a peer-reviewed conference:

- N. A. Villa and P.-B. Wieber. *Model predictive control of biped walking with bounded uncertainties.* In IEEE-RAS International Conference on Humanoid Robotics (Humanoids), pages 836–841, 2017

1.3 Outline

This thesis is composed of 5 main Chapters 2-6, a conclusive Chapter 7 and appendices. We introduce the dynamical model of the robot on Chapter 2. Then, in Chapter 3 we present an overview of our control scheme and the main sources of uncertainty affecting it. The effect from uncertainties on the tracking error is detailed and bounded analytically in Chapter 4, where we also discuss how to improve the robot capability to manage bigger uncertainties and generate less restrictive motions while keeping safety guarantees. In Chapter 5, we choose feedback gains to minimize the impact from uncertainty, and we analyse the sensitivity of the

resulting closed-loop system to sampling period and ground interaction compliance, which we validate experimentally using the robot Toro. In chapter 6, we describe our MPC scheme to generate the reference motion including an initial constraint to ensure a bounded tracking error.

1.4 Notations

Scalars, Vectors and Matrices

- Scalars are denoted using the standard italic font: N, n.
- Vectors and matrices are denoted by letters in a bold font: $\boldsymbol{x}$, $\boldsymbol{A}$.
- Sequences of scalars or vectors stacks the elements vertically in a vector as:

$$\boldsymbol{U} = \langle u_1, \ldots, u_n \rangle \equiv \begin{bmatrix} u_1 \\ \vdots \\ u_n \end{bmatrix}, \quad \boldsymbol{X} = (\boldsymbol{x}_1, \ldots, \boldsymbol{x}_n) \equiv \begin{bmatrix} \boldsymbol{x}_1 \\ \vdots \\ \boldsymbol{x}_n \end{bmatrix}. \tag{1.1}$$

- $\boldsymbol{I}$ – is the identity matrix of order $n \times n$ according to the context.
- $\boldsymbol{0}$ – is the matrix of zeros of order $n \times m$ according to the context.
- $\boldsymbol{M}_{\mathtt{c},i}$ the i-th column of the matrix $\boldsymbol{M}$
- $\boldsymbol{M}_{\mathtt{r},i}$ the i-th row of the matrix $\boldsymbol{M}$
- When several subscripts collide, we separate them with a dot: $p^{c}_{des \cdot ref}$

Sets

- Sets are denoted using the calligraphic font: $\mathcal{C}, \mathcal{P}, \mathcal{V}$
- Special number sets are denoted using blackboard bold font: $\mathbb{R}$, $\mathbb{N}$.
- $\mathbb{R}$ is the set of real numbers.
- $\mathbb{N}$ is the set of natural numbers.
- $\mathbb{R}^n$ is the set of real-valued vectors.
- $\mathbb{R}^{n \times m}$ is the set of real-valued matrices.

Functions

- Function names in mathematical expressions are written in the regular roman font: $\mathrm{sign}(q)$, $\cosh(\omega\tau)$.
- The norm L_2 in vectors and the absolute value in scalars are denoted as: $|\boldsymbol{f}|$, $|q|$.
- The angle between vectors is denoted as: $\angle(\boldsymbol{L}, \boldsymbol{B})$.

Sign Convention

- Current values are denoted without any additional notation: $\boldsymbol{x}$, u.
- Estimated, approximated or commanded values are denoted with a prime: $\boldsymbol{x}'$, u'.
- Error or disturbance values are denoted using a hat: $\hat{\boldsymbol{x}}$, $\hat{u}$.
- Errors are defined with their positive sign as:

$$\hat{\boldsymbol{x}} = \boldsymbol{x} - \boldsymbol{x}', \qquad \hat{u} = u - u'.$$

- Reference values are denoted with the subindex: $\boldsymbol{x}_{ref}$, u_{ref}.
- Tracking error values are denoted with a tilde: $\tilde{\boldsymbol{x}}$, $\tilde{u}$.
- Tracking errors are defined with their positive sign as:

$$\tilde{\boldsymbol{x}} = \boldsymbol{x} - \boldsymbol{x}_{ref}, \qquad \tilde{u} = u - u_{ref}. \tag{1.2}$$

Chapter 2

Biped Robot Modeling

2.1 Introduction

Humanoids and legged robots in general are complex machines with tens of degrees of freedom that must be precisely coordinated to develop the physical interactions required for useful tasks. We present in this chapter a brief overview of these machines focusing on the control issues that are relevant for the following chapters.

We describe briefly the Lagrangian mechanics of these robots and its limitations in Sec. 2.2. The effects of external forces on the robot as a whole are presented in Sec. 2.3, formulated in terms of the Center of Mass (CoM). We comment the dynamical implications of common scenarios in Sec. 2.3.1 and we describe the CoM restrictions in Sec. 2.3.2.

2.2 Robot Mechanics

A legged robot can be described mechanically as a kinematic chain of N actuated joints connecting $N+1$ links, where no link is fixed to the global reference frame, so that the robot can move freely in its 3D environment. The complete vector of independent generalized coordinates

$$\boldsymbol{q} = \begin{bmatrix} \boldsymbol{q}_j \\ \boldsymbol{\rho} \\ \boldsymbol{\theta} \end{bmatrix} \tag{2.1}$$

can be described by a vector of joint positions $\boldsymbol{q}_j \in \mathbb{R}^N$ that determines the robot posture, and the global position $\boldsymbol{\rho} \in \mathbb{R}^3$ and orientation $\boldsymbol{\theta} \in \mathbb{R}^3$ of a reference frame attached to some part of the robot.

Joints are normally equipped with rotary actuators to change the robot's posture by introducing a vector of joint torques $\boldsymbol{\eta} \in \mathbb{R}^N$. The final motion of the robot is also affected by interaction forces $\boldsymbol{f}_i \in \mathbb{R}$ between the environment and the i-th link, inertial effects $\boldsymbol{N} \in \mathbb{R}^{N+6}$ (as Coriolis and centrifugal forces) and the gravity acceleration $\boldsymbol{g} \in \mathbb{R}^3$ [Hurmuzlu 2004, Wieber 2016, Englsberger 2016]

$$\boldsymbol{M}(\boldsymbol{q}) \left(\begin{bmatrix} \ddot{\boldsymbol{q}}_j \\ \ddot{\boldsymbol{\rho}} \\ \ddot{\boldsymbol{\theta}} \end{bmatrix} + \begin{bmatrix} 0 \\ \boldsymbol{g} \\ 0 \end{bmatrix} \right) + \boldsymbol{N}(\boldsymbol{q}, \dot{\boldsymbol{q}}) = \begin{bmatrix} \boldsymbol{\eta} \\ 0 \\ 0 \end{bmatrix} + \sum_i \boldsymbol{J}_i(\boldsymbol{q}) \boldsymbol{f}_i, \tag{2.2}$$

where $\boldsymbol{M} \in \mathbb{R}^{(N+6)\times(N+6)}$ is the generalized inertia matrix of the robot and $\boldsymbol{J}_i$ is the Jacobian matrix formulated in [Wieber 2006a] for each link.

Since the joint actuation $\boldsymbol{\eta}$ cannot affect directly the global position $\boldsymbol{\rho}$ and orientation $\boldsymbol{\theta}$, the robot locomotion requires using external forces. As usual for legged robots, we consider

that such external forces are supplied by the contact between the feet and the ground. Though other parts of the robot can also produce a helpful support depending on the situation [Sherikov 2015] and even other kind of external forces, such as jet propulsion, could be used to generate the robot locomotion [Pucci 2017].

Contact forces can only be exerted when some link of the robot has established a contact with some surface in the environment. This condition can be modeled as the complementarity problem [Hurmuzlu 2004]:

$$\delta_k \boldsymbol{f}_k = 0, \qquad \text{with} \qquad \delta_k \geq 0, \quad |\boldsymbol{f}_k| \geq 0, \tag{2.3}$$

where the distance between contact surfaces δ_k indicates whether the contact has been accomplished ($\delta_k = 0$) or not ($\delta_k > 0$) for the k-th contact force $\boldsymbol{f}_k$ on some link.

Contact forces with the ground are usually unilateral: the force component $\boldsymbol{f}_k^{\perp}$ orthogonal to the surface can push but not pull on the ground,

$$\boldsymbol{f}_k^{\perp} \geq 0. \tag{2.4}$$

And in order to avoid foot slipping, the tangential component $\boldsymbol{f}_k^{\parallel}$ must satisfy [Wieber 2016]

$$|\boldsymbol{f}_k^{\parallel}| \leq \mu_k \boldsymbol{f}_k^{\perp}, \tag{2.5}$$

where μ_k is the friction coefficient of the k-th contact interaction.

The contact forces required for the robot balance and locomotion can only be controlled indirectly through the coordinated actuation of joints producing some appropriate sequence of postures. According to the desired motion, the robot is controlled to stand, balancing its body with a given ground contact; or to walk, establishing and interrupting ground contacts cyclically [Sherikov 2016].

Any robot motion is restricted to postures $\boldsymbol{q}_j$ without interpenetration of the robot parts, joint torques $\boldsymbol{\eta}$ within the motor limitations, links with unalterable sizes (rigid body links) and other limitations of the robot hardware that introduce control restrictions of the form [Sherikov 2016, Feng 2016a]:

$$\underline{\phi} \leq \phi(\boldsymbol{q}, \dot{\boldsymbol{q}}, \ddot{\boldsymbol{q}}, \boldsymbol{\eta}) \leq \overline{\phi} \tag{2.6}$$

where ϕ is an application-dependent function with lower $\underline{\phi}$ and upper $\overline{\phi}$ limits defined by the hardware restrictions.

When a foot reaches the ground to establish a new contact point, an impact occurs. Such impact is normally modeled assuming an instantaneous collision on a rigid surface and its effects are estimated using a collision mapping [Westervelt 2018, Hurmuzlu 2004]:

$$\dot{\boldsymbol{q}}^{-} \longmapsto \dot{\boldsymbol{q}}^{+}, \tag{2.7}$$

that relates the robot velocities just before $\dot{\boldsymbol{q}}^{-}$ and just after $\dot{\boldsymbol{q}}^{+}$ the impact. This behavior with finite jumps in the velocity corresponds to a hybrid dynamics.

2.3 Center of Mass Dynamics

The behavior of the robot affected by external forces can be approached more simply by considering its Center of Mass (CoM) $\boldsymbol{c}$ defined as the weighted sum:

$$\boldsymbol{c} \equiv \frac{\sum_{i=1}^{\mathrm{N+1}} \boldsymbol{l}_i m_i}{\sum_{i=1}^{\mathrm{N+1}} m_i}, \tag{2.8}$$

where m_i and $\boldsymbol{l}_i$ are the mass and position of the CoM of the i-th link. We can obtain the contact forces required to balance and drive the robot around its environment from Newton and Euler equations of the robot motion with respect to its CoM $\boldsymbol{c}$ [Wieber 2006a]:

$$\sum_k \boldsymbol{f}_k = m\ddot{\boldsymbol{c}} + m\boldsymbol{g} - \boldsymbol{f}_\mathrm{e} \tag{2.9}$$

$$\sum_k (\boldsymbol{r}_k - \boldsymbol{c}) \times \boldsymbol{f}_k = \dot{\boldsymbol{L}} - \boldsymbol{\eta}_\mathrm{e}, \tag{2.10}$$

where we have separated the forces $\boldsymbol{f}_k$ exerted at the ground contact points $\boldsymbol{r}_k$ and the rest of external wrenches $\boldsymbol{f}_\mathrm{e}$, $\boldsymbol{\eta}_\mathrm{e}$, as proposed in [Agravante 2016]. $\boldsymbol{L}$ is the centroidal angular momentum of the entire robot and m is its total mass. Combining these equations we obtain:

$$\sum_k \boldsymbol{r}_k \times \boldsymbol{f}_k = \boldsymbol{c} \times (m\ddot{\boldsymbol{c}} + m\boldsymbol{g} - \boldsymbol{f}_\mathrm{e}) + \dot{\boldsymbol{L}} - \boldsymbol{\eta}_\mathrm{e}. \tag{2.11}$$

Let's adopt Cartesian coordinate axes ^{x,y,z} with origin on the contact surface of one foot on the ground and the axis ^{z} normal to it, and separate the torque introduced by the contact forces as:

$$\sum_k \boldsymbol{r}_k \times \boldsymbol{f}_k = \sum_k \left(\begin{bmatrix} r_k^y \\ -r_k^x \\ 0 \end{bmatrix} f_k^z - \begin{bmatrix} f_k^y \\ -f_k^x \\ 0 \end{bmatrix} r_k^z + \begin{bmatrix} 0 \\ 0 \\ r_k^x f_k^y - r_k^x f_k^y \end{bmatrix} \right), \tag{2.12}$$

where the first term is related to the pressure distribution f_k^z on the contact surface; the second term is related to the unevenness of the ground (it is zero when the contact surface is a plane so $r_k^z = 0$, but can become relevant when climbing stairs); and the third one, normal to the contact surface, is used to control the robot orientation.

Rewriting the pressure distribution f_k^z in terms of the Center of Pressure (CoP) $\boldsymbol{p}$, that is defined as the point on the contact surface where we can concentrate the distributed pressure as a single force $\sum f_k^z$ that produce the same torque as the original distribution [Sardain 2004]:

$$\boldsymbol{p}^{x,y} \sum_k f_k^z \equiv \sum_k \boldsymbol{r}_k^{x,y} f_k^z, \tag{2.13}$$

and dividing all the expression (2.11) by the ^{z} coordinate of the Newton equation (2.9), we can obtain the ^{x,y} coordinates of the CoM dynamics [Wieber 2016]:

$$\boldsymbol{p}^{x,y} = \boldsymbol{c}^{x,y} - \frac{(m\ddot{\boldsymbol{c}}^{x,y} + m\boldsymbol{g}^{x,y} - \boldsymbol{f}_\mathrm{e}^{x,y})c^z}{m\ddot{c}^z + mg^z - f_\mathrm{e}^z} + \frac{\boldsymbol{S}(\dot{\boldsymbol{L}}^{x,y} - \boldsymbol{\eta}_\mathrm{e}^{x,y})}{m\ddot{c}^z + mg^z - f_\mathrm{e}^z} + \frac{\sum_k r_k^z \boldsymbol{f}_k^{x,y}}{\sum_k f_k^z}, \tag{2.14}$$

with a $\frac{\pi}{2}$ rotation matrix $\boldsymbol{S} = \left[\begin{smallmatrix} 0 & -1 \\ 1 & 0 \end{smallmatrix}\right]$. We rearrange this expression to emphasize the linear relation between CoM acceleration $\ddot{\boldsymbol{c}}$ and CoP $\boldsymbol{p}$:

$$\ddot{\boldsymbol{c}}^{x,y} = \omega^2(\boldsymbol{c}^{x,y} - \boldsymbol{p}^{x,y} + \boldsymbol{n}^{x,y}), \tag{2.15}$$

with some constant value $\omega^2 \approx \frac{g^z}{c^z}$, gathering all non-linearities in the vector:

$$\boldsymbol{n}^{x,y} \equiv \frac{\ddot{\boldsymbol{c}}^{x,y}}{\omega^2} - \frac{(m\ddot{\boldsymbol{c}}^{x,y} + m\boldsymbol{g}^{x,y} - \boldsymbol{f}_\mathrm{e}^{x,y})c^z}{m\ddot{c}^z + mg^z - f_\mathrm{e}^z} + \frac{\boldsymbol{S}(\dot{\boldsymbol{L}}^{x,y} - \boldsymbol{\eta}_\mathrm{e}^{x,y})}{m\ddot{c}^z + mg^z - f_\mathrm{e}^z} + \frac{\sum_k r_k^z \boldsymbol{f}_k^{x,y}}{\sum_k f_k^z}. \tag{2.16}$$

Rewriting this expression as a system of two first order differential equations with the change of variables

$$\boldsymbol{\zeta}^{x,y} \equiv \boldsymbol{c}^{x,y} - \frac{\dot{\boldsymbol{c}}^{x,y}}{\omega}, \tag{2.17}$$

$$\boldsymbol{\xi}^{x,y} \equiv \boldsymbol{c}^{x,y} + \frac{\dot{\boldsymbol{c}}^{x,y}}{\omega}, \tag{2.18}$$

we obtain the modal form

$$\dot{\boldsymbol{\zeta}}^{x,y} = \omega(\boldsymbol{p}^{x,y} - \boldsymbol{n}^{x,y} - \boldsymbol{\zeta}^{x,y}), \tag{2.19}$$

$$\dot{\boldsymbol{\xi}}^{x,y} = \omega(\boldsymbol{\xi}^{x,y} - \boldsymbol{p}^{x,y} + \boldsymbol{n}^{x,y}), \tag{2.20}$$

where $\boldsymbol{\zeta}^{x,y}$ converges to $\boldsymbol{p}^{x,y} - \boldsymbol{n}^{x,y}$, and $\boldsymbol{\xi}$, the so called Divergent Component of the Motion (DCM) [Takenaka 2009], diverges away from $\boldsymbol{p}^{x,y} - \boldsymbol{n}^{x,y}$ constituting an unstable dynamics. We can see, moreover, reorganizing (2.18) that the CoM is attracted by the DCM:

$$\dot{\boldsymbol{c}}^{x,y} = \omega(\boldsymbol{\xi}^{x,y} - \boldsymbol{c}^{x,y}). \tag{2.21}$$

2.3.1 Common Scenarios

In practical applications of legged robots, it may be required to walk on slopes (having non-zero $\boldsymbol{g}^{x,y}$) or on uneven terrains (having non-zero $\sum_k r_k^z \boldsymbol{f}_k^{x,y}$). In these cases the lateral acceleration $\boldsymbol{g}^{x,y}$ and torque $\sum_k r_k^z \boldsymbol{f}_k^{x,y}$ are bounded, can be easily estimated using the robot sensors, and the friction forces $\boldsymbol{f}_k^{x,y}$ can be controlled to stabilize the motion.

External forces, on the other hand, are not bounded, but we assume that the robot is controlled to handle tools and objects requiring bounded wrenches $\boldsymbol{f}_\mathrm{e}$, $\boldsymbol{\eta}_\mathrm{e}$, as well as avoiding collisions and dangerous places [Bohórquez 2016].

For several applications we can expect the robot to spend most of the time walking in a simple scenario where the ground is flat ($r_k^z = 0$) and horizontal ($\boldsymbol{g}^{x,y} = 0$), without additional external wrenches ($\boldsymbol{f}_\mathrm{e} = 0$, $\boldsymbol{\eta}_\mathrm{e} = 0$), resulting in

$$\boldsymbol{n}^{x,y} = \frac{\ddot{\boldsymbol{c}}^{x,y}}{\omega^2} - \frac{c^z}{\ddot{c}^z + g^z}\ddot{\boldsymbol{c}}^{x,y} + \frac{\boldsymbol{S}\dot{\boldsymbol{L}}^{x,y}}{m(\ddot{c}^z + g^z)}, \tag{2.22}$$

where the angular momentum variation $\dot{\boldsymbol{L}}$ and CoM vertical motion $\ddot{c}^z$ are bounded [Herr 2008, Brasseur 2015], can be easily estimated, and $\dot{\boldsymbol{L}}$ can be introduced by moving the body to stabilize the motion [Lee 2012].

Standing still is an even simpler but also common condition. In such case the vector $\boldsymbol{n}^{x,y}$ vanishes, resulting in a CoM linearly related to the CoP [Wieber 2016]

$$\ddot{\boldsymbol{c}}^{x,y} = \omega^2(\boldsymbol{c}^{x,y} - \boldsymbol{p}^{x,y}), \tag{2.23}$$

corresponding to the model of a linear inverted pendulum which has also been experimentally validated for the balance of human beings while standing [Winter 1998]. Since the non-linear effects $\boldsymbol{n}$ are bounded, and because of the simplicity and linearity of this relation, it is normally used for the control of legged robots even in walking scenarios (neglecting $\dot{\boldsymbol{L}}^{x,y}$ and $\ddot{c}^z$) [Englsberger 2011, Kajita 2010] obtaining good results even in presence of perturbations [Choi 2006, Feng 2016b, Wieber 2006b].

2.3.2 Restrictions on the Center of Mass Dynamics

From the CoM dynamics computation we obtain the forces required for the robot locomotion and its associated whole-body kinematics

$$\dot{\boldsymbol{c}} = \boldsymbol{J}_{CoM}\dot{\boldsymbol{q}}, \tag{2.24}$$

using a Jacobian matrix $\boldsymbol{J}_{CoM}$ [Sugihara 2002] based on the CoM definition (2.8). Then, from an inverse dynamics problem [Sherikov 2016], we can obtain the required joint torques $\boldsymbol{\eta}$. In consequence, for the feasibility of the CoM motion, it must agree with the whole-body hardware restrictions and with the limitations of each physical interaction.

Considering the unilaterality of contact forces (2.4), the CoP is bound to the convex hull $\mathcal{P}$ of the contact points as can be easily noticed from its definition (2.13) [Wieber 2016]:

$$\boldsymbol{p}^{x,y} = \frac{\sum_k \boldsymbol{r}_k^{x,y} f_k^z}{\sum_k f_k^z} \in \mathcal{P}(\boldsymbol{s}_k). \tag{2.25}$$

The size and shape of this set, that we call support polygon, varies depending on the position and orientation of the feet $\boldsymbol{s}_k$ on the ground.

We control the robot to always maintain at least one foot on the ground. The placement of new steps must respect some minimum distance from the foot currently on the ground in order to avoid self collisions (2.6), and a maximum distance related to leg length (2.6), constraining new step placements $\boldsymbol{s}^{x,y}$ to some stepping area [Herdt 2010]:

$$\boldsymbol{s}^{x,y} \in \mathcal{S}(\boldsymbol{s}_k). \tag{2.26}$$

The maximum leg length also determines a maximum distance between the CoM and the feet on the ground [Brasseur 2015]:

$$\boldsymbol{c}^{x,y} \in \mathcal{C}(\boldsymbol{s}_k). \tag{2.27}$$

Other restrictions can also be considered such as limits on CoM velocity and acceleration $\dot{\boldsymbol{c}}^{x,y}$, $\ddot{\boldsymbol{c}}^{x,y}$ introduced by the limited joint torques [Grandia 2019] and friction forces [Caron 2015] $\boldsymbol{f}_k^{x,y}$ (2.5), or task specific constraints such as avoiding obstacles [Bohórquez 2016, Ciocca 2019].

2.4 Conclusion

We have presented a general overview of the physics involved in legged robots. We have introduced the concept of CoM, reaching an exhaustive expression for its dynamics, and we presented the CoM restrictions related to the robot hardware and its interactions with the environment.

Chapter 3

Control and Uncertainty

3.1 Introduction

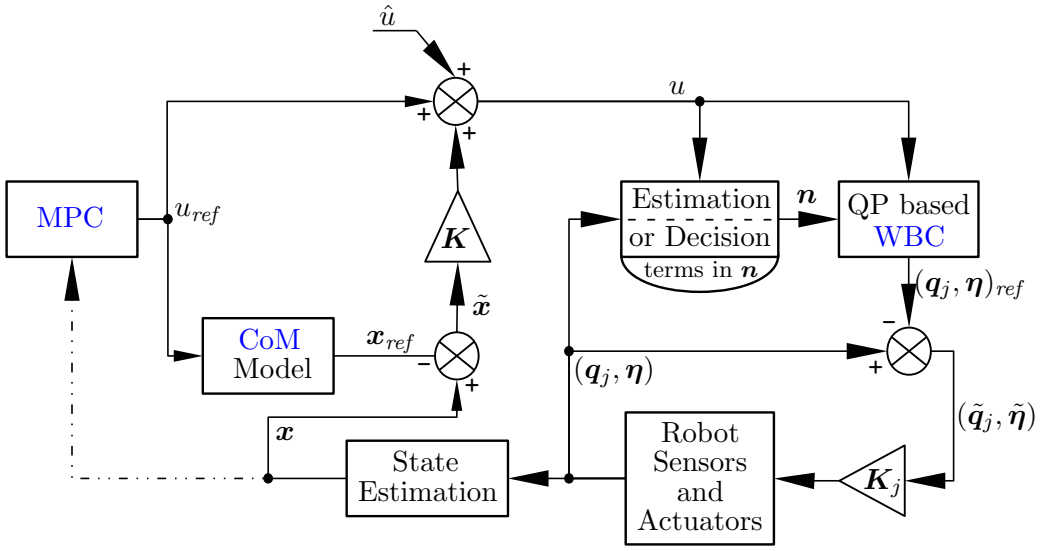

Figure 3.1: Control scheme. This general layout is presented in the current chapter describing its main sources of uncertainty $\hat{u}$. In Ch. 4 we determine a precise bound for the tracking error $\tilde{\boldsymbol{x}}$. In Ch. 5 we study the election of feedback gains $\boldsymbol{K}$ aiming to minimize the tracking error bound. In Ch. 6 we propose an MPC reference generation scheme $(u_{ref}, \boldsymbol{x}_{ref})$, and we propose a safe form to close the reference generation loop (dashed connection).

The goal of this chapter is to present our CoM control scheme shown in Fig. 3.1, and the main sources of uncertainty affecting it. The structure of joint actuators and the interaction with the ground determine our capability to control contact forces. Considering typical configurations, the CoP can be controlled directly or indirectly as discussed in Sec. 3.2. Controlling directly the difference $\boldsymbol{p} - \boldsymbol{n}$, we obtain a linear CoM dynamics in Sec. 3.3. This requires controlling or estimating the terms in $\boldsymbol{n}$ and, therefore, is subject to some uncertainty. In Sec. 3.4 we rewrite the control system in discrete form to match the digital instruments used for the internal signal communication. In order to track a reference motion, considering all sources of uncertainty, we propose in Sec. 3.5 a feedback control law and show its closed-loop stability conditions. In Sec. 3.5.1, we introduce a standard Smith predictor to deal with delays between the state estimation and the control execution.

3.2 Types of Actuation

Considering physical applications, we expect legged robots to manipulate tools [Okada 2006], carry heavy objects while cooperating with humans or other robots [Agravante 2016], reach target places avoiding all sort of obstacles [Bohórquez 2016, Brossette 2017], etc. During their normal operation, the robots must exert precise contact forces to balance all the environment interactions and follow some desired motion.

These robots control forces from interactions with the environment through the coordinated actuation of joints. Thus, precision in such an indirect control requires both precise control of joint actuation [Semini 2011] and a detailed knowledge of the interaction dynamics [Grandia 2019].

Looking for the capability to determine directly every joint torque $\boldsymbol{\eta}$ (in so-called *torque-controlled* robots), several joint control architectures have been proposed in the literature. Strengths and weakness of hydraulic, pneumatic and electric based joints in terms of force actuation are discussed in [Hutter 2016, Englsberger 2014, Pratt 2002].

Normally, a rigid ground is assumed for the contact interaction, it means that unilateral forces of arbitrary magnitude can be instantaneously exerted within the support polygon $\mathcal{P}$. Many indoor applications of legged robots, such as bringing supplies in industrial plants, could match with this assumption. Considering also a torque controlled robot, allows us to control directly the CoP in the dynamics (2.15) that we repeat here in scalar form

$$\ddot{c} = \omega^2(c - p + n), \tag{3.1}$$

valid for any ^{x} or ^{y} coordinate, since they are uncoupled and present identical dynamics. We write, then, the control system $\mathbf{P}\rightarrow\mathbf{C}\dot{\mathbf{C}}$:

$$\frac{d}{dt}\begin{bmatrix} c \\ \dot{c} \end{bmatrix} = \begin{bmatrix} 0 & 1 \\ \omega^2 & 0 \end{bmatrix}\begin{bmatrix} c \\ \dot{c} \end{bmatrix} + \begin{bmatrix} 0 \\ -\omega^2 \end{bmatrix}(p - n). \tag{3.2}$$

Or considering only the DCM (2.18), we obtain the system $\mathbf{P}\rightarrow\mathbf{X}$:

$$\dot{\xi} = \omega\xi - \omega(p - n). \tag{3.3}$$

Other robot architectures implement the joint actuation by setting every joint position $\boldsymbol{q}_j$ (so-called *position controlled* robots), which in general incorporate some form of force control at the end effectors [Ibanez 2012] to manage specific interactions such as ground contact, but normally, the resulting force control loop is slow. In [Kajita 2010] a converging dynamics of the CoP

$$\dot{p} = \gamma(p_{des} - p), \tag{3.4}$$

with some desired CoP p_{des}, is proposed for a position controlled robot which relies on a compliant element in the sole to control ground contact forces. This CoP converging dynamics can also be observed in torque controlled robots [Englsberger 2015], having a much higher time parameter γ.

Unstructured environments can present more complex contact interactions with the ground [Li 2013]. When the ground is compliant, we can expect a similar converging CoP with some time varying parameter γ. So, either a slow force control loop or a compliant support ground, introduces a converging dynamics (3.4) for the CoP and results in the control system $\mathbf{P}_d\rightarrow\mathbf{C}\dot{\mathbf{C}}\mathbf{P}$:

$$\frac{d}{dt}\begin{bmatrix} c \\ \dot{c} \\ p \end{bmatrix} = \begin{bmatrix} 0 & 1 & 0 \\ \omega^2 & 0 & -\omega^2 \\ 0 & 0 & -\gamma \end{bmatrix}\begin{bmatrix} c \\ \dot{c} \\ p \end{bmatrix} + \begin{bmatrix} 0 \\ \omega^2 \\ 0 \end{bmatrix} n + \begin{bmatrix} 0 \\ 0 \\ \gamma \end{bmatrix} p_{des} \tag{3.5}$$

proposed in [Kajita 2010], or in terms of the DCM, $\mathbf{P}_d \rightarrow \mathbf{XP}$:

$$\frac{d}{dt}\begin{bmatrix}\xi\\ p\end{bmatrix} = \begin{bmatrix}\omega & -\omega\\ 0 & -\gamma\end{bmatrix}\begin{bmatrix}\xi\\ p\end{bmatrix} + \begin{bmatrix}\omega\\ 0\end{bmatrix} n + \begin{bmatrix}0\\ \gamma\end{bmatrix} p_{des} \tag{3.6}$$

proposed in [Morisawa 2012], where the control variable is the desired CoP p_{des}. For simplicity, we will consider only this second form ($\mathrm{P}_d \rightarrow \mathrm{XP}$) of the system with CoP compliance.

In the following sections we will represent generically the control input as u and the state as $\boldsymbol{x}$ for all systems.

3.2.1 Inaccurate actuation

Setting an input value u' requires all joints to move accordingly to generate a particular interaction with the ground. The inaccuracy of joint actuators produces, therefore, a mismatch between the desired contact forces and the resulting ground interaction. We can define an actual effective input u related to the current actuation as

$$u = u' + \hat{a}, \tag{3.7}$$

differing with the commanded input u' by a bounded uncertain mismatch $\hat{a}$. Typically, these inaccuracies are introduced by:

Friction: When working with small loads, joint friction can produce torques with magnitude comparable to the commanded torque producing wrong position and torque outputs.

Flexibilities: Interaction forces such as the contact with the ground produce a deformation of the robot structure introducing uncertainty in the interaction and their application point.

Backlash: Gaps in the mechanical chain require the joint motors to make some displacement without applying appreciable torque or motion of links, which delays the control action. This issue does not have a big impact in each joint since harmonic drives as well as hydraulic pumps present low backlash [Semini 2011], but its accumulated effect along all the kinematic chain can be meaningful and approaches to compensate for it has been proposed [Jung 2004].

Bandwidth: In a real motor, inertia and maximum allowed current limit the rate of change of its output torque (which measured in Hertz (Hz) is called bandwidth). Friction, flexibilities and backlash produce an even smaller effective bandwidth limit in the robot actuation.

Similarly, in a compliant terrain the contact force is not instantaneously applied, but with some finite rate. In [Grandia 2019] it is proposed a cost function to penalize rapid variations of the high level control input to be consistent with these limitations.

3.2.2 State Estimation

The robot model and sensors distributed on the robot structure are used to estimate all relevant dynamic variables such as CoM $\boldsymbol{c}$, CoP $\boldsymbol{p}$, DCM $\boldsymbol{\xi}$, non-linearities $\boldsymbol{n}$, robot posture $\boldsymbol{q}_j$, and their time derivatives.

Commonly, these robots incorporate an Inertial Measurement Unit (IMU) in the central body to measure acceleration and angular velocities of the structure, force sensors in every joint or only at the end effectors to sense interactions with the environment, and joint encoders to determine the position of each joint. Other sensors such as cameras and lidars are often included to measure the global position of the robot, and recognize dynamically the

environment. The state estimation is normally implemented using optimal observers such as Kalman filters or moving horizon estimators [Xinjilefu 2015, Mifsud 2017].

Noise in sensors, bad calibration of instruments, numerical issues and other sources of uncertainty along the estimation process results in state estimation errors $\hat{\boldsymbol{x}}$. These errors can be efficiently bounded, limiting the predicted state variation based on the robot model [Fang 2018].

3.3 Equivalent Linear Dynamics

During its normal operation, the robot produces intentional movements that impact non-linearly on the CoM dynamics, such as vertical motion c^z, $\dot{c}^z$, $\ddot{c}^z$ of the CoM while walking or climbing stairs, or external forces $\boldsymbol{f}_\text{e}$, $\boldsymbol{n}_\text{e}$ when manipulating tools. These effects n can be efficiently bounded [Brasseur 2015, Serra 2016]:

$$n \in \mathcal{N}, \tag{3.8}$$

and based on the robot sensors and the model (2.16), they can be estimated and taken into account to control the robot balance and locomotion.

Since n is known and affects the dynamics in the same form as p, we linearize all systems (3.2), (3.3), (3.5), (3.6) by introducing the change of variable

$$p^c = p - n, \tag{3.9}$$

that we call compensated CoP (cCoP). So, we obtain

$$\textbf{P}\rightarrow\textbf{C}\dot{\textbf{C}}\textbf{:} \qquad \begin{bmatrix}\dot{c}\\ \ddot{c}\end{bmatrix} = \begin{bmatrix}0 & 1\\ \omega^2 & 0\end{bmatrix}\begin{bmatrix}c\\ \dot{c}\end{bmatrix} + \begin{bmatrix}0\\ -\omega^2\end{bmatrix}p^c, \tag{3.10}$$

$$\textbf{P}\rightarrow\textbf{X}\textbf{:} \qquad \dot{\xi} = \omega\xi - \omega p^c, \tag{3.11}$$

and defining also the desired cCoP:

$$p^c_{des} = p_{des} - \left(n + \frac{\dot{n}}{\gamma}\right), \tag{3.12}$$

we have,

$$\textbf{P}_d\rightarrow\textbf{XP}\textbf{:} \qquad \begin{bmatrix}\dot{\xi}\\ \dot{p}^c\end{bmatrix} = \begin{bmatrix}\omega & -\omega\\ 0 & -\gamma\end{bmatrix}\begin{bmatrix}\xi\\ p^c\end{bmatrix} + \begin{bmatrix}0\\ \gamma\end{bmatrix}p^c_{des}. \tag{3.13}$$

Based on the estimation of n (and $\dot{n}$), the WBC is in charge of bringing the input p^c or p^c_{des} to the required values by controlling the CoP p.

We normally control the robot to maintain certain posture and move limbs as humans do, which mostly defines the value of n. Thus, the cCoP is constrained to the support polygon (2.25) shifted by n

$$p^c \in \mathcal{P} - n. \tag{3.14}$$

In some scenarios, we may have access to exert external forces $\boldsymbol{\eta}_\text{e}$, $\boldsymbol{f}_\text{e}$, $\boldsymbol{f}_k^{x,y}$ [Sherikov 2015] or modify slightly the vertical motion $\ddot{c}^z$, c^z and angular momentum $\boldsymbol{L}$. Controlling such variables for balance, we can obtain a laxer cCoP constraint:

$$p^c \in \mathcal{P} \oplus -\mathcal{N}_c - n_g, \tag{3.15}$$

where the non-linearities $n = n_c + n_g$ are separated in a bounded controlled part $n_c \in \mathcal{N}_c$ and a known given part n_g. The controlled term n_c can be decided on-line optimally using the method of Safe SQP proposed by [Bohorquez 2018]. In this thesis, however, we use the constraint (3.14) assuming that none part of n is directly controlled for balance.

3.3.1 Non-Linear Model Errors

Due to the natural lack of information in a dynamic environment, the estimated value n' of non-linear effects is missing unexpected interactions and makes a bad estimate of those partially known. Such model error $\hat{n}$ has different effects depending on the system:

P→X / P→C$\dot{\text{C}}$

The commanded cCoP is

$$p'^c = p - n' = p - n + \hat{n}, \tag{3.16}$$

so, reordering, we can observe that the actual cCoP is

$$p^c = p - n = p'^c - \hat{n}, \tag{3.17}$$

with the actuation error $-\hat{n}$.

$\mathbf{P}_d$→XP

We command a desired cCoP as

$$p'^c_{des} = p_{des} - \left(n' + \frac{\dot{n}'}{\gamma}\right) = p_{des} - \left(n + \frac{\dot{n}}{\gamma}\right) + \left(\hat{n} + \frac{\hat{\dot{n}}}{\gamma}\right), \tag{3.18}$$

so, reordering, we can observe that the actual desired cCoP is

$$p^c_{des} = p_{des} - \left(n + \frac{\dot{n}}{\gamma}\right) = p'^c_{des} - \hat{n} - \frac{\hat{\dot{n}}}{\gamma}. \tag{3.19}$$

with the actuation error $-(\hat{n} + \hat{\dot{n}}/\gamma)$.

Moreover, in this case, p^c is a state variable and $\hat{n}$ introduces the estimation error

$$\hat{p}^c = p^c - p'^c = -\hat{n}. \tag{3.20}$$

3.4 Discrete Control

Based on the linear CoM dynamics, we decide the control action u to feed the WBC through a zero-order hold circuit, which maintains the input constant during time periods τ (the sampling period). Therefore, we restrict explicitly our dynamics to piece-wise constant control actions

$$u_t = u_{i\tau} \qquad \text{for the } i\text{-th time period} \qquad i\tau \leq t < (i+1)\tau, \tag{3.21}$$

that allows us to rewrite our continuous control systems in discrete form [Ogata 1995]. Let's consider generically the system

$$\dot{\boldsymbol{x}}_t = \boldsymbol{G}\boldsymbol{x}_t + \boldsymbol{H}u_t, \tag{3.22}$$

with state $\boldsymbol{x}_t$ and system matrices $\boldsymbol{G}$ and $\boldsymbol{H}$. From this equation's solution, given $\boldsymbol{x}_{i\tau}$ at some initial time $t = i\tau$, the state $\boldsymbol{x}_{(i+1)\tau}$ after a period τ is

$$\boldsymbol{x}_{(i+1)\tau} = \mathrm{e}^{\boldsymbol{G}\tau}\boldsymbol{x}_{i\tau} + \mathrm{e}^{\boldsymbol{G}(i+1)\tau}\int_{i\tau}^{(i+1)\tau} \mathrm{e}^{-\boldsymbol{G}t}\boldsymbol{H}u_{i\tau}dt, \tag{3.23}$$

Since $\boldsymbol{G}$ is non-singular in our systems, it is:

$$\boldsymbol{x}_{(i+1)\tau} = \mathrm{e}^{\boldsymbol{G}\tau}\boldsymbol{x}_{i\tau} + (\mathrm{e}^{\boldsymbol{G}\tau} - \boldsymbol{I})\boldsymbol{G}^{-1}\boldsymbol{H}u_{i\tau}, \tag{3.24}$$

and with the change of notation:

$$\begin{aligned} \boldsymbol{A} &= \mathrm{e}^{\boldsymbol{G}\tau} \\ \boldsymbol{B} &= (\mathrm{e}^{\boldsymbol{G}\tau} - \boldsymbol{I})\boldsymbol{G}^{-1}\boldsymbol{H} \\ \boldsymbol{x} &= \boldsymbol{x}_{i\tau} \\ u &= u_{i\tau}, \end{aligned} \tag{3.25}$$

it is equivalent to

$$\boldsymbol{x}^{+} = \boldsymbol{A}\boldsymbol{x} + \boldsymbol{B}u. \tag{3.26}$$

In particular, for each formulation, we obtain the matrices:

P→CC̈

$$\boldsymbol{A} = \begin{bmatrix} \cosh(\omega\tau) & \omega^{-1}\sinh(\omega\tau) \\ \omega\sinh(\omega\tau) & \cosh(\omega\tau) \end{bmatrix}, \qquad \boldsymbol{B} = \begin{bmatrix} 1-\cosh(\omega\tau) \\ -\omega\sinh(\omega\tau) \end{bmatrix}, \tag{3.27}$$

with state and input:

$$\boldsymbol{x} = \begin{bmatrix} c \\ \dot{c} \end{bmatrix}, \qquad u = p^{c} = p - n. \tag{3.28}$$

P→X

$$A = \mathrm{e}^{\omega\tau}, \qquad B = 1 - \mathrm{e}^{\omega\tau} \tag{3.29}$$

with state and input:

$$x = \xi \qquad u = p^{c} = p - n. \tag{3.30}$$

P$_d$→XP

$$\boldsymbol{A} = \begin{bmatrix} \mathrm{e}^{\omega\tau} & \frac{\omega}{\gamma+\omega}(\mathrm{e}^{-\gamma\tau} - \mathrm{e}^{\omega\tau}) \\ 0 & \mathrm{e}^{-\gamma\tau} \end{bmatrix}, \qquad \boldsymbol{B} = \begin{bmatrix} \frac{\omega(1-\mathrm{e}^{-\gamma\tau})+\gamma(1-\mathrm{e}^{\omega\tau})}{\gamma+\omega} \\ 1-\mathrm{e}^{-\gamma\tau} \end{bmatrix}, \tag{3.31}$$

with state and input:

$$\boldsymbol{x} = \begin{bmatrix} \xi \\ p^{c} \end{bmatrix}, \qquad u = p^{c}_{des} = p_{des} - \left(n + \frac{\dot{n}}{\gamma}\right). \tag{3.32}$$

3.5 Closed-Loop Dynamics

Consider a reference motion $\boldsymbol{x}_{ref}$, u_{ref}, generated according to the robot dynamics model, using any standard motion generation scheme [Wieber 2016] (we discuss the reference motion generation in more detail in Ch. 6). Because of the uncertainties described above, we track this reference using a feedback law based on the estimated state $\boldsymbol{x}' = \boldsymbol{x} - \hat{\boldsymbol{x}}$. The resulting effective control law is:

$$u = u_{ref} + \boldsymbol{K}(\boldsymbol{x} - \boldsymbol{x}_{ref}) + \hat{u}, \tag{3.33}$$

with a feedback gain of the form

$$\boldsymbol{K} = k\begin{bmatrix}1 & \lambda\end{bmatrix} \qquad \text{for} \qquad \mathbf{P}\rightarrow\mathbf{C}\dot{\mathbf{C}} \text{ and } \mathbf{P}_d\rightarrow\mathbf{XP}, \tag{3.34}$$

$$\boldsymbol{K} = k \qquad \text{for} \qquad \mathbf{P}\rightarrow\mathbf{X}, \tag{3.35}$$

and where $\hat{u}$ groups all previously discussed uncertainties coming from actuation (Sec. 3.2.1), estimation (Sec. 3.2.2), and model errors (Sec. 3.3.1):

$\mathbf{P}\rightarrow\mathbf{C}\dot{\mathbf{C}}$	$\mathbf{P}\rightarrow\mathbf{X}$	$\mathbf{P}_d\rightarrow\mathbf{XP}$
$\hat{u} = \hat{a} - \hat{n} - \boldsymbol{K}\hat{\boldsymbol{x}}$	$\hat{u} = \hat{a} - \hat{n} - k\hat{\xi}$	$\hat{u} = \hat{a} - \hat{n} - \frac{\dot{\hat{n}}}{\gamma} - \boldsymbol{K}\hat{\boldsymbol{x}}$

so that it is bounded in a set

$$\hat{u} \in \mathcal{V}. \tag{3.36}$$

Any known (not uncertain) offset in the actuation or estimation must be taken into account as a part of the calibration of the control system, or included in the robot model as a parameter. In consequence, the set of uncertainty $\mathcal{V}$ is centered on zero.

Defining the tracking errors of state and input:

$$\tilde{\boldsymbol{x}} = \boldsymbol{x} - \boldsymbol{x}_{ref}, \qquad \tilde{u} = u - u_{ref} = \boldsymbol{K}\tilde{\boldsymbol{x}} + \hat{u}, \tag{3.37}$$

and generating the reference motion $\boldsymbol{x}_{ref}$, u_{ref} to satisfy the system dynamics (3.26)

$$\boldsymbol{x}_{ref}^{+} = \boldsymbol{A}\boldsymbol{x}_{ref} + \boldsymbol{B}u_{ref}, \tag{3.38}$$

we obtain the dynamics of the tracking error:

$$\tilde{\boldsymbol{x}}^{+} = (\boldsymbol{A} + \boldsymbol{B}\boldsymbol{K})\tilde{\boldsymbol{x}} + \boldsymbol{B}\hat{u}. \tag{3.39}$$

Notice that (in its own space of variables) the tracking error also satisfies the original system dynamics:

$$\tilde{\boldsymbol{x}}^{+} = \boldsymbol{A}\tilde{\boldsymbol{x}} + \boldsymbol{B}\tilde{u} \tag{3.40}$$

It means that, for example, the tracking error of the CoM velocity is also the velocity of the CoM tracking error $\tilde{\dot{c}} = \dot{\tilde{c}}$.

The current motion $\boldsymbol{x}$, u must satisfy all constraints (2.26), (2.27), (3.14):

$$u = u_{ref} + \tilde{u} \in \mathcal{U}, \tag{3.41}$$

$$\boldsymbol{x} = \boldsymbol{x}_{ref} + \tilde{\boldsymbol{x}} \in \mathcal{X}, \tag{3.42}$$

where the set $\mathcal{U}$ groups the constraints related to the input variable and $\mathcal{X}$ those related to the state. So, in order to ensure feasibility without over-restricting the reference motion $\boldsymbol{x}_{ref}$, u_{ref}, we will investigate more about the tracking error dynamics in the following chapters.

3.5.1 Feedback Delays

We have designed the feedback law (3.33) to produce the control action $u(\boldsymbol{x})$ required when the state is $\boldsymbol{x}$. Since $u(\boldsymbol{x})$ is obtained from an estimation $\boldsymbol{x}'$ of the state, it introduces also the estimation error $\hat{\boldsymbol{x}}$ in (3.36). Delays between the sampling of sensors and the control execution increases this estimation error:

Consider a known delay δ, and the state $\boldsymbol{x}^{-\delta}$ when sensors are sampled, the control action u is executed when the state is

$$\boldsymbol{x} = \boldsymbol{A}_\delta \boldsymbol{x}^{-\delta} + \boldsymbol{B}_\delta(u_{ref}^{-} + \boldsymbol{K}\tilde{\boldsymbol{x}}^{-} + \hat{u}^{-}), \tag{3.43}$$

where matrices $\boldsymbol{A}_\delta$, $\boldsymbol{B}_\delta$ are obtained from (3.25) using δ as sampling period. This state is normally estimated using a Smith predictor with available data as proposed in [Koenemann 2015]:

$$\boldsymbol{x}' = \boldsymbol{A}_\delta \boldsymbol{x}'^{-\delta} + \boldsymbol{B}_\delta(u^-_{ref} + \boldsymbol{K}(\tilde{\boldsymbol{x}}^- - \hat{\boldsymbol{x}}^-)), \tag{3.44}$$

where $\boldsymbol{x}'^{-\delta}$ is the estimation obtained from the robot sensors. The resulting estimation error is the difference:

$$\hat{\boldsymbol{x}} = \boldsymbol{x} - \boldsymbol{x}' = \boldsymbol{A}_\delta \hat{\boldsymbol{x}}^{-\delta} + \boldsymbol{B}_\delta(\hat{u}^- + \boldsymbol{K}\hat{\boldsymbol{x}}^-), \tag{3.45}$$

that is larger than the direct estimation error $\hat{\boldsymbol{x}}^{-\delta}$ due to the instability of $\boldsymbol{A}_\delta$. So, for each system the estimation error is:

P→CĊ

$$\hat{\boldsymbol{x}} = \boldsymbol{A}_\delta \hat{\boldsymbol{x}}^{-\delta} + \boldsymbol{B}_\delta(\hat{a}^- - \hat{n}^-)$$

P→X

$$\hat{\xi} = \boldsymbol{A}_\delta \hat{\xi}^{-\delta} + \boldsymbol{B}_\delta(\hat{a}^- - \hat{n}^-)$$

P_d→XP

$$\hat{\boldsymbol{x}} = \boldsymbol{A}_\delta \hat{\boldsymbol{x}}^{-\delta} + \boldsymbol{B}_\delta(\hat{a}^- - \hat{n}^- - \tfrac{\hat{\dot{n}}}{\gamma})$$

3.5.2 Stable Feedback Gains

The tracking error dynamics is stable if the norm of all eigenvalues (also called *poles*) of the closed-loop matrix are smaller than 1. Following Jury's stability criterion [Jury 1962] in the case of 2^{nd}-order systems, it is stable if and only if:

$$q_1 q_2 < 1, \tag{3.46}$$

$$(q_1 - 1)(q_2 - 1) = q_1 q_2 - (q_1 + q_2) + 1 > 0, \tag{3.47}$$

$$(q_1 + 1)(q_2 + 1) = q_1 q_2 + (q_1 + q_2) + 1 > 0, \tag{3.48}$$

where q_1 and q_2 are the system's poles. In particular for each system we have:

P→CĊ

Substituting the trace and determinant

$$q_1 q_2 = \det(\boldsymbol{A} + \boldsymbol{B}\boldsymbol{K}) = 1 - k + k\cosh(\omega\tau) - k\lambda\omega\sinh(\omega\tau), \tag{3.49}$$

$$q_1 + q_2 = \mathrm{tr}(\boldsymbol{A} + \boldsymbol{B}\boldsymbol{K}) = k + (2 - k)\cosh(\omega\tau) - k\lambda\omega\sinh(\omega\tau), \tag{3.50}$$

of the closed-loop matrix on Jury's conditions, the stability limits of $\boldsymbol{K}$ are:

$$\lambda > \frac{\cosh(\omega\tau) - 1}{\omega\sinh(\omega\tau)}, \tag{3.51}$$

$$k > 1, \tag{3.52}$$

$$k\lambda < \frac{\cosh(\omega\tau) + 1}{\omega\sinh(\omega\tau)}, \tag{3.53}$$

which are represented in Fig. 3.2.

P→X

The closed-loop pole is:

$$q = \boldsymbol{A} + \boldsymbol{B}k = \mathrm{e}^{\omega\tau} + k(1 - \mathrm{e}^{\omega\tau}), \tag{3.54}$$

its norm is smaller than 1 if k satisfies:

$$1 < k < \frac{\mathrm{e}^{\omega\tau} + 1}{\mathrm{e}^{\omega\tau} - 1}. \tag{3.55}$$

$\mathbf{P}_d \rightarrow \mathbf{XP}$

Substituting the trace and determinant

$$q_1 q_2 = \det(\boldsymbol{A} + \boldsymbol{B}\boldsymbol{K}) = \mathrm{e}^{(\omega-\gamma)\tau} + k\left(\frac{\gamma \mathrm{e}^{-\gamma\tau} + \omega \mathrm{e}^{\omega\tau}}{\gamma+\omega} + \lambda \mathrm{e}^{\omega\tau} - (\lambda+1)\mathrm{e}^{(\omega-\gamma)\tau}\right), \tag{3.56}$$

$$q_1 + q_2 = \mathrm{tr}(\boldsymbol{A} + \boldsymbol{B}\boldsymbol{K}) = \mathrm{e}^{-\gamma\tau} + \mathrm{e}^{\omega\tau} + k\left(\lambda - \frac{\gamma \mathrm{e}^{\omega\tau} + \omega \mathrm{e}^{-\gamma\tau}}{\gamma+\omega} - \lambda \mathrm{e}^{-\gamma\tau} + 1\right), \tag{3.57}$$

of the closed-loop matrix on Jury's conditions, the stability limits of $\boldsymbol{K}$ are:

$$\lambda < \frac{\mathrm{e}^{(\gamma-\omega)\tau} - 1}{\mathrm{e}^{\gamma\tau} - 1} k^{-1} + \frac{\gamma(\mathrm{e}^{\gamma\tau} - \mathrm{e}^{-\omega\tau})}{(\gamma+\omega)(\mathrm{e}^{\gamma\tau} - 1)} - 1, \tag{3.58}$$

$$\lambda > k^{-1} - 1, \tag{3.59}$$

$$\lambda > \frac{1+\mathrm{e}^{\gamma\tau}}{1-\mathrm{e}^{\gamma\tau}} k^{-1} + \frac{2\gamma(\mathrm{e}^{\gamma\tau} - \mathrm{e}^{-\omega\tau})}{(\gamma+\omega)(\mathrm{e}^{\gamma\tau} - 1)(1+\mathrm{e}^{-\omega\tau})} - 1. \tag{3.60}$$

which are represented in Fig. 3.3

3.6 Practical Summary and Conclusions

The external forces required for the robot locomotion are obtained from its interaction with the ground. In order to reduce the uncertainty, it is important to use an appropriate model for this interaction. We proposed the systems $\mathbf{P} \rightarrow \mathbf{C}\dot{\mathbf{C}}$ (3.2) and $\mathbf{P} \rightarrow \mathbf{X}$ (3.3) for rigid ground interactions, and $\mathbf{P}_d \rightarrow \mathbf{C}\dot{\mathbf{C}}\mathbf{P}$ (3.5) and $\mathbf{P}_d \rightarrow \mathbf{XP}$ (3.6) for compliant ground interactions.

Producing desired balance and locomotion of the robot while satisfying all its constraints requires planning the motion in advance, which is computationally demanding. In order to reduce the required CPU resources, we have arranged the control scheme (shown in Fig. 3.1) to plan the robot motion using a linear form of the complete CoM dynamics. Moreover, in order to reduce uncertainties, we use piece-wise constant control actions matching the typical choice of zero-order hold circuits for the control signal communication. As a result, we obtained linear time-invariant discrete-time control systems of the form:

$$\boldsymbol{x}^+ = \boldsymbol{A}\boldsymbol{x} + \boldsymbol{B}u, \tag{3.61}$$

with the matrices $\boldsymbol{A}$ and $\boldsymbol{B}$ reported in (3.27), (3.29) and (3.31).

In spite of the effort and resources spent trying to reduce uncertainties with fast and precise sensors, actuators and detailed models, we will always have some remaining uncertainty, which is dangerous considering the unstable dynamics and hard constraint of the robot. We compensate for the effects of these uncertainties introducing a feedback term in the control signal. As a result, we obtained the following control laws and uncertainties:

$\mathbf{P} \rightarrow \mathbf{C}\dot{\mathbf{C}}$

The proposed control law is:

$$u = p^c = p^c_{ref} + k(\tilde{c} + \lambda\tilde{\dot{c}}) + \hat{u}, \tag{3.62}$$

with uncertainties of the form:

$$\hat{u} = \hat{a} - \hat{n} - \boldsymbol{K}\big(\boldsymbol{A}_\delta \hat{\boldsymbol{x}}^{-\delta} + \boldsymbol{B}_\delta(\hat{a}^- - \hat{n}^-)\big), \tag{3.63}$$

coming from actuation, modelling and state estimation errors.

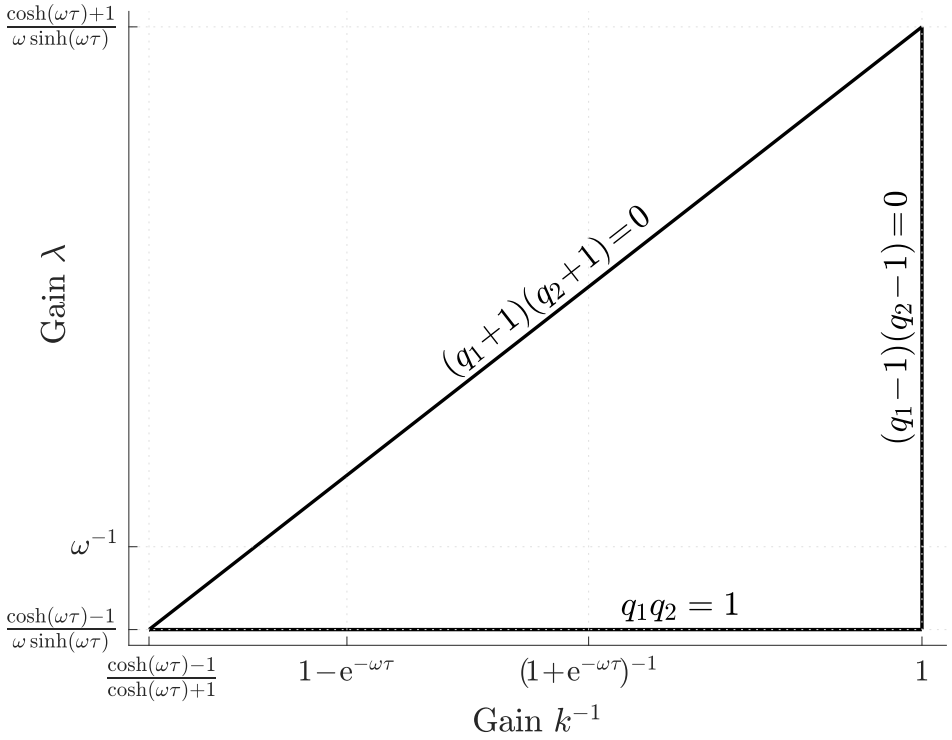

Figure 3.2: Set of stable gains for P→CĊ. The set of feedback gains k^{-1} and λ that lead to a stable closed-loop dynamics is a triangle, where λ varies between $\frac{\cosh(\omega\tau)-1}{\omega\sinh(\omega\tau)}$ and $\frac{\cosh(\omega\tau)+1}{\omega\sinh(\omega\tau)}$ while k^{-1} varies between $\frac{\cosh(\omega\tau)-1}{\cosh(\omega\tau)+1}$ and 1.

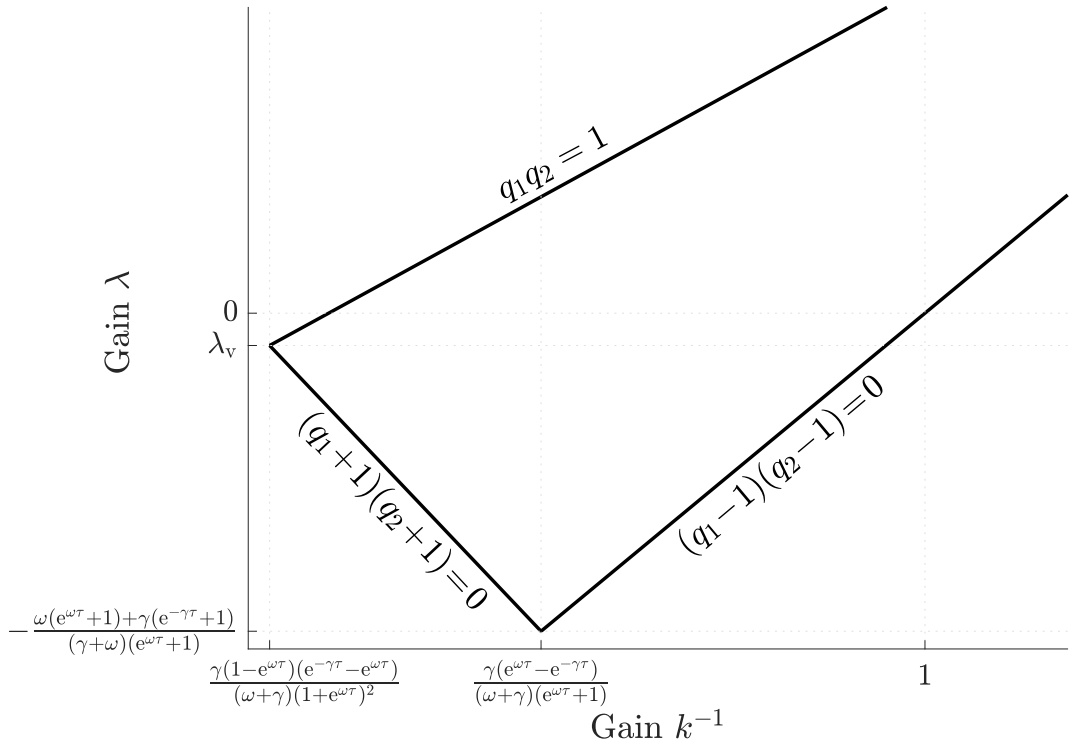

Figure 3.3: Set of stable gains for $\mathbf{P}_d$→XP. The set of feedback gains k^{-1} and λ that lead to a stable closed-loop dynamics is a triangle, where λ varies between $-\frac{\omega(\mathrm{e}^{\omega\tau}+1)+\gamma(\mathrm{e}^{-\gamma\tau}+1)}{(\gamma+\omega)(1+\mathrm{e}^{\omega\tau})}$ and $\frac{\omega(\mathrm{e}^{\omega\tau}-1)+\gamma(\mathrm{e}^{-\gamma\tau}-1)}{(\gamma+\omega)(1-\mathrm{e}^{\omega\tau})}$ while k^{-1} varies between $\frac{\gamma(1-\mathrm{e}^{\omega\tau})(\mathrm{e}^{-\gamma\tau}-\mathrm{e}^{\omega\tau})}{(\gamma+\omega)(1+\mathrm{e}^{\omega\tau})^2}$ and $\frac{\gamma(\mathrm{e}^{-\gamma\tau}-\mathrm{e}^{\omega\tau})}{(\gamma+\omega)(1-\mathrm{e}^{\omega\tau})}$. λ_v has a long expression, it can be positive or negative depending on the parameters γ, ω, τ.

P→X

The proposed control law is:

$$u = p^c = p^c_{ref} + k\tilde{\xi} + \hat{u}, \tag{3.64}$$

with uncertainties of the form:

$$\hat{u} = \hat{a} - \hat{n} - k\big(\mathrm{e}^{\omega\delta}\hat{\xi}^{-\delta} + (\mathrm{e}^{\omega\delta} - 1)(\hat{a}^- - \hat{n}^-)\big), \tag{3.65}$$

coming from actuation, modelling and state estimation errors.

$\mathbf{P}_d$→XP

The proposed control law is:

$$u = p^c_{des} = p^c_{des\cdot ref} + k(\tilde{\xi} + \lambda\tilde{p}^c) + \hat{u}, \tag{3.66}$$

with uncertainties of the form:

$$\hat{u} = \hat{a} - \hat{n} - \frac{\hat{\dot{n}}}{\gamma} - \boldsymbol{K}\left(\boldsymbol{A}_\delta\hat{\boldsymbol{x}}^{-\delta} + \boldsymbol{B}_\delta\left(\hat{a}^- - \hat{n}^- - \frac{\hat{\dot{n}}^-}{\gamma}\right)\right) + k\lambda\hat{n}, \tag{3.67}$$

coming from actuation, modelling and state estimation errors.

The set of feedback gains $\boldsymbol{K}$ that stabilize the closed-loop dynamics of each system is reported in eqs.(3.49)-(3.60).

Chapter 4

Bounded Deviations for Bounded Uncertainty

4.1 Introduction

This chapter exposes in a quantitative form the effect that uncertainty has on the tracking error and how to manage it for safety. We refer to uncertainty as the set of all possible control mistakes, described in the previous chapter; but, when one concrete mistake occurs during the robot operation, we call it a disturbance.

We show in Sec. 4.2 that using stable gains, a bounded uncertainty produces also bounded tracking errors contained in a Robust Positively Invariant (RPI) set. Based on this bound, we can obtain a relation between bound sizes of uncertainty and tracking error as shown in Sec. 4.3. Such relation depends on the eigenstructure of the closed-loop matrix, as we show in Sec. 4.4, where this relation is computed for real-valued and complex-conjugate poles. As a result, we obtain the Worst-Case Sequence (WCS) of disturbances and all vertices of the RPI set. In order to guarantee feasibility of the controller, and then, a safe robot operation, we must ensure the robot motion to satisfy the system constraints in spite of the tracking error as shown in Sec. 4.5.

4.2 Bounded Tracking Error

Considering some initial tracking error $\tilde{\boldsymbol{x}}$ and the entire set of uncertainties $\hat{u} \in \mathcal{V}$, the successor tracking error in (3.39) is bounded by the difference inclusion:

$$\tilde{\boldsymbol{x}}^{+} \in (\boldsymbol{A}+\boldsymbol{B}\boldsymbol{K})\tilde{\boldsymbol{x}} + \boldsymbol{B}\mathcal{V}. \tag{4.1}$$

By iteration, after N samples, the tracking error is

$$\tilde{\boldsymbol{x}}^{+N} \in (\boldsymbol{A}+\boldsymbol{B}\boldsymbol{K})^{N}\tilde{\boldsymbol{x}} + \bigoplus_{i=0}^{N-1}(\boldsymbol{A}+\boldsymbol{B}\boldsymbol{K})^{i}\boldsymbol{B}\mathcal{V}. \tag{4.2}$$

Since the feedback gain $\boldsymbol{K}$ is chosen to stabilize the closed-loop matrix $\boldsymbol{A}+\boldsymbol{B}\boldsymbol{K}$ (eigenvalues with norm smaller than 1), the first term vanishes when $N \to \infty$:

$$(\boldsymbol{A}+\boldsymbol{B}\boldsymbol{K})^{N}\tilde{\boldsymbol{x}} \to 0, \tag{4.3}$$

and the tracking error converges to a compact set [Kolmanovsky 1998, Theorem 4.1]:

$$\tilde{\boldsymbol{x}}^{+N} \to \mathcal{Z} \equiv \bigoplus_{i=0}^{\infty}(\boldsymbol{A}+\boldsymbol{B}\boldsymbol{K})^{i}\boldsymbol{B}\mathcal{V}. \tag{4.4}$$

Considering a convex set $\mathcal{V}$, this Minkowski sum is also convex [Schneider 1993, Sec. 1.1].

Based on its definition (4.4), the set $\mathcal{Z}$ satisfies

$$\mathcal{Z} = (\boldsymbol{A} + \boldsymbol{BK})\mathcal{Z} \oplus \boldsymbol{B}\mathcal{V}, \tag{4.5}$$

which implies from (4.1), that if the tracking error $\tilde{\boldsymbol{x}}$ belongs to the set $\mathcal{Z}$, then for any disturbance $\hat{u} \in \mathcal{V}$, the successor tracking error $\tilde{\boldsymbol{x}}^+$ will also belong to $\mathcal{Z}$:

$$\forall \hat{u} \in \mathcal{V}, \quad \tilde{\boldsymbol{x}} \in \mathcal{Z} \;\; \Rightarrow \;\; \tilde{\boldsymbol{x}}^+ \in \mathcal{Z}, \tag{4.6}$$

therefore, every future tracking error will belong to $\mathcal{Z}$ as long as $\hat{u} \in \mathcal{V}$. A set with this property is called Robust Positively Invariant (RPI), and in particular, $\mathcal{Z}$ is the minimum RPI set since it is contained in every closed RPI set of the closed-loop system (4.1) [Rakovic 2005].

We use this property to ensure a bounded tracking error

$$\tilde{\boldsymbol{x}} \in \mathcal{Z}, \tag{4.7}$$

with the input tracking error bounded accordingly

$$\tilde{u} \in \boldsymbol{K}\mathcal{Z} \oplus \mathcal{V}, \tag{4.8}$$

provided that the robot motion starts within these bounds. We can ensure the initial tracking error to lie in $\mathcal{Z}$ by starting the robot operation standing still, which reduces uncertainty (minimum actuation and $\boldsymbol{n}$, $\hat{\boldsymbol{n}}$ vanish) letting the stable matrix $\boldsymbol{A}+\boldsymbol{BK}$ to bring the tracking error closer to zero, within $\mathcal{Z}$. A safer form to ensure it, proposed in Ch. 6, is to generate the reference trajectory $\boldsymbol{x}_{ref}$ satisfying (4.7) as an initial condition based on the current state $\boldsymbol{x}$.

4.3 Quantitative Effect of Uncertainties

We can obtain a bound for the tracking error of every variable in the CoM dynamics using the set $\mathcal{Z}$ and operations of sets described in Appx. A:

P→CĊ

CoM position and velocity tracking errors are bounded as:

$$\begin{aligned} \tilde{c} &= \begin{bmatrix} 1 & 0 \end{bmatrix} \tilde{\boldsymbol{x}} \in \begin{bmatrix} 1 & 0 \end{bmatrix} \mathcal{Z}, \\ \dot{\tilde{c}} &= \begin{bmatrix} 0 & 1 \end{bmatrix} \tilde{\boldsymbol{x}} \in \begin{bmatrix} 0 & 1 \end{bmatrix} \mathcal{Z}, \end{aligned} \tag{4.9}$$

and the cCoP tracking error is bounded as (3.37):

$$\tilde{p}^c = \tilde{u} = \boldsymbol{K}\tilde{\boldsymbol{x}} + \hat{u} \in \boldsymbol{K}\mathcal{Z} \oplus \mathcal{V}. \tag{4.10}$$

P→X

The DCM tracking error is bounded as:

$$\tilde{\xi} = \tilde{x} \in \mathcal{Z}, \tag{4.11}$$

and the cCoP tracking error is bounded as (3.37):

$$\tilde{p}^c = \tilde{u} = k\tilde{\xi} + \hat{u} \in k\mathcal{Z} \oplus \mathcal{V}. \tag{4.12}$$

$\mathbf{P}_d \rightarrow \mathbf{XP}$

DCM and cCoP tracking errors are bounded as:

$$\begin{aligned} \tilde{\xi} &= \begin{bmatrix} 1 & 0 \end{bmatrix} \tilde{\boldsymbol{x}} \in \begin{bmatrix} 1 & 0 \end{bmatrix} \mathcal{Z}, \\ \tilde{p}^c &= \begin{bmatrix} 0 & 1 \end{bmatrix} \tilde{\boldsymbol{x}} \in \begin{bmatrix} 0 & 1 \end{bmatrix} \mathcal{Z}, \end{aligned} \tag{4.13}$$

and the tracking error bound of the desired cCoP is (3.37):

$$\tilde{p}^c_{des} = \tilde{u} = \boldsymbol{K}\tilde{\boldsymbol{x}} + \hat{u} \in \boldsymbol{K}\mathcal{Z} \oplus \mathcal{V}. \tag{4.14}$$

In general terms, the tracking error $\boldsymbol{L}\tilde{\boldsymbol{x}}$ of any linear combination of state variables, with coefficients in some vector $\boldsymbol{L}$, is bounded according to (4.7)

$$\boldsymbol{L}\tilde{\boldsymbol{x}} \in \boldsymbol{L}\mathcal{Z}. \tag{4.15}$$

From linear programming, the maximum value $\boldsymbol{L}\boldsymbol{z}$ is reached at some vertex $\boldsymbol{z} \in \mathcal{Z}$. Iterating in (3.39) with disturbances $\hat{u}_i \in \mathcal{V}$ contained in the real interval

$$\mathcal{V} \equiv [-\hat{u}_{\text{peak}},\ \hat{u}_{\text{peak}}], \tag{4.16}$$

this maximum tracking error

$$\boldsymbol{L}\boldsymbol{z} = \max_{\hat{\boldsymbol{U}}} \sum_{i=0}^{\infty} \boldsymbol{L}(\boldsymbol{A}+\boldsymbol{B}\boldsymbol{K})^i \boldsymbol{B}\hat{u}_{-i} \tag{4.17}$$

is obtained using a Worst-Case Sequence (WCS) of disturbances

$$\hat{\boldsymbol{U}}_{\text{L}} \equiv \langle \ldots,\ \hat{u}_{-2},\ \hat{u}_{-1},\ \hat{u}_0 \rangle, \tag{4.18}$$

with

$$\hat{u}_{-i} = \text{sign}\big(\boldsymbol{L}(\boldsymbol{A}+\boldsymbol{B}\boldsymbol{K})^i \boldsymbol{B}\big)\hat{u}_{\text{peak}} \tag{4.19}$$

maximizing each addend of the sum in (4.17). So, we have

$$\boldsymbol{L}\boldsymbol{z} = \sum_{i=0}^{\infty} \big|\boldsymbol{L}(\boldsymbol{A}+\boldsymbol{B}\boldsymbol{K})^i \boldsymbol{B}\big| \hat{u}_{\text{peak}}. \tag{4.20}$$

Let's also define the ratio

$$r_{\text{L}} \equiv \frac{\boldsymbol{L}\boldsymbol{z}}{\hat{u}_{\text{peak}}} = \sum_{i=0}^{\infty} \big|\boldsymbol{L}(\boldsymbol{A}+\boldsymbol{B}\boldsymbol{K})^i \boldsymbol{B}\big|, \tag{4.21}$$

that translates the bound $\hat{u}_{\text{peak}}$ of the uncertainty $\hat{u}$ into the bound $\boldsymbol{L}\boldsymbol{z}$ of the tracking error $\boldsymbol{L}\tilde{\boldsymbol{x}}$. Since the closed-loop matrix $\boldsymbol{A}+\boldsymbol{B}\boldsymbol{K}$ is designed to be stable, this series converges to some value depending on our choice of feedback gain $\boldsymbol{K}$.

4.4 Series Convergence

Assuming that the closed-loop matrix is diagonalizable, we factorize it as follows:

$$\boldsymbol{A}+\boldsymbol{B}\boldsymbol{K} = \boldsymbol{M} \begin{bmatrix} q_1 & 0 \\ 0 & q_2 \end{bmatrix} \boldsymbol{M}^{-1}, \tag{4.22}$$

with an invertible matrix $\boldsymbol{M}$, so that the sum (4.21) is equivalent to:

$$\begin{aligned} r_{\text{L}} &= \sum_{i=0}^{\infty} \left| \boldsymbol{L}\boldsymbol{M} \begin{bmatrix} q_1^i & 0 \\ 0 & q_2^i \end{bmatrix} \boldsymbol{M}^{-1}\boldsymbol{B} \right| \\ &= \sum_{i=0}^{\infty} \left| \alpha_1 q_1^i + \alpha_2 q_2^i \right|, \end{aligned} \tag{4.23}$$

with coefficients α_1 and α_2 obtained directly from the matrices $\boldsymbol{L}\boldsymbol{M}$ and $\boldsymbol{M}^{-1}\boldsymbol{B}$:

$$\begin{aligned} \alpha_1 &\equiv \boldsymbol{L}\boldsymbol{M}_{\mathtt{c},1}\boldsymbol{M}_{\mathtt{r},1}^{-1}\boldsymbol{B} \\ \alpha_2 &\equiv \boldsymbol{L}\boldsymbol{M}_{\mathtt{c},2}\boldsymbol{M}_{\mathtt{r},2}^{-1}\boldsymbol{B}, \end{aligned} \tag{4.24}$$

where the matrix subindexes identify one single column or one single row:

$$\boldsymbol{M} = \begin{bmatrix} \boldsymbol{M}_{\mathtt{c},1} & \boldsymbol{M}_{\mathtt{c},2} \end{bmatrix}, \qquad \boldsymbol{M}^{-1} = \begin{bmatrix} \boldsymbol{M}_{\mathtt{r},1}^{-1} \\ \boldsymbol{M}_{\mathtt{r},2}^{-1} \end{bmatrix}. \tag{4.25}$$

4.4.1 Real-Valued Poles

When the closed-loop matrix $\boldsymbol{A} + \boldsymbol{B}\boldsymbol{K}$ has real-valued poles q_1, q_2, we rename poles and coefficients such that $|q_m| < |q_{\text{M}}|$. If $|q_1| = |q_2|$, we rename them such that $|\alpha_m| \leq |\alpha_{\text{M}}|$.

4.4.1.1 Ratio Between Bounds

Let's rewrite the series (4.23) making explicit the sign inside the absolute value of the i-th addend $\alpha_m q_m^i + \alpha_{\text{M}} q_{\text{M}}^i$ which is determined by the term with bigger absolute value.

Case 1: When $\alpha_{\text{M}} = 0$, the sum (4.23) is actually a geometric series

$$r_{\text{L}} = \sum_{i=0}^{\infty} \left| \alpha_m q_m^i \right|, \tag{4.26}$$

and converges to

$$r_{\text{L}} = \frac{|\alpha_m|}{1 - |q_m|}. \tag{4.27}$$

Case 2: When $|\alpha_m| \leq |\alpha_{\text{M}}|$, since $|q_m| \leq |q_{\text{M}}|$, we have that $\forall i$, $|\alpha_m q_m^i| \leq |\alpha_{\text{M}} q_{\text{M}}^i|$, which means:

$$\forall i \geq 0, \qquad \operatorname{sign}(\alpha_m q_m^i + \alpha_{\text{M}} q_{\text{M}}^i) = \operatorname{sign}(\alpha_{\text{M}} q_{\text{M}}^i), \tag{4.28}$$

so, the sum (4.23) is actually the sum of two geometric series

$$r_{\text{L}} = \sum_{i=0}^{\infty} \left| \alpha_m q_m^i + \alpha_{\text{M}} q_{\text{M}}^i \right| = \left(\alpha_m \sum_{i=0}^{\infty} (s_{\text{M}} q_m)^i + \alpha_{\text{M}} \sum_{i=0}^{\infty} (s_{\text{M}} q_{\text{M}})^i \right) \operatorname{sign}(\alpha_{\text{M}}), \tag{4.29}$$

where s_{M} is the sign of q_{M}, and the sum converges to

$$r_{\text{L}} = \left(\frac{\alpha_m}{1 - s_{\text{M}} q_m} + \frac{\alpha_{\text{M}}}{1 - s_{\text{M}} q_{\text{M}}} \right) \operatorname{sign}(\alpha_{\text{M}}). \tag{4.30}$$

Case 3: When $|\alpha_m| > |\alpha_{\mathrm{M}}|$, with $\alpha_{\mathrm{M}} \neq 0$ and $|q_m| < |q_{\mathrm{M}}|$, we have

$$\begin{aligned} |\alpha_m q_m^i| \leq |\alpha_{\mathrm{M}} q_{\mathrm{M}}^i| &\iff \left|\frac{q_m}{q_{\mathrm{M}}}\right|^i \leq \left|\frac{\alpha_{\mathrm{M}}}{\alpha_m}\right| \\ &\iff i \geq \frac{\ln|\alpha_{\mathrm{M}}/\alpha_m|}{\ln|q_m/q_{\mathrm{M}}|} \equiv \nu, \end{aligned} \tag{4.31}$$

where we call the fraction obtained ν. Note that both $\ln(|\alpha_{\mathrm{M}}/\alpha_m|)$ and $\ln(|q_m/q_{\mathrm{M}}|)$ are negative. Similarly, we can obtain that $|\alpha_m q_m^i| > |\alpha_{\mathrm{M}} q_{\mathrm{M}}^i|$ when $i < \nu$.

It means that

$$\begin{aligned} &\text{when } i < n && \operatorname{sign}(\alpha_m q_m^i + \alpha_{\mathrm{M}} q_{\mathrm{M}}^i) = \operatorname{sign}(\alpha_m q_m^i) \\ &\text{when } i \geq n && \operatorname{sign}(\alpha_m q_m^i + \alpha_{\mathrm{M}} q_{\mathrm{M}}^i) = \operatorname{sign}(\alpha_{\mathrm{M}} q_{\mathrm{M}}^i), \end{aligned} \tag{4.32}$$

where $n \in \mathbb{N}$ is the smallest integer bigger than ν ($n = \lceil \nu \rceil$, rounded up). So, we can separate the sum (4.23) in four geometric series

$$\begin{aligned} r_{\mathrm{L}} = &\left(\alpha_m \sum_{i=0}^{n-1} (s_m q_m)^i + \alpha_{\mathrm{M}} \sum_{i=0}^{n-1} (s_m q_{\mathrm{M}})^i\right) \operatorname{sign}(\alpha_m) \\ &+ \left(\alpha_m \sum_{i=n}^{\infty} (s_{\mathrm{M}} q_m)^i + \alpha_{\mathrm{M}} \sum_{i=n}^{\infty} (s_{\mathrm{M}} q_{\mathrm{M}})^i\right) \operatorname{sign}(\alpha_{\mathrm{M}}), \end{aligned} \tag{4.33}$$

where s_m is the sign of q_m, and the sum converges to

$$\begin{aligned} r_{\mathrm{L}} = &\left(\alpha_m \frac{1-(s_m q_m)^n}{1-s_m q_m} + \alpha_{\mathrm{M}} \frac{1-(s_m q_{\mathrm{M}})^n}{1-s_m q_{\mathrm{M}}}\right) \operatorname{sign}(\alpha_m) \\ &+ \left(\alpha_m \frac{(s_{\mathrm{M}} q_m)^n}{1-s_{\mathrm{M}} q_m} + \alpha_{\mathrm{M}} \frac{(s_{\mathrm{M}} q_{\mathrm{M}})^n}{1-s_{\mathrm{M}} q_{\mathrm{M}}}\right) \operatorname{sign}(\alpha_{\mathrm{M}}). \end{aligned} \tag{4.34}$$

Notice that this latter expression reduces to the **case 1** when $n \to \infty$ (with $\alpha_{\mathrm{M}} = 0$) and to the **case 2** when $n = 0$. So, we can unify all cases with this latter formulation using different values of n.

All possibilities are contained in cases **1**, **2** and **3**, but we consider an additional case which overlaps with cases **2** and **3** since it corresponds to an important property that we will discuss in the next chapter:

Case 4: When poles q_m, q_{M} and coefficients α_m, α_{M} have equal signs

$$\operatorname{sign}(\alpha_{\mathrm{M}}) = \operatorname{sign}(\alpha_m), \qquad \operatorname{sign}(q_{\mathrm{M}}) = \operatorname{sign}(q_m), \tag{4.35}$$

we have

$$\operatorname{sign}(\alpha_m q_m^i + \alpha_{\mathrm{M}} q_{\mathrm{M}}^i) = \operatorname{sign}(\alpha_m q_m^i) = \operatorname{sign}(\alpha_{\mathrm{M}} q_{\mathrm{M}}^i) \qquad \forall i \geq 0, \tag{4.36}$$

so, regardless of the relation between coefficients α_m, α_{M}, we can use (4.30) or equivalently $n = 0$ in (4.34).

4.4.1.2 Worst-Case Disturbances

The WCS of disturbances (4.18) follows the same separation in four cases since it depends on the same sign structure (4.19). We name these sequences depending on the parameter n since it will be helpful in the following sections.

In cases **2** (4.28) and **4** (4.36) (corresponding to $n = 0$), the WCS is

$$\hat{\boldsymbol{U}}_{\mathrm{L}} = \hat{\boldsymbol{U}}_0 = \langle \ldots, \hat{u}_{(2|0)}, \hat{u}_{(1|0)}, \hat{u}_{(0|0)} \rangle, \tag{4.37}$$

with elements of the form (4.19):

$$\hat{u}_{(i|0)} = s_{\mathrm{M}}^i \mathrm{sign}(\alpha_{\mathrm{M}}) \hat{u}_{\mathrm{peak}}. \tag{4.38}$$

In the case **3** (4.32), we can write the WCS as

$$\hat{\boldsymbol{U}}_{\mathrm{L}} = \langle \hat{\boldsymbol{U}}_0 s_{\mathrm{M}}^n, \hat{\boldsymbol{U}}_n \rangle \tag{4.39}$$

where the final sequence of n iterations is:

$$\hat{\boldsymbol{U}}_n = \langle \hat{u}_{(n-1|n)}, \hat{u}_{(n-2|n)}, \ldots, \hat{u}_{(0|n)} \rangle, \tag{4.40}$$

with elements of the form (4.19):

$$\hat{u}_{(i|n)} = s_m^i \mathrm{sign}(\alpha_m) \hat{u}_{\mathrm{peak}}. \tag{4.41}$$

In the case **1** (corresponding to $n \to \infty$) the WCS is

$$\hat{\boldsymbol{U}}_{\mathrm{L}} = \hat{\boldsymbol{U}}_\infty = \langle \ldots, \hat{u}_{(2|\infty)}, \hat{u}_{(1|\infty)}, \hat{u}_{(0|\infty)} \rangle, \tag{4.42}$$

also satisfying (4.19) with elements of the form (4.41).

Notice that each sequence $\hat{\boldsymbol{U}}_0$, $\hat{\boldsymbol{U}}_n$, $\hat{\boldsymbol{U}}_\infty$ depends on the sign of only one pole s_{M} or s_m and is either constant when it is positive, or alternate when it is negative.

4.4.1.3 Reaching Vertices of the Minimum RPI Set

The coefficients α_1, α_2 (4.24) satisfy the bijective relation with $\boldsymbol{L}$:

$$\begin{bmatrix} \alpha_1 & \alpha_2 \end{bmatrix} = \boldsymbol{L}\boldsymbol{M} \begin{bmatrix} \boldsymbol{M}_{\mathbf{r},1}^{-1}\boldsymbol{B}_1 & 0 \\ 0 & \boldsymbol{M}_{\mathbf{r},2}^{-1}\boldsymbol{B}_2 \end{bmatrix}, \tag{4.43}$$

where, since $\boldsymbol{M}$ is invertible by hypothesis (4.22) and assuming that $\boldsymbol{M}_{\mathbf{r},1}^{-1}\boldsymbol{B}$, $\boldsymbol{M}_{\mathbf{r},2}^{-1}\boldsymbol{B}$ are different to 0, the matrix on the right is invertible. So, by choosing the vector $\boldsymbol{L}$, we can get any pair of coefficients α_1, α_2, corresponding to any of the four cases proposed before and to any value of $n \in \mathbb{N}$ in the case **3** for given poles q_1, q_2. For each case, and each value of n, we have a corresponding WCS of disturbances

$$\hat{\boldsymbol{U}}_{\mathrm{L}} = \langle \hat{\boldsymbol{U}}_0 s_{\mathrm{M}}^n, \hat{\boldsymbol{U}}_n \rangle, \tag{4.44}$$

that reaches accordingly some vertex $\boldsymbol{z} \in \mathcal{Z}$ maximizing the product $\boldsymbol{L}\tilde{\boldsymbol{x}}$ subject to $\tilde{\boldsymbol{x}} \in \mathcal{Z}$. Therefore, by varing the vector $\boldsymbol{L}$, we can reach all vertices of the minimum RPI set $\mathcal{Z}$.

In the following sections we will choose the vector $\boldsymbol{L}$ to decide arbitrarily the value of $n \in \mathbb{N}$ and the sign of α_m.

4.4.1.4 Stationary Tracking Error

Iterating in (3.39) with the sequence $\hat{\boldsymbol{U}}_0$, the tracking error reaches some vertex $\boldsymbol{z}_0$

$$\tilde{\boldsymbol{x}} \to \boldsymbol{z}_0 = \sum_{i=0}^{\infty} (\boldsymbol{A} + \boldsymbol{B}\boldsymbol{K})^i \boldsymbol{B} \hat{u}_{(i|0)} \in \mathcal{Z}, \tag{4.45}$$

and maintains the stationary condition

$$s_{\mathrm{M}}\boldsymbol{z}_0 = (\boldsymbol{A} + \boldsymbol{B}\boldsymbol{K})\boldsymbol{z}_0 + \boldsymbol{B}\hat{u}_{(i|0)}, \tag{4.46}$$

$$\boldsymbol{z}_0 = (\boldsymbol{A} + \boldsymbol{B}\boldsymbol{K}) s_{\mathrm{M}} \boldsymbol{z}_0 + \boldsymbol{B}\hat{u}_{(i+1|0)}, \tag{4.47}$$

while disturbances $\hat{u}_{(i|0)}$ have the form (4.38) of the sequence $\hat{\boldsymbol{U}}_0$ as we show in the Appx. B.

4.4.1.5 Numbered Vertices

Consider the worst-case subsequences (4.39) of case **3**

$$\begin{aligned}
\hat{\boldsymbol{U}}_1 &= \langle \hat{u}_{(0|1)} \rangle && \text{with} && n = 1 \\
\hat{\boldsymbol{U}}_2 &= \langle \hat{u}_{(1|2)},\ \hat{u}_{(0|2)} \rangle && \text{with} && n = 2 \\
&\vdots \\
\hat{\boldsymbol{U}}_n &= \langle \hat{u}_{(n\text{-}1|n)},\ \ldots,\ \hat{u}_{(1|n)},\ \hat{u}_{(0|n)} \rangle && \text{with} && n \in \mathbb{N}.
\end{aligned} \tag{4.48}$$

For each subsequence $\hat{\boldsymbol{U}}_n$, we choose a vector $\boldsymbol{L}$ producing $\operatorname{sign}(\alpha_m) = s_m^{n\text{-}1}$ to obtain them all starting in the same form (4.41):

$$\begin{aligned}
\hat{u}_{(n\text{-}1|n)} &= s_m^{n\text{-}1} \operatorname{sign}(\alpha_m) \hat{u}_{\text{peak}} \\
&= s_m^{n\text{-}1} s_m^{n\text{-}1} \hat{u}_{\text{peak}} \\
&= \hat{u}_{\text{peak}},
\end{aligned} \tag{4.49}$$

so that, we can nest them:

$$\begin{aligned}
\hat{\boldsymbol{U}}_1 &= \langle \hat{u}_{(0|1)} \rangle = \hat{u}_{\text{peak}} && \text{with} && n = 1 \\
\hat{\boldsymbol{U}}_2 &= \langle \hat{\boldsymbol{U}}_1,\ \hat{u}_{(0|2)} \rangle = \langle s_m^0,\ s_m^1 \rangle \hat{u}_{\text{peak}} && \text{with} && n = 2 \\
&\vdots \\
\hat{\boldsymbol{U}}_n &= \langle \hat{\boldsymbol{U}}_{n\text{-}1},\ \hat{u}_{(0|n)} \rangle = \langle s_m^0,\ s_m^1,\ \ldots,\ s_m^{n\text{-}1} \rangle \hat{u}_{\text{peak}} && \text{with} && n \in \mathbb{N}.
\end{aligned} \tag{4.50}$$

Therefore, after reaching the vertex $\tilde{\boldsymbol{x}} \to \boldsymbol{z}_0$ (4.46), (4.47) produced by $\hat{\boldsymbol{U}}_0$, the WCS

$$\hat{\boldsymbol{U}}_{\text{L}} = \langle \hat{\boldsymbol{U}}_0 s_{\text{M}}^n,\ \hat{\boldsymbol{U}}_n \rangle, \tag{4.51}$$

actually finishes iteratively n worst-case sequences, reaching accordingly a new vertex at each iteration:

$$\begin{aligned}
\boldsymbol{z}_1 &= (\boldsymbol{A} + \boldsymbol{B}\boldsymbol{K}) \boldsymbol{z}_0 + \boldsymbol{B} \hat{u}_{(0|1)} s_m \\
\boldsymbol{z}_2 &= (\boldsymbol{A} + \boldsymbol{B}\boldsymbol{K}) \boldsymbol{z}_1 + \boldsymbol{B} \hat{u}_{(0|2)} s_m \\
&\vdots \\
\boldsymbol{z}_n &= (\boldsymbol{A} + \boldsymbol{B}\boldsymbol{K}) \boldsymbol{z}_{n\text{-}1} + \boldsymbol{B} \hat{u}_{(0|n)} s_m.
\end{aligned} \tag{4.52}$$

As a result, vertices of the minimum RPI set $\mathcal{Z}$ are reached in order by the WCS $\hat{\boldsymbol{U}}_{\text{L}}$, and the number n (together with $\operatorname{sign}(\alpha_m)$) identifies one particular vertex $\boldsymbol{z}_n$ in $\mathcal{Z}$. This analytic computation of vertices is shown in Fig. 4.1, where we compare them with the outer approximation proposed by [Rakovic 2005].

4.4.2 Complex-Valued Poles

When the poles are complex-conjugate $q_{1,2} = q\,\mathrm{e}^{\pm j\theta}$, also the coefficients $\alpha_{1,2} = \alpha\,\mathrm{e}^{\pm j\varphi}$ are complex conjugate, as we show in the Appx. C.

4.4.2.1 Ratio Between Bounds

In this case the infinite sum (4.23) becomes

$$\begin{aligned}
r_{\text{L}} = \sum_{i=0}^{\infty} \left| \alpha_1 q_1^i + \alpha_2 q_2^i \right| &= \alpha \sum_{i=0}^{\infty} \left| \mathrm{e}^{(i\theta+\varphi)j} + \mathrm{e}^{-(i\theta+\varphi)j} \right| q^i \\
&= 2\alpha \sum_{i=0}^{\infty} \left| \cos(i\theta + \varphi) \right| q^i.
\end{aligned} \tag{4.53}$$

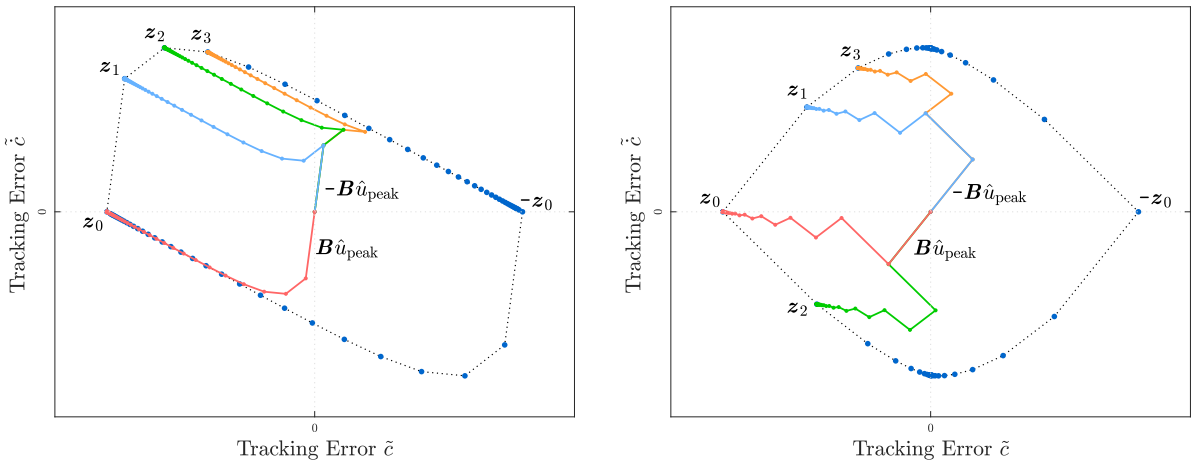

Figure 4.1: minimum RPI sets. Both poles are positive on the left, and they have opposite signs on the right. We show all terms of the summation (4.45) using the WCS $\hat{\boldsymbol{U}}_0$ (in red) that reaches the vertex $\boldsymbol{z}_0$ and the three first iterations of the subsequence $\hat{\boldsymbol{U}}_n$ (4.52) reaching the vertices $\boldsymbol{z}_1$ (in blue), $\boldsymbol{z}_2$ (in green) and $\boldsymbol{z}_3$ (in orange). We also show the outer approximation of the minimum RPI set proposed in [Rakovic 2005] with dotted black lines.

Considering poles with any angle θ, the factor $|\cos(i\theta+\phi)|$ is normally aperiodic making hard the computation of r_{L}. So, we propose the upper bound approximation

$$\begin{aligned} r_{\text{L}} \leq r'_{\text{L}} &= 2\alpha \sum_{i=0}^{n-1} |\cos(i\theta+\varphi)|\, q^i + 2\alpha \sum_{h=n}^{\infty} q^h \\ &= 2\alpha \sum_{i=0}^{n-1} |\cos(i\theta+\varphi)|\, q^i + 2\alpha \frac{q^n}{1-q}, \end{aligned} \tag{4.54}$$

where since $|\cos(i\theta+\varphi)| \leq 1 \quad \forall i$, we replace the cosine by 1 for all addend with $i \geq n$, choosing some number $n \in \mathbb{N}$ to ensure a small enough approximation error $\hat{r}_{\text{L}}$:

$$\hat{r}_{\text{L}} = r_{\text{L}} - r'_{\text{L}}, \qquad -\frac{2\alpha q^n}{1-q} < \hat{r}_{\text{L}} < 0. \tag{4.55}$$

When the ratio between the angle θ and 2π is a rational number, $|\cos(i\theta+\varphi)|$ varies with the period

$$T = \frac{\text{LCM}(\theta,\ 2\pi)}{\theta}, \tag{4.56}$$

given by the Least Common Multiple (LCM) of θ and 2π. So, we can rewrite r_{L} as

$$r_{\text{L}} = 2\alpha \sum_{h=0}^{\infty} \left(\sum_{i=0}^{T-1} |\cos(i\theta+\varphi)| q^i \right) q^{hT}, \tag{4.57}$$

to obtain the exact convergence

$$r_{\text{L}} = 2\alpha \frac{\sum_{i=0}^{T-1} |\cos(i\theta+\varphi)| q^i}{1-q^T}. \tag{4.58}$$

4.4.2.2 Worst-Case Disturbances

Based on the ratio r_{L} (4.53), the WCS of disturbances

$$\hat{\boldsymbol{U}}_{\text{L}} = \langle \dots, \hat{u}_{(2|\text{L})}, \hat{u}_{(1|\text{L})}, \hat{u}_{(0|\text{L})} \rangle, \tag{4.59}$$

has elements of the form (4.19):

$$\hat{u}_{(i|\text{L})} = \frac{\cos(i\theta + \varphi)}{|\cos(i\theta + \varphi)|} \hat{u}_{\text{peak}}. \tag{4.60}$$

4.4.2.3 Reaching Vertices of the Minimum RPI Set

The WCS of disturbances $\hat{\boldsymbol{U}}_{\text{L}}$ is designed to maximize the tracking error $\boldsymbol{L}\tilde{\boldsymbol{x}}$ for some vector of coefficients $\boldsymbol{L}$. Since $\tilde{\boldsymbol{x}}$ is bound to the minimum RPI set $\mathcal{Z}$, this maximum value $\boldsymbol{L}\boldsymbol{z}$ is reached at some vertex $\boldsymbol{z} \in \mathcal{Z}$. The sequence $\hat{\boldsymbol{U}}_{\text{L}}$ is determined by the angles θ and φ from poles $q_{1,2} = q\text{e}^{\pm j\theta}$ and coefficients $\alpha_{1,2} = \alpha\text{e}^{\pm j\varphi}$. From the definition of coefficients α_1, α_2 (4.24), we can see that φ is actually the angle between $\boldsymbol{L}$ and $\boldsymbol{B}$:

$$\begin{aligned} \boldsymbol{L}\boldsymbol{B} =& \boldsymbol{L}\boldsymbol{M}\boldsymbol{M}^{-1}\boldsymbol{B} \\ =& \boldsymbol{L}\boldsymbol{M}_{\text{c},1}\boldsymbol{M}_{\text{r},1}^{-1}\boldsymbol{B} + \boldsymbol{L}\boldsymbol{M}_{\text{c},2}\boldsymbol{M}_{\text{r},2}^{-1}\boldsymbol{B} \\ =& \alpha_1 + \alpha_2 \\ =& 2\alpha\cos(\varphi) \qquad \Longrightarrow \quad |\boldsymbol{L}||\boldsymbol{B}| = 2\alpha, \quad \angle(\boldsymbol{L},\ \boldsymbol{B}) = \varphi. \end{aligned} \tag{4.61}$$

So, considering vectors $\boldsymbol{L}_i$ such that $\angle(\boldsymbol{L}_i,\ \boldsymbol{B}) = \varphi + i\theta$, each iteration of the sequence (4.59) reaches a corresponding vertex $\boldsymbol{z}_i \in \mathcal{Z}$.

4.4.2.4 Vertices of the Minimum RPI Set

We consider the tracking error $\boldsymbol{L}\tilde{\boldsymbol{x}}$ that reaches its maximum value at some vertex $\boldsymbol{z}_0 \in \mathcal{Z}$ and we propose an outer approximation to such vertex:

$$\boldsymbol{z}_0' = \sum_{i=0}^{n-1} (\boldsymbol{A} + \boldsymbol{B}\boldsymbol{K})^i \boldsymbol{B}\hat{u}_{(i|\text{L})} + \frac{q^n}{1-q}\boldsymbol{B}\frac{\hat{u}_{\text{peak}}}{\cos(\varphi)}, \tag{4.62}$$

where the first term is obtained iterating n times in (3.39) with the WCS (4.59) $\hat{\boldsymbol{U}}_{\text{L}}$ and φ is the angle between $\boldsymbol{L}$ and $\boldsymbol{B}$. Let's show that $\boldsymbol{z}_0'$ is an outer approximation of $\boldsymbol{z}_0$: Multiplying by $\boldsymbol{L}$ on the left we obtain

$$\boldsymbol{L}\boldsymbol{z}_0' = \sum_{i=0}^{n-1} \boldsymbol{L}(\boldsymbol{A} + \boldsymbol{B}\boldsymbol{K})^i \boldsymbol{B}\hat{u}_{(i|\text{L})} + \frac{q^n}{1-q}\boldsymbol{L}\boldsymbol{B}\frac{\hat{u}_{\text{peak}}}{\cos(\varphi)}, \tag{4.63}$$

using the factorization (4.22), the coefficients α_1, α_2 from (4.24) and the product $\boldsymbol{L}\boldsymbol{B}$ from (4.61), it is

$$\begin{aligned} \boldsymbol{L}\boldsymbol{z}_0' &= \sum_{i=0}^{n-1} |\alpha_1 q_1^i + \alpha_2 q_2^i| \hat{u}_{\text{peak}} + 2\alpha\frac{q^n}{1-q}\hat{u}_{\text{peak}} \\ &= \left(2\alpha \sum_{i=0}^{n-1} |\cos(i\theta + \varphi)| q^i + 2\alpha\frac{q^n}{1-q} \right) \hat{u}_{\text{peak}}, \end{aligned} \tag{4.64}$$

that is an upper bound approximation of the tracking error bound $\boldsymbol{L}\boldsymbol{z}_0$, from (4.54):

$$\boldsymbol{L}\boldsymbol{z}_0' = r_{\text{L}}'\hat{u}_{\text{peak}}. \tag{4.65}$$

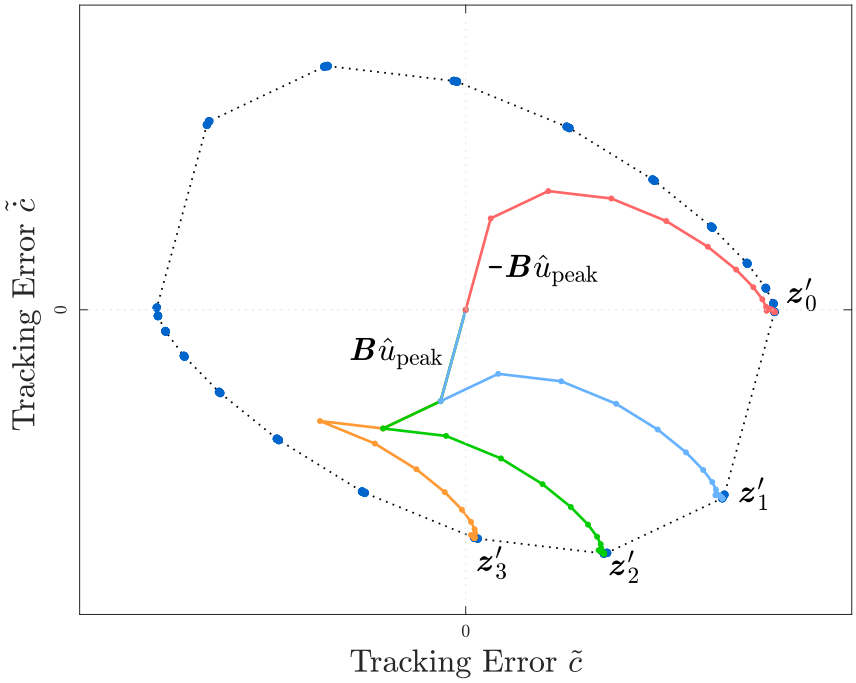

Figure 4.2: minimum RPI set. We show in red the summation (4.17) that reaches some vertex $\boldsymbol{z}_0$, approximated here by $\boldsymbol{z}'_0$. Then, vertices $\boldsymbol{z}_1$, $\boldsymbol{z}_2$, $\boldsymbol{z}_3$, $\cdots$ (or their outer approximations) are obtained by one iteration each. We also show the outer approximation of the minimum RPI set proposed in [Rakovic 2005] with dotted black lines.

The estimation error on $\boldsymbol{z}'_0$ is

$$\hat{\boldsymbol{z}}_0 = \boldsymbol{z}_0 - \boldsymbol{z}'_0 = \mu \frac{q^n}{1-q} \boldsymbol{B} \frac{\hat{u}_{\text{peak}}}{\cos(\varphi)}, \qquad \text{with} \qquad -1 < \mu < 0. \tag{4.66}$$

Starting from $\boldsymbol{z}'_0$, we can continue iterating in the closed-loop system (3.39) with worst-case disturbances of the form (4.60) to obtain outer approximations of an arbitrary quantity of vertices

$$\begin{aligned} \boldsymbol{z}'_1 &= (\boldsymbol{A}+\boldsymbol{B}\boldsymbol{K})\boldsymbol{z}'_0 + \boldsymbol{B}\hat{u}_{(-1|\mathrm{L})} \\ \boldsymbol{z}'_2 &= (\boldsymbol{A}+\boldsymbol{B}\boldsymbol{K})\boldsymbol{z}'_1 + \boldsymbol{B}\hat{u}_{(-2|\mathrm{L})} \\ &\vdots \\ \boldsymbol{z}'_n &= (\boldsymbol{A}+\boldsymbol{B}\boldsymbol{K})\boldsymbol{z}'_{n-1} + \boldsymbol{B}\hat{u}_{(-n|\mathrm{L})} \\ &\vdots \end{aligned} \tag{4.67}$$

with decreasing estimation errors since the closed-loop matrix $\boldsymbol{A}+\boldsymbol{B}\boldsymbol{K}$ has poles with norm q less than one. We compare these vertices with the minimum RPI set obtained from [Rakovic 2005] in Fig. 4.2.

When the sequence $\hat{\boldsymbol{U}}_{\mathrm{L}}$ (4.59) is periodic, using it in (3.39), the tracking error $\tilde{\boldsymbol{x}}$ reaches some vertex $\boldsymbol{z}_0 \in \mathcal{Z}$ once each period T:

$$\boldsymbol{z}_0 = (\boldsymbol{A}+\boldsymbol{B}\boldsymbol{K})^T \boldsymbol{z}_0 + \sum_{h=0}^{T-1} (\boldsymbol{A}+\boldsymbol{B}\boldsymbol{K})^h \boldsymbol{B}\hat{u}_{(h|\mathrm{L})}. \tag{4.68}$$

Using such vertex $\boldsymbol{z}_0$ as starting point, and iterating with worst-case disturbances of the form

(4.60), we can obtain the vertices:

$$\begin{aligned} \boldsymbol{z}_1 &= (\boldsymbol{A}+\boldsymbol{B}\boldsymbol{K})\boldsymbol{z}_0 + \boldsymbol{B}\hat{u}_{(\text{-}1|\text{L})}, \\ \boldsymbol{z}_2 &= (\boldsymbol{A}+\boldsymbol{B}\boldsymbol{K})\boldsymbol{z}_1 + \boldsymbol{B}\hat{u}_{(\text{-}2|\text{L})}, \\ &\vdots \\ \boldsymbol{z}_0 &= (\boldsymbol{A}+\boldsymbol{B}\boldsymbol{K})\boldsymbol{z}_{T\text{-}1} + \boldsymbol{B}\hat{u}_{(\text{-}T|\text{L})}. \end{aligned} \tag{4.69}$$

4.5 Tracking Error and Constraints

Thanks to the bound (4.7) on the tracking error $\tilde{x}$, we can guarantee that all system constraints (3.42), (3.41) are satisfied as long as $\hat{u} \in \mathcal{V}$ by constraining the reference trajectory as:

$$x_{ref} \in \mathcal{X} \ominus \mathcal{Z}, \tag{4.70}$$
$$u_{ref} \in \mathcal{U} \ominus \boldsymbol{K}\mathcal{Z} \ominus \mathcal{V}, \tag{4.71}$$

where the symbol $\ominus$ represents a Pontryagin difference (Appx. A), these sets are non-empty if

$$\mathcal{Z} \subset \mathcal{X}, \tag{4.72}$$
$$\boldsymbol{K}\mathcal{Z} \oplus \mathcal{V} \subset \mathcal{U}. \tag{4.73}$$

Feasibility is guaranteed in this form up to a maximum uncertainty $\mathcal{V}_{max}$, defined when some tracking error bound (that we call the *limiting bound*) reaches a constraint boundary in (4.72), (4.73).

In Ch. 5, we will look for a feedback gain $\boldsymbol{K}$ to reduce specifically such limiting bound in order to extend these feasibility guarantees while reducing restrictiveness of the reference motion.

P→CĊ

Considering the constraints (2.27), (3.14), we obtain the conditions (4.72) and (4.73) to be:

$$\begin{bmatrix} 1 & 0 \end{bmatrix}\mathcal{Z} \subset \mathcal{C}, \tag{4.74}$$
$$\boldsymbol{K}\mathcal{Z} \oplus \mathcal{V} \subset \mathcal{P} - n \tag{4.75}$$

Since the tracking error $\tilde{x}$ satisfies the original dynamics (3.40) (see Sec. 3.5), having it stabilized (i.e., using the control law (3.33) with stable feedback gains (3.51), (3.52), (3.53)) physically means that when a tracking error of the CoM $\begin{bmatrix} \tilde{c} \\ \dot{\tilde{c}} \end{bmatrix} \in \mathcal{Z}$ is produced, we move the tracking error of the cCoP $\tilde{p}^c \in \boldsymbol{K}\mathcal{Z} \oplus \mathcal{V}$ even further to push it backwards:

$$\ddot{\tilde{c}} = \omega^2(\tilde{c} - \tilde{p}^c). \tag{4.76}$$

So, for stability, the set $\boldsymbol{K}\mathcal{Z} \oplus \mathcal{V}$ bounding the cCoP tracking error $\tilde{p}^c$ is bigger than the set $\begin{bmatrix} 1 & 0 \end{bmatrix}\mathcal{Z}$ bounding the CoM tracking error $\tilde{c}$. Moreover, in humanoid robots the compensated support polygon $\mathcal{P} - n$ (given by the foot size) is normally smaller than the kinematic constraint $\mathcal{C}$ (given by the leg length). So, the tracking error bound $\boldsymbol{K}\mathcal{Z} \oplus \mathcal{V}$ of the cCoP $\tilde{p}^c$ is the limiting bound.

P→X

Since this system does not include information of the CoM position, only the condition (4.73) applies:

$$k\mathcal{Z} \oplus \mathcal{V} \subset \mathcal{P} - n \tag{4.77}$$

and, therefore, the tracking error bound $k\mathcal{Z} \oplus \mathcal{V}$ of the cCoP $\tilde{p}^c$ is the limiting bound.

P_d→XP

Since this system does not include information of the CoM position, only the condition (4.72) applies:

$$\begin{bmatrix} 0 & 1 \end{bmatrix} \mathcal{Z} \subset \mathcal{P} - n \tag{4.78}$$

and, therefore, the tracking error bound $\begin{bmatrix} 0 & 1 \end{bmatrix} \mathcal{Z}$ of the cCoP $\tilde{p}^c$ is the limiting bound.

4.6 Discussion and Conclusions

When the robot is unable to execute specified control actions, we lose the control of the motion with unpredictable consequences due to its unstable dynamics. As the main result of this chapter, we can state conditions to guarantee robust feasibility, and thereby ensuring a safe operation of the robot:

- **On the control settings**, we must stabilize the closed-loop dynamics (4.1) of the tracking error using stable feedback gains $\boldsymbol{K}$ (Sec. 3.5.2), and we must design the reference constraints (4.70), (4.71) taking into account the tracking error bound $\tilde{x} \in \mathcal{Z}$.
- **On the operation**, we need bounded uncertainties $\hat{u} \in \mathcal{V}$ and feasible goal tasks (4.70), (4.71).

In order to generate all reference constraints without over-restricting the robot motion, we need a precise measure of the tracking error bound. Considering the tracking error $\boldsymbol{L}\tilde{\boldsymbol{x}}$ of an arbitrary linear combination of state variables, we have obtained three important results: the ratio r_{L} (4.34), (4.54), (4.58) that relates the upper bound $\boldsymbol{L}\boldsymbol{z}$ of this tracking error with the uncertainty of the system $\hat{u}_{\text{peak}}$; The WCS of disturbances $\hat{\boldsymbol{U}}_{\text{L}}$ (4.18); and based on the structure of $\hat{\boldsymbol{U}}_{\text{L}}$, we proposed an analytical form to compute the vertices of the minimum RPI set (4.52), (4.67), (4.69).

Comparing each tracking error bound with their constraints, we observed that the cCoP tracking error $\tilde{p}^c_{\text{peak}}$ is limiting the capability of the robot to handle bigger uncertainties or, equivalently, to allow less restrictive reference motions. So, in the next chapter, we focus particularly on reducing this tracking error bound.

Chapter 5

Robustness and Feedback Gains

5.1 Introduction

The goal of this chapter is to choose feedback gains to minimize the impact from uncertainty on the robot operation. This way, we maximize the set of uncertainty that the robot can handle safely while minimizing restrictiveness in the reference motion generation (4.70), (4.71).

In Sec. 5.2 we map different regions of stable gains depending on the behaviors of the WCS of disturbances described in the previous chapter. Focusing on the case of rigid ground interactions, in Sec. 5.3, we obtain the feedback gains that minimize the impact from disturbances on the robot operation, producing a bound on the tracking error which is independent from the sampling period. These results are validated in experiments and simulations using the humanoid robot Toro, developed at DLR, in section Sec. 5.4; where we also discuss the restrictiveness of the resulting control scheme. Considering a compliant ground interaction, in Sec. 5.5, we obtain numerically the minimum cCoP tracking error bound, which results smaller than in the rigid case for most standard compliance and sampling periods.

5.2 Map of Worst-Case Disturbances

As we discussed in Sec. 4.4, the WCS of disturbances $\hat{\boldsymbol{U}}_{\mathrm{L}}$ depends on the eigenstructure of the closed-loop matrix $\boldsymbol{A}+\boldsymbol{B}\boldsymbol{K}$, and coefficients α_1, α_2 of the particular ratio r_{L} that we are studying. Since the eigenstructure and coefficients depend ultimately on the feedback gain $\boldsymbol{K}$, we can map these behaviors onto the set of stable gains shown in Figs. 5.1 and 5.2, as follows.

5.2.1 Real-Valued and Complex Conjugate Poles

The relation between poles q and feedback gains $\boldsymbol{K}$ is defined by the characteristic equation

$$\det(q\boldsymbol{I}-\boldsymbol{A}-\boldsymbol{B}\boldsymbol{K})=0 \tag{5.1}$$

of the closed-loop system [Ogata 1995], where $\boldsymbol{I}$ is the identity matrix. For our second order systems it is:

$$\det(\boldsymbol{A}+\boldsymbol{B}\boldsymbol{K})-\operatorname{tr}(\boldsymbol{A}+\boldsymbol{B}\boldsymbol{K})q+q^2=0. \tag{5.2}$$

Solving this quadratic equation, the poles

$$q_{1,2}=\frac{\operatorname{tr}(\boldsymbol{A}+\boldsymbol{B}\boldsymbol{K})}{2}\pm\frac{\sqrt{\operatorname{tr}(\boldsymbol{A}+\boldsymbol{B}\boldsymbol{K})^2-4\det(\boldsymbol{A}+\boldsymbol{B}\boldsymbol{K})}}{2} \tag{5.3}$$

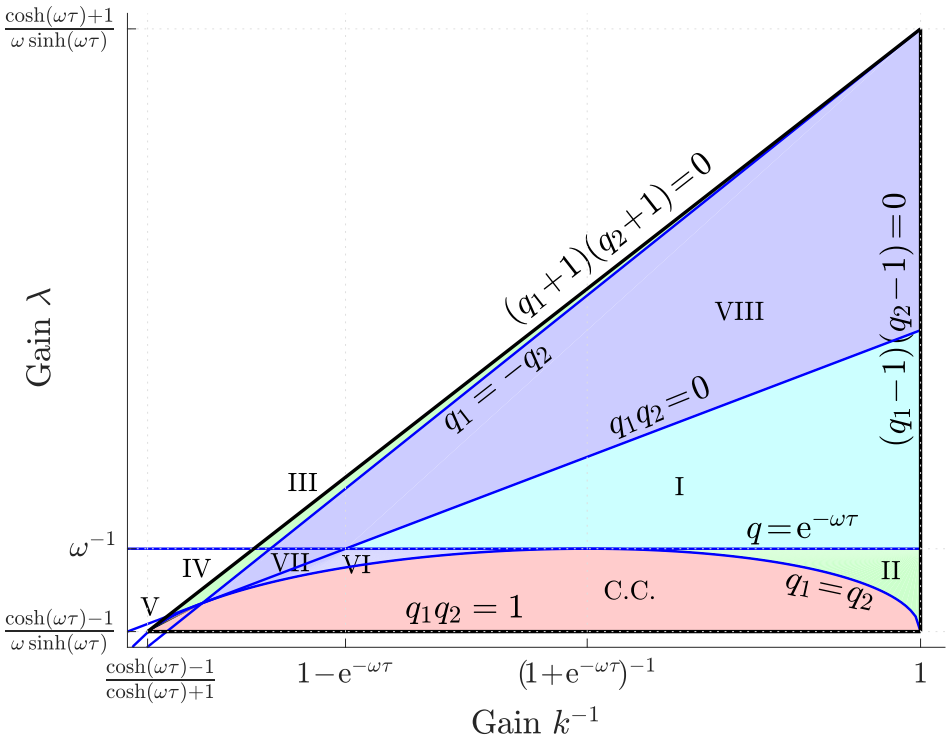

Figure 5.1: Map of behaviors for P→CC̈. This map is made for the cCoP tracking error $\tilde{p}^c$ considering the feedback law (3.33). We indicate with colors the cases to compute r described in Sec. 4.4: case **2** in green, case **3** in blue, case **4** in light blue and complex-conjugate poles in red. Tab. 5.1 characterizes each region.

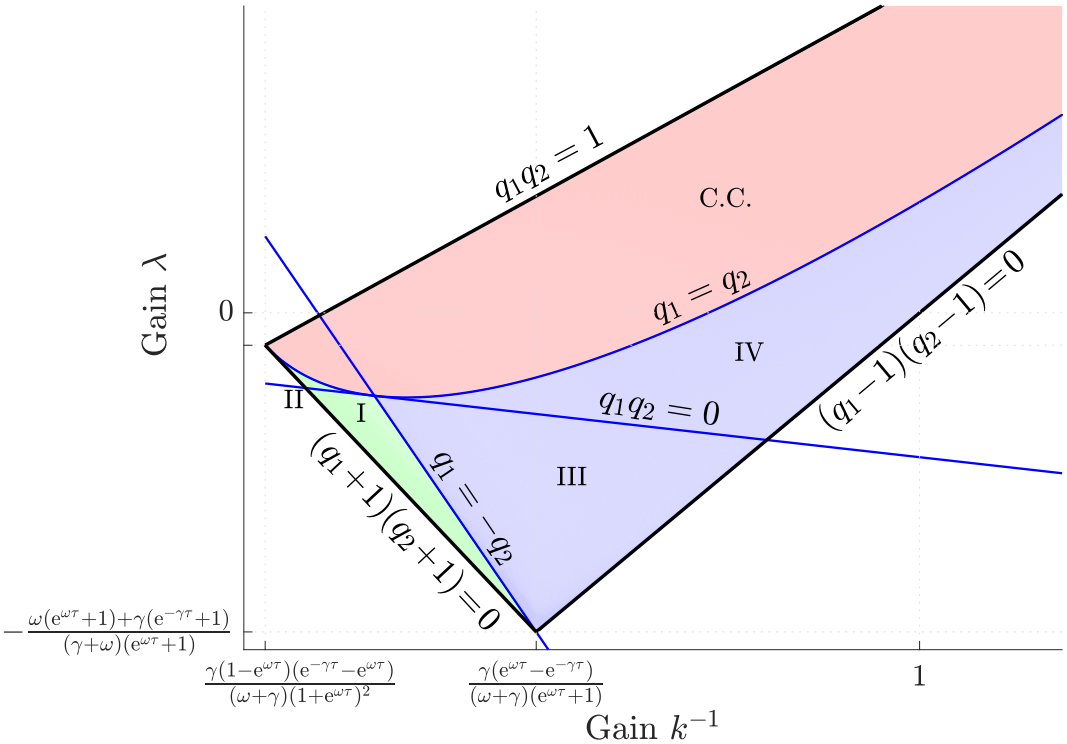

Figure 5.2: Map of behaviors for $\mathbf{P}_d$→XP. This map is made for the cCoP tracking error $\tilde{p}^c$ considering the feedback law (3.33). We indicate with colors the cases to compute r described in Sec. 4.4: case **2** in green, case **3** in blue and complex-conjugate poles in red. Tab. 5.2 characterizes each region.

P→CĊ

Region	q_m	q_{M}	$\lvert\alpha_m\rvert \gtrless \lvert\alpha_{\mathrm{M}}\rvert$	**Case**
I	+	+	$(\text{-})\alpha_m \gtrless (\text{-})\alpha_{\mathrm{M}}$	**4**
II	+	+	$(\text{+})\alpha_m \leq (\text{-})\alpha_{\mathrm{M}}$	**2**
III	+	-	$(\text{-})\alpha_m \leq (\text{-})\alpha_{\mathrm{M}}$	**2**
IV	+	-	$(\text{+})\alpha_m \leq (\text{-})\alpha_{\mathrm{M}}$	**2**
V	-	-	$(\text{+})\alpha_m > (\text{-})\alpha_{\mathrm{M}}$	**2**
VI	+	+	$(\text{-})\alpha_m > (\text{+})\alpha_{\mathrm{M}}$	**3**
VII	-	+	$(\text{-})\alpha_m > (\text{+})\alpha_{\mathrm{M}}$	**3**
VIII	-	+	$(\text{-})\alpha_m > (\text{-})\alpha_{\mathrm{M}}$	**3**

Table 5.1: Region conditions.

P_d→XP

Region	q_m	q_{M}	$\lvert\alpha_m\rvert \gtrless \lvert\alpha_{\mathrm{M}}\rvert$	**Case**
I	+	-	$(\text{-})\alpha_m \leq (\text{+})\alpha_{\mathrm{M}}$	**2**
II	-	-	$(\text{-})\alpha_m \leq (\text{+})\alpha_{\mathrm{M}}$	**2**
III	-	+	$(\text{+})\alpha_m > (\text{-})\alpha_{\mathrm{M}}$	**3**
IV	+	+	$(\text{+})\alpha_m > (\text{-})\alpha_{\mathrm{M}}$	**3**

Table 5.2: Region conditions.

are real-valued ($\Delta \geq 0$), or complex conjugate ($\Delta \leq 0$) depending on the discriminant

$$\Delta \equiv \mathrm{tr}(\boldsymbol{A}+\boldsymbol{B}\boldsymbol{K})^2 - 4\det(\boldsymbol{A}+\boldsymbol{B}\boldsymbol{K}). \tag{5.4}$$

This separates the set of stable feedback gains into two subsets with a frontier such that

$$\Delta = 0, \tag{5.5}$$

where both poles are equal $q_1 = q_2 = q_*$ and from (5.3), the trace is

$$\mathrm{tr}(\boldsymbol{A}+\boldsymbol{B}\boldsymbol{K}) = 2q_*. \tag{5.6}$$

Considering gains of the form (3.34), this frontier describes a curve in coordinates (k^{-1}, λ) as shown in Figs. 5.1 and 5.2. Combining expressions (5.5) and (5.6) we can parameterize this curve with the value of the pole $q_* \in \{\text{-}1,\ 1\}$.

5.2.2 Equal Magnitude Poles

Coefficients α_1, α_2 are defined from the eigenvectors $\boldsymbol{M}_{\mathtt{c},1}$, $\boldsymbol{M}_{\mathtt{c},2}$ (4.24) associated to poles q_1 and q_2 respectively. Working with real-valued poles, we rename them such that $|q_{\mathrm{M}}| > |q_m|$. Since cases **2** and **3** described in Sec.4.4.1 depend on the ordinal relation $|\alpha_{\mathrm{M}}| \lesseqgtr |\alpha_m|$, when the order between poles q_1, q_2 is inverted, the coefficients α_m and α_{M} exchange names accordingly, switching between cases **2** and **3** (or between **2** and **1** when some α is 0). On the frontier between regions of feedback gains with different pole orders, both poles must have the same magnitude. Since the curve (5.5) with equal poles $q_1 = q_2$ cannot produce this separation (it is not crossing the region of real-valued poles), we look for gains where the poles are opposite $q_1 = \text{-}q_2$:

$$q_1 + q_2 = \mathrm{tr}(\boldsymbol{A}+\boldsymbol{B}\boldsymbol{K}) = 0. \tag{5.7}$$

Considering the vectors $\boldsymbol{B}$ and $\boldsymbol{K}$ (3.34):

$$\boldsymbol{B} = \begin{bmatrix} b_1 \\ b_2 \end{bmatrix}, \qquad \boldsymbol{K} = k\begin{bmatrix} 1 & \lambda \end{bmatrix}, \tag{5.8}$$

the trace is:

$$\begin{aligned} \mathrm{tr}(\boldsymbol{A}+\boldsymbol{B}\boldsymbol{K}) &= \mathrm{tr}(\boldsymbol{A}) + \mathrm{tr}(\boldsymbol{B}\boldsymbol{K}) \\ &= \mathrm{tr}(\boldsymbol{A}) + \boldsymbol{K}\boldsymbol{B} \\ &= \mathrm{tr}(\boldsymbol{A}) + b_1 k + b_2 k\lambda, \end{aligned} \tag{5.9}$$

so, opposite poles (5.7) represent a line in coordinates (k^{-1}, λ):

$$\mathrm{tr}(\boldsymbol{A})k^{-1} + b_2\lambda + b_1 = 0, \tag{5.10}$$

as shown in Figs. 5.1 and 5.2.

5.2.3 Equal and Opposite Sign Poles

The case **4** described in Sec. 4.4.1 requires both poles with the same sign $q_1 q_2 > 0$ (and both coefficients $\alpha_1\alpha_2 > 0$, what will be discussed in Sec. 5.2.7). The frontier between poles with equal and opposite sign is when one of the poles is zero:

$$q_1 q_2 = \det(\boldsymbol{A} + \boldsymbol{B}\boldsymbol{K}) = 0. \tag{5.11}$$

Considering vectors of the form (5.8) and the matrix

$$\boldsymbol{A} = \begin{bmatrix}\boldsymbol{A}_{\mathsf{c},1} & \boldsymbol{A}_{\mathsf{c},2}\end{bmatrix} = \begin{bmatrix}a_{11} & a_{12}\\ a_{21} & a_{22}\end{bmatrix}, \tag{5.12}$$

we can see that this determinant is

$$\begin{aligned}\det(\boldsymbol{A} + \boldsymbol{B}\boldsymbol{K}) &= (a_{11} + b_1 k)(a_{22} + b_2 k\lambda) - (a_{12} + b_1 k\lambda)(a_{21} + b_2 k)\\ &= a_{11}a_{22} - a_{12}a_{21} + (a_{11}b_2 - a_{21}b_1)k\lambda - (a_{12}b_2 - a_{22}b_1)k\\ &= \det(\boldsymbol{A}) + \det\begin{bmatrix}\boldsymbol{A}_{\mathsf{c},1} & \boldsymbol{B}\end{bmatrix}k\lambda - \det\begin{bmatrix}\boldsymbol{A}_{\mathsf{c},2} & \boldsymbol{B}\end{bmatrix}k.\end{aligned} \tag{5.13}$$

So, this frontier (5.11) corresponds to a line in coordinates (k^{-1}, λ):

$$\det(\boldsymbol{A})k^{-1} + \det\begin{bmatrix}\boldsymbol{A}_{\mathsf{c},1} & \boldsymbol{B}\end{bmatrix}\lambda - \det\begin{bmatrix}\boldsymbol{A}_{\mathsf{c},2} & \boldsymbol{B}\end{bmatrix} = 0, \tag{5.14}$$

as shown in Figs. 5.1 and 5.2.

5.2.4 Gains for a Given Pole

Having one pole with an arbitrary real value q_*, corresponds to a set of feedback gains satisfying

$$\det(\boldsymbol{A} + \boldsymbol{B}\boldsymbol{K}) - \mathrm{tr}(\boldsymbol{A} + \boldsymbol{B}\boldsymbol{K})q_* + q_*^2 = 0, \tag{5.15}$$

we can see from the trace (5.9) and determinant (5.13) that this is equivalent to:

$$\begin{aligned}\det(\boldsymbol{A}) + \det\begin{bmatrix}\boldsymbol{A}_{\mathsf{c},1} & \boldsymbol{B}\end{bmatrix}k\lambda - \det\begin{bmatrix}\boldsymbol{A}_{\mathsf{c},2} & \boldsymbol{B}\end{bmatrix}k - \mathrm{tr}(\boldsymbol{A})q_* - b_1 k q_* - b_2 k\lambda q_* + q_*^2 = 0\\ \big(\det(\boldsymbol{A}) - \mathrm{tr}(\boldsymbol{A})q_* + q_*^2\big)k^{-1} + \Big(\det\begin{bmatrix}\boldsymbol{A}_{\mathsf{c},1} & \boldsymbol{B}\end{bmatrix} - b_2 q_*\Big)\lambda - b_1 q_* - \det\begin{bmatrix}\boldsymbol{A}_{\mathsf{c},2} & \boldsymbol{B}\end{bmatrix} = 0,\end{aligned} \tag{5.16}$$

so this set of feedback gains $\boldsymbol{K}$ represents a line in coordinates (k^{-1}, λ). As an example, the stability margins in Fig. 5.1 and Fig. 5.2 are lines defined by $q_* = 1$ and $q_* = -1$.

For simplicity we rewrite this expression as

$$\sigma_{(*,0)}k^{-1} + \sigma_{(*,1)}\lambda + \sigma_{(*,2)} = 0, \tag{5.17}$$

gathering all parameters in coefficients $\sigma_{(*,0)}$, $\sigma_{(*,1)}$ and $\sigma_{(*,2)}$ that depend on the fixed pole q_* as indicated in their subscripts.

5.2.5 Intersections of Given Pole Lines

The line defined by any real-valued pole q_* intersects the curve of equal poles (5.5) when $q_1 = q_2 = q_*$ at some feedback gain $\boldsymbol{K}$ satisfying both expressions:

$$\sigma_{(*,0)}k^{-1} + \sigma_{(*,1)}\lambda + \sigma_{(*,2)} = 0, \tag{5.18}$$

$$\mathrm{tr}(\boldsymbol{A} + \boldsymbol{B}\boldsymbol{K})^2 - 4\det(\boldsymbol{A} + \boldsymbol{B}\boldsymbol{K}) = 0, \tag{5.19}$$

This intersection can only be tangent to the curve (5.19) since the line (5.18) is defined by a real-valued pole. Notice that on the point of tangency, the pole q_* used to define the line is also the parameter of the curve. Any other point in the region with real-valued poles can be understood as the intersection

$$\sigma_{(1,0)}k^{-1} + \sigma_{(1,1)}\lambda + \sigma_{(1,2)} = 0, \tag{5.20}$$

$$\sigma_{(2,0)}k^{-1} + \sigma_{(2,1)}\lambda + \sigma_{(2,2)} = 0, \tag{5.21}$$

between two lines tangent to the curve (5.5), defined by poles q_1 and q_2. So, we can determine the two poles of any point in the region of real-valued poles by simple identification of the two tangents to (5.5) that croiss such point.

5.2.6 Interpreting Plots

We can recognize visually the distribution of poles in Figs. 5.1 and 5.2 considering the recap of previous results:

- ***a)*** Every line, tangent to the curve (5.5), maintains one pole constant with the value of the pole q_* in the point of tangency.
- ***b)*** The curve of equal poles (5.5) is parameterized by the pole q_*. Varing q_* from -1 to 1, this curve goes from one vertex to another of the set of stable gains.
- ***c)*** Every point in the region with real-valued poles is the intersection of two lines tangent to the curve (5.5). These two lines define the two poles obtained at such point.

Let's exemplify this on the map of behaviors shown in the Fig. 5.3. From ***a)***, we can observe that on top of the curve, the parameter $q_* = \mathrm{e}^{-\omega\tau}$ is given by the horizontal line. From ***b)***, the parameter decreases to the left reaching $q_* = 0$ on the intersection with the frontier line $q_1 q_2 = 0$. So, for any point in this segment we have

$$0 \leq q_a \leq \mathrm{e}^{-\omega\tau}. \tag{5.22}$$

Towards the right, the parameter grows up to $q_* = 1$ on the intersection with the stability limit. So, for any point in this segment we have

$$\mathrm{e}^{-\omega\tau} \leq q_b \leq 1. \tag{5.23}$$

Noticing that every point in the region I is the intersection of one tangent to the segment (5.22) and one tangent to the segment (5.23) (as in the illustrated example). From ***c)***, we have that poles in region I are both positive, with one bigger and one smaller than $\mathrm{e}^{-\omega\tau}$. Similarly, we can see that every point in region II is the intersection of two tangents to the segment (5.23) only, concluding that poles in region II are both bigger than $\mathrm{e}^{-\omega\tau}$.

In the following, we detail the frontier curves between different regions for each system:

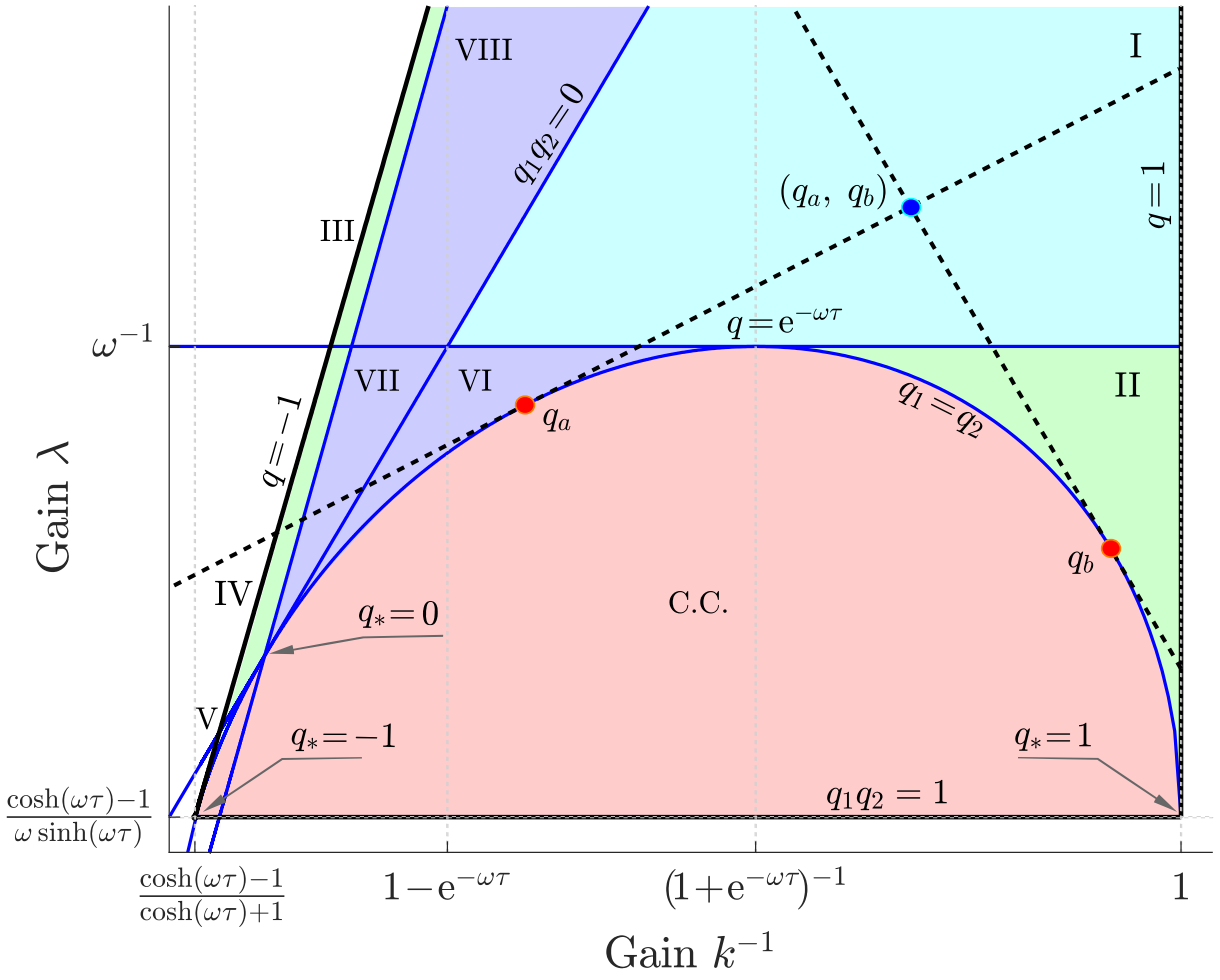

Figure 5.3: Tangent lines for P→CC̀. We show how to recognize visually the distribution of poles based on lines tangent to the frontier between complex-conjugate and real-valued poles.

P→CĊ

From the trace (3.50) and determinant (3.49) of the closed-loop matrix, we obtain: The frontier between regions with real-valued and complex conjugate poles ($\Delta = 0$) (5.5) is with

$$\lambda = \frac{\left((2k^{-1}-1)\sqrt{\cosh(\omega\tau)-1}+2\sqrt{2k^{-1}(1-k^{-1})}\right)}{\omega\sinh(\omega\tau)}\sqrt{\cosh(\omega\tau)-1}. \tag{5.24}$$

The frontier between regions with equal and opposite sign poles ($q_1 q_2 = 0$) (5.11) is with

$$\lambda = \frac{\cosh(\omega\tau)-1+k^{-1}}{\omega\sinh(\omega\tau)}. \tag{5.25}$$

The poles have opposite values ($q_1 + q_2 = 0$) with gains that satisfy (5.7)

$$\lambda = \frac{(2k^{-1}-1)\cosh(\omega\tau)+1}{\omega\sinh(\omega\tau)}. \tag{5.26}$$

P→X

The pole (3.54) changes its sign ($q = 0$) when

$$k = \frac{\mathrm{e}^{\omega\tau}}{\mathrm{e}^{\omega\tau}-1}. \tag{5.27}$$

$\mathbf{P}_d$→XP

From the trace (3.57) and determinant (3.56) of the closed-loop matrix, we obtain: The frontier between regions with real-valued and complex-conjugate poles ($\Delta = 0$) (5.5) is with

$$\lambda = \left(\sqrt{\left(\mathrm{e}^{(\gamma+\omega)\tau}-1\right)k^{-1}}-\sqrt{\frac{\gamma(\mathrm{e}^{\omega\tau}-1)\mathrm{e}^{\gamma\tau}}{\gamma+\omega}}\right)^2(\mathrm{e}^{\gamma\tau}-1)-\frac{\omega}{\gamma+\omega}. \tag{5.28}$$

The frontier between regions with equal and opposite sign poles ($q_1 q_2 = 0$) (5.11) is with

$$\lambda = \frac{1-k^{-1}}{\mathrm{e}^{\gamma\tau}-1}-\frac{\gamma\mathrm{e}^{-\omega\tau}+\omega\mathrm{e}^{\gamma\tau}}{(\gamma+\omega)(\mathrm{e}^{\gamma\tau}-1)}. \tag{5.29}$$

The poles have opposite values ($q_1 + q_2 = 0$) with gains that satisfy (5.7)

$$\lambda = \frac{1+\mathrm{e}^{(\gamma+\omega)\tau}}{1-\mathrm{e}^{\gamma\tau}}k^{-1}-\frac{\gamma(\mathrm{e}^{\omega\tau}-1)\mathrm{e}^{\gamma\tau}}{(\gamma+\omega)(1-\mathrm{e}^{\gamma\tau})}-\frac{\omega}{\gamma+\omega}. \tag{5.30}$$

5.2.7 cCoP Tracking Error Bound Ratio

As we concluded in Sec. 4.5, our priority is to minimize the impact from disturbances $\hat{u} \in \mathcal{V}$ on the cCoP tracking error bound $\tilde{p}^c_{\text{peak}}$. So, we focus on the ratio (4.10), (4.12), (4.13):

$$r \equiv \frac{\tilde{p}^c_{\text{peak}}}{\hat{u}_{\text{peak}}}. \tag{5.31}$$

Considering this ratio, we can obtain the coefficients α_m and α_{M} to include in our maps the frontiers between cases discussed in Sec. 4.4.1 ($\alpha_m = 0$, $\alpha_{\text{M}} = 0$, $|\alpha_{\text{M}}| = |\alpha_m|$).

Only with P→CĊ there is a separation of cases due to these limits corresponding to $\alpha_m = 0$ and $\alpha_{\text{M}} = 0$. We describe the frontier for this case only:

P→CĊ

Consider the eigenvector $\boldsymbol{V} = \left[\begin{smallmatrix} -\omega^{-1} \\ 1 \end{smallmatrix}\right]$ of the matrix $\boldsymbol{A}$ (3.27) associated to its stable eigenvalue $q = \mathrm{e}^{-\omega\tau}$:

$$\boldsymbol{A}\boldsymbol{V} = q\boldsymbol{V}. \tag{5.32}$$

When $\lambda = \omega^{-1}$, feedback gains of the form (3.34) $\boldsymbol{K} = k\begin{bmatrix}1 & \omega^{-1}\end{bmatrix}$ are orthogonal to V, therefore, we have

$$(\boldsymbol{A} + \boldsymbol{B}\boldsymbol{K})\boldsymbol{V} = \boldsymbol{A}\boldsymbol{V} = q\boldsymbol{V}, \tag{5.33}$$

which means that $\boldsymbol{V}$ and q are an eigenvector and a pole of the closed-loop matrix as well. Hence, from the diagonalization (4.22), $\boldsymbol{M}_{\text{c},1} = \boldsymbol{V}$ is a column of $\boldsymbol{M}$ and the respective coefficient is

$$\alpha_1 = \boldsymbol{K}\boldsymbol{M}_{\text{c},1}\boldsymbol{M}_{\text{r},1}^{-1}\boldsymbol{B} = 0. \tag{5.34}$$

5.3 Torque-Controlled Robot on Rigid Ground

A rigid ground is the most common scenario for robots that work indoors. Typically, a fast force control is also desired for the safety of the robot and its environment, specially when managing expensive instruments or collaborating with humans.

In this section, we focus on this configuration to study in more detail, and minimize, the effect of different uncertainty sources on the tracking error using systems P→CĊ and P→X. In particular, we consider the torque-controlled humanoid robot Toro developed at DLR, but the proposed mathematical results apply indistinctly to torque-controlled legged robots in general.

5.3.1 Tracking Error and Gain Regions

From (5.31), the cCoP tracking error bound, expressed in terms of all uncertainty sources (3.36) is

$$\tilde{p}^c_{\text{peak}} = r(\hat{a}_{\text{peak}} + \hat{n}_{\text{peak}}) + rk(\hat{c}_{\text{peak}} + \lambda\hat{\dot{c}}_{\text{peak}}). \tag{5.35}$$

When we have only actuation errors ($\hat{c}_{\text{peak}} = \hat{\dot{c}}_{\text{peak}} = 0$), $\tilde{p}^c_{\text{peak}}$ is related to feedback gains $\boldsymbol{K}$ only through the ratio r. Using the results obtained in Sec. 4.4, we present in Fig. 5.4 the ratio r (5.31) on the entire set of stable gains $\boldsymbol{K}$. We can see that it tends to infinity when gains approach the stability boundaries and has a minimum value for poles $q_1 = 0$, $q_2 = \mathrm{e}^{-\omega\tau}$ that correspond to the feedback gain

$$\boldsymbol{K} = \frac{1}{1 - \mathrm{e}^{-\omega\tau}}\begin{bmatrix}1 & \omega^{-1}\end{bmatrix}. \tag{5.36}$$

With an estimation error $\hat{c}$, we can expect the minimum of $\tilde{p}^c_{\text{peak}}$ to be with smaller values of k (bigger k^{-1}), and with some estimation error $\hat{\dot{c}}$, smaller values of λ. We generate the level curves of cCoP tracking error shown in Fig. 5.5 considering, as an example the proportion between uncertainty sizes:

$$\hat{a}_{\text{peak}} + \hat{n}_{\text{peak}} = \hat{c}_{\text{peak}} + \frac{\hat{\dot{c}}_{\text{peak}}}{\omega}, \tag{5.37}$$

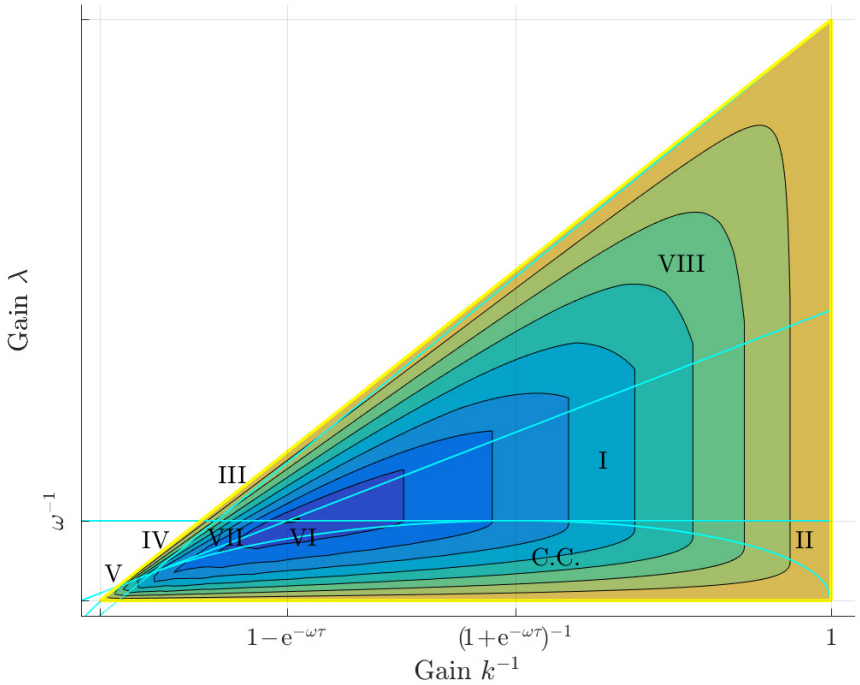

Figure 5.4: Level curves of the ratio r. The minimum ratio r is reached with $k^{-1} = 1 - e^{-\omega\tau}$ and $\lambda = \omega^{-1}$ shown in black, and its values grow towards infinity on the stability boundary shown in yellow. We also overlay the map of regions discussed earlier.

in order to weight similarly actuation and estimation errors, using ω to match units. Other proportions exhibit similar level curves for $\tilde{p}^{c}_{\text{peak}}$ with minimum values in or close to $\lambda = \omega^{-1}$. This choice ($\lambda = \omega^{-1}$) is particularly interesting since it has been shown to maximize controllability in [Sugihara 2009] where it is called "the best CoM-CoP regulator", and became, therefore, a standard control choice [Morisawa 2012], [Englsberger 2011].

5.3.2 Optimal Gains

In the system P→CĊ, feedback gains of the form

$$\boldsymbol{K} = k\begin{bmatrix}1 & \omega^{-1}\end{bmatrix}, \tag{5.38}$$

produce the poles

$$q_1 = e^{-\omega\tau}, \qquad q_2 = e^{\omega\tau} + k(1 - e^{\omega\tau}), \tag{5.39}$$

obtained from the determinant (3.49) and trace (3.50) of the closed-loop matrix $\boldsymbol{A} + \boldsymbol{B}\boldsymbol{K}$. For $\lambda = \omega^{-1}$, moreover, we have obtained in (5.34) that

$$\alpha_1 = \boldsymbol{K}\boldsymbol{M}_{\mathrm{c},1}\boldsymbol{M}_{\mathrm{r},1}^{-1}\boldsymbol{B} = 0, \tag{5.40}$$

and α_2 can be obtained from the product:

$$\begin{aligned}\boldsymbol{K}\boldsymbol{B} &= \boldsymbol{K}\boldsymbol{M}\boldsymbol{M}^{-1}\boldsymbol{B}\\ &= \boldsymbol{K}\boldsymbol{M}_{\mathrm{c},1}\boldsymbol{M}_{\mathrm{r},1}^{-1}\boldsymbol{B} + \boldsymbol{K}\boldsymbol{M}_{\mathrm{c},2}\boldsymbol{M}_{\mathrm{r},2}^{-1}\boldsymbol{B}\\ &= \alpha_1 + \alpha_2\\ &= \alpha_2 = k(1 - e^{\omega\tau}).\end{aligned} \tag{5.41}$$

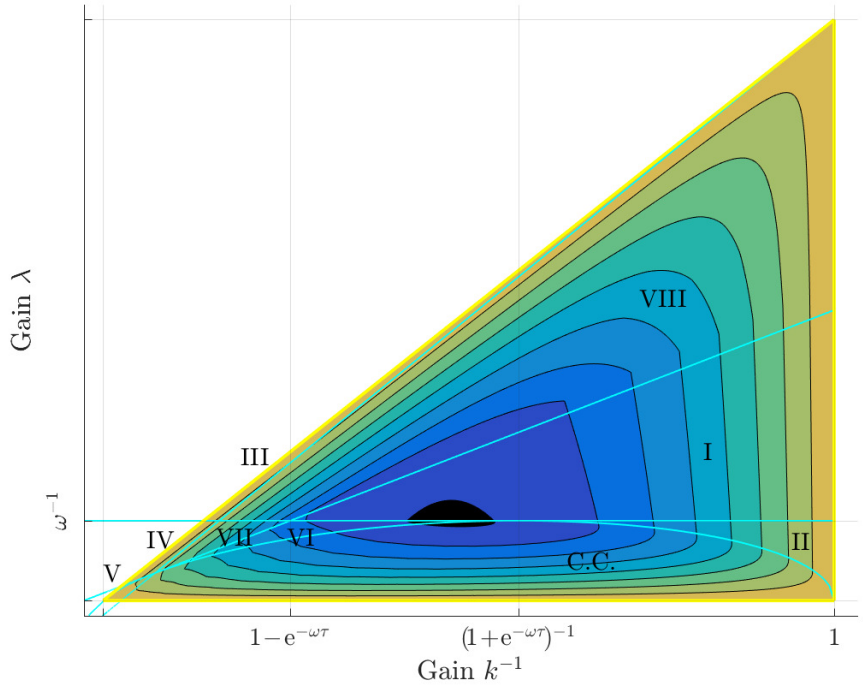

Figure 5.5: Level curves of the tracking error bound $\tilde{p}^c_{\text{peak}}$. Using the proportion of uncertainties (5.37), The minimum cCoP tracking error $\tilde{p}^c_{\text{peak}}$, shown in black, is reached with $\lambda = \omega^{-1}$ and its values grow towards infinity on the stability boundary shown in yellow. We also overlay the map of regions discussed earlier.

So, the ratio r is the sum (4.23):

$$r = \frac{\tilde{p}^c_{\text{peak}}}{\hat{u}_{\text{peak}}} = \sum_{i=0}^{\infty} |q_2 \alpha_2| + 1, \tag{5.42}$$

that converges to (4.34):

$$r = \frac{k(e^{\omega\tau} - 1)}{1 - |q_2|} + 1, \tag{5.43}$$

and depending on the sign of q_2 it is:

$$r = \begin{cases} \frac{1}{k-1} + 2 & \text{if} \quad e^{\omega\tau} - 1 \leq \frac{1}{k-1}, \qquad (q_2 \geq 0), \\ \frac{2+(e^{\omega\tau}-1)}{2-(k-1)(e^{\omega\tau}-1)} & \text{if} \quad \frac{1}{k-1} \leq e^{\omega\tau} - 1 < \frac{2}{k-1}, \qquad (q_2 \leq 0), \end{cases} \tag{5.44}$$

defined within the stability limits (3.52), (3.53) with $\lambda = \omega^{-1}$.

On the other hand, the system P→X has only one pole obtained in (3.54):

$$q = \boldsymbol{A} + \boldsymbol{B}k = e^{\omega\tau} + k(1 - e^{\omega\tau}), \tag{5.45}$$

so, from the summation (4.21), the ratio r is

$$r = \frac{\tilde{p}^c_{\text{peak}}}{\hat{u}_{\text{peak}}} = \sum_{i=0}^{\infty} |k\, q\, (1 - e^{\omega\tau})| + 1, \tag{5.46}$$

that coincides with the ratio (5.42) for the system P→C$\dot{\text{C}}$, and therefore converges to (5.44).

Since gains of the form (5.38) feedback the DCM (2.18) ξ on P→CĊ, we can see that both systems (P→CĊ and P→X) result with the same control law (3.33):

$$u = p^c = p^c_{ref} + k\tilde{\xi} + \hat{u}, \tag{5.47}$$

the same uncertainty (3.36):

$$\hat{u} = \hat{a} - \hat{n} - k\hat{\xi} \in \mathcal{V}, \tag{5.48}$$

and the same cCoP tracking error bound (4.12):

$$\tilde{p}^c_{\text{peak}} = r(\hat{a}_{\text{peak}} + \hat{n}_{\text{peak}}) + rk\hat{\xi}_{\text{peak}}. \tag{5.49}$$

Considering the ratio r with $q_2 \geq 0$ in (5.44) (region I), the derivatives of this tracking error are

$$\frac{d\tilde{p}^c_{\text{peak}}}{dk} = \frac{\big(2(k-1)^2 - 1\big)\hat{\xi}_{\text{peak}} - \hat{n}_{\text{peak}} - \hat{a}_{\text{peak}}}{(k-1)^2}, \tag{5.50}$$

$$\frac{d^2\tilde{p}^c_{\text{peak}}}{dk^2} = \frac{2}{(k-1)^3}(\hat{n}_{\text{peak}} + \hat{a}_{\text{peak}} + \hat{\xi}_{\text{peak}}). \tag{5.51}$$

Since $\frac{d^2\tilde{p}^c_{\text{peak}}}{dk^2}$ is positive for any stable gain k (3.55), the minimum tracking error

$$\tilde{p}^{c*}_{\text{peak}} = \left(\sqrt{\hat{\xi}_{\text{peak}}} + \sqrt{2(\hat{a}_{\text{peak}} + \hat{n}_{\text{peak}} + \hat{\xi}_{\text{peak}})}\right)^2 \tag{5.52}$$

is obtained using a feedback gain k^* such that $\frac{\tilde{p}^c_{\text{peak}}}{dk} = 0$:

$$k^* = 1 + \sqrt{\frac{\hat{a}_{\text{peak}} + \hat{n}_{\text{peak}} + \hat{\xi}_{\text{peak}}}{2\hat{\xi}_{\text{peak}}}}. \tag{5.53}$$

Taking typical uncertainty sizes [Flayols 2017] as:

$$\hat{n}_{\text{peak}} + \hat{a}_{\text{peak}} = \hat{\xi}_{\text{peak}} = 0.5 \text{ cm}, \tag{5.54}$$

the optimal gain is $k^* = 2$, and the minimal bound of the cCoP tracking error $\tilde{p}^{c*}_{\text{peak}} = 4.5$ cm, as shown in Fig. 5.6, that corresponds to the half-width of Toro's feet.

Notice that, as a result of the expression of r (5.44), once the feedback gain has been chosen, the cCoP tracking error bound $\tilde{p}^{c*}_{\text{peak}}$ does not depend on the sampling period τ as long as it is shorter than

$$\tau_0 = \omega^{-1} \ln\left(\frac{1}{k-1} + 1\right). \tag{5.55}$$

The tracking error bound $\tilde{p}^{c*}_{\text{peak}}$ is not improved by reducing the sampling period below this value, but it degrades sharply when $\tau > \tau_0$, as shown in Fig. 5.6. For the robot Toro ($\omega \approx 3.2\text{s}^{-1}$), $\tau_0 = 216$ ms.

5.3.3 Independence of the sampling period

The independence of the sampling period observed in (5.44) when $\lambda = \omega^{-1}$, is actually a property of feedback gains in regions I and II as we show in following:

From Tab. 5.1, in regions I and II, the WCS of disturbances $\hat{\boldsymbol{U}}_{\text{L}} = \hat{\boldsymbol{U}}_0$ is a constant disturbance $\hat{u}_{\text{peak}}$ ($n = 0$ with $q_{\text{M}} > 0$). Hence, the tracking error (4.10) converges to the stationary value (see Sec.4.4.1.4):

$$\tilde{p}^c_{\text{peak}} = |\boldsymbol{K}\boldsymbol{z}_0| + \hat{u}_{\text{peak}}, \tag{5.56}$$

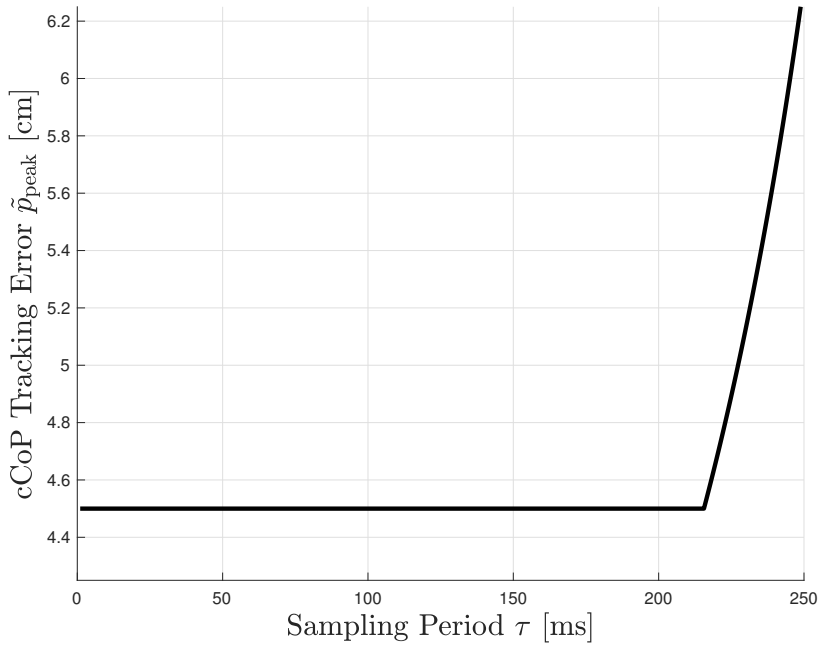

Figure 5.6: Relation between cCoP tracking error bound and sampling period. The cCoP tracking error bound produced by actuation and estimation errors of up to 0.5 cm, using the optimal gains $k^* = 2$ and $\lambda = \omega^{-1}$ ($\omega \approx 3.2\text{s}^{-1}$ for Toro) for different sampling periods τ.

where the vertex $\boldsymbol{z}_0$ satisfies (4.46):

$$\boldsymbol{z}_0 = (\boldsymbol{A} + \boldsymbol{B}\boldsymbol{K})\boldsymbol{z}_0 + B\hat{u}_{\text{peak}}, \tag{5.57}$$

which can be easily obtained:

$$\boldsymbol{z}_0 = \begin{bmatrix} \tilde{c}_0 \\ \dot{\tilde{c}}_0 \end{bmatrix} = \begin{bmatrix} \frac{\hat{u}_{\text{peak}}}{1-k} \\ 0 \end{bmatrix}. \tag{5.58}$$

The ratio r defined in (5.31) is

$$r = \frac{|\boldsymbol{K}\boldsymbol{z}_0|}{\hat{u}_{\text{peak}}} + 1 = \frac{1}{k-1} + 2, \tag{5.59}$$

which is independent from λ, ω and τ for gains in regions I and II.

Proof. Let's demonstrate formally that regions I and II correspond to cases **2** and **4** ($n = 0$). As indicated in (4.28) and (4.36) it implies that

$$\text{sign}(\alpha_m q_m^i + \alpha_{\text{M}} q_{\text{M}}^i) = \text{sign}(\alpha_{\text{M}} q_{\text{M}}^i) \qquad \forall\, i \geq 0 \tag{5.60}$$

the sign of every addend in the infinite sum (4.23) coincides with the sign of the term associated to the bigger eigenvalue q_{M}.

Rewriting the addend in (4.23) we have

$$\alpha_m q_m^i + \alpha_{\text{M}} q_{\text{M}}^i = (\alpha_m + \alpha_{\text{M}}) q_m^i + \alpha_{\text{M}}(q_{\text{M}}^i - q_m^i), \tag{5.61}$$

the first term is negative since we can observe from (4.24) that

$$\alpha_m + \alpha_{\text{M}} = \boldsymbol{K}\boldsymbol{B} \tag{5.62}$$

$$= k - k\cosh(\omega\tau) - k\lambda\omega\sinh\omega\tau \tag{5.63}$$

$$= q_m + q_{\text{M}} - 2\cosh(\omega\tau) < 0, \tag{5.64}$$

where the last equality follows from (3.50). With the help of a computer algebra system, we can obtain

$$\alpha_m = \frac{1-q_m}{(k-1)(q_m-q_{\mathrm{M}})}(q_m q_{\mathrm{M}} - 1 + k(1-q_m)), \tag{5.65}$$

$$\alpha_{\mathrm{M}} = \frac{1-q_{\mathrm{M}}}{(k-1)(q_{\mathrm{M}}-q_m)}(q_m q_{\mathrm{M}} - 1 + k(1-q_{\mathrm{M}})). \tag{5.66}$$

Having α_{M} also negative would complete the proof. The fraction on the left is positive, so α_{M} has the same sign as the factor on the right. From (3.49), in region I ($\lambda \geq \omega^{-1}$) we have:

$$q_m q_{\mathrm{M}} - 1 + k(1-q_{\mathrm{M}}) = k(\cosh(\omega\tau) - \lambda\omega\sinh(\omega\tau) - q_{\mathrm{M}}) \tag{5.67}$$

$$\leq k(\mathrm{e}^{-\omega\tau} - q_{\mathrm{M}}). \tag{5.68}$$

Region II ($\lambda \leq \omega^{-1}$) satisfies that $k \leq 1 + \mathrm{e}^{-\omega\tau}$, so

$$q_{\mathrm{M}} - 1 + k(1-q_{\mathrm{M}}) \leq q_{\mathrm{M}}^2 - 1 + k(1-q_{\mathrm{M}}) \tag{5.69}$$

$$\leq (1-q_{\mathrm{M}})(k-1-q_{\mathrm{M}}) \tag{5.70}$$

$$\leq (1-q_{\mathrm{M}})(\mathrm{e}^{-\omega\tau} - q_{\mathrm{M}}). \tag{5.71}$$

In both cases, this factor is negative since at least one pole is greater or equal to $\mathrm{e}^{-\omega\tau}$ in these regions (check the example in Sec. 5.2.6), so $q_{\mathrm{M}} \geq \mathrm{e}^{-\omega\tau}$, and $n = 0$ follows.

□

Notice that the stationary vertex $\boldsymbol{z}_0$ satisfies the equilibrium condition of the system dynamics (3.1) in the tracking error space, as mentioned in Sec. 3.5. It is, zero velocity $\dot{\tilde{c}}_0 = \tilde{\dot{c}}_0 = 0$, and CoM coinciding with cCoP $\tilde{p}^c_{\mathrm{peak}} = \tilde{c}_0$.

5.3.4 Uncompensated Vertical Motion (a preliminary discussion)

Variations in the vertical motion c^z, $\ddot{c}^z$, g^z, f_{e}^z affect the ^{x,y} components of the CoM acceleration $\ddot{c}$. As we discussed in Sec. 3.3, the WBC must compensate for them based on estimated values c'^z, $\ddot{c}'^z$, g'^z, $f_{\mathrm{e}}'^z$ to maintain the linear CoM dynamics (3.10), which is detailed in [Brasseur 2015]. Errors in this estimation, however, have two effects: the first one is a disturbance of the form $\hat{n}$ that has been discussed in Sec. 3.3.1; as a second effect, they modify the linear dynamics (3.10) producing the parameter ω to vary with time between some bounds $\omega_{min} \leq \omega \leq \omega_{max}$. Since the set of stable gains and all regions depend on ω as shown in Fig. 5.1, our fixed choice of feedback gain is not optimal anymore.

Looking at the level curves in Figs. 5.4 and 5.5, the tracking error $\tilde{p}^c_{\mathrm{peak}}$ grows faster for variations of λ towards region C.C. than towards region I. So, we may be interested in maintaining our feedback gain $\boldsymbol{K}$ in region I for any value of ω. Choosing $\lambda = \omega_{min}^{-1}$ and k^{-1} within the limits of the region (5.25) and (3.52):

$$\frac{\omega_{max}}{\omega_{min}}\sinh(\omega_{max}\tau) + 1 - \cosh(\omega_{max}\tau) \leq k^{-1} < 1, \tag{5.72}$$

Our feedback gain $\boldsymbol{K}$ can be maintained in region I for variations such that

$$\frac{\omega_{min}}{\omega_{max}} > \tanh(\omega_{max}\tau). \tag{5.73}$$

As an example, the largest variation presented in [Brasseur 2015], between $\omega_{min} = 3.37\ \mathrm{s}^{-1}$ and $\omega_{max} = 3.5\ \mathrm{s}^{-1}$ satisfies this condition

$$\frac{\omega_{min}}{\omega_{max}} = 0.96 > 0.018 = \tanh(\omega_{max}\tau), \tag{5.74}$$

using an standard sampling period $\tau = 5$ ms.

Within region I, the cCoP tracking error bound $\tilde{p}^c_{\text{peak}}$ (5.35) is linearly related to λ reaching its minimum value on the lower bound of the region $\lambda = \omega^{-1}$. Using an arbitrary gain $\lambda = \omega^{-1}_{min}$ in region I, the optimal gain k^* can be obtained as before in (5.53):

$$k^* = 1 + \sqrt{\frac{\hat{a} + \hat{n} + \hat{c} + \omega^{-1}_{min}\hat{\dot{c}}}{2(\hat{c} + \lambda\hat{\dot{c}})}}, \tag{5.75}$$

that produces the minimum tracking error bound:

$$\tilde{p}^{c*}_{\text{peak}} = \left(\sqrt{\hat{c} + \omega^{-1}_{min}\hat{\dot{c}}} + \sqrt{2(\hat{a} + \hat{n} + \hat{c} + \omega^{-1}_{min}\hat{\dot{c}})}\right)^2. \tag{5.76}$$

5.4 Simulations and Experiments

Let's evaluate the tracking error dynamics with long sampling periods τ in experiments and simulations with the humanoid robot Toro[1], controlled as follows:

CoM Controller: We use the DCM-based linear feedback (5.47), with feedback gain $\lambda = \omega^{-1}$ and $k = 2$ (used in the example of Fig. 5.6), and several sampling periods τ, specified in each case. For the particular case of the robot Toro, $\omega = 3.21$ s^{-1}.

Whole-Body Controller: Joint positions and contact forces are controlled with an inverse dynamics scheme based on a standard Quadratic Program (QP) [Englsberger 2018]. In this scheme, uncertainties $\hat{u}$ and non-linearities $\boldsymbol{n}$ are partially compensated using arm movements to introduce variations of the angular momentum $\dot{\boldsymbol{L}}$. The sampling period of this QP-based WBC is kept constant at 3 ms, unrelated to the CoM sampling period τ used in (5.47).

Uncertainty Sources: The control law (5.47) generates piece-wise constant values of the input p^c according to (3.21) but, the reference motion has been generated considering a continuous variation of p^c_{ref}, this introduces a numerical error during the double support stages (when both feet are on the ground) that can be observed in Figs. 5.7 and 5.8. An estimation error is also introduced in the CP-feedback (5.47). And in the experiments we have, moreover, mechanical $\hat{a}$ and model $\hat{n}$ errors (3.36).

We can observe in Fig. 5.7 that, in experiments with Toro, the lateral DCM and cCoP tracking performances are similar and satisfactory when $\tau = 51$ ms or 120 ms, as expected from our theoretical analysis. For longer sampling periods, the WBC generates larger arm motions in order to compensate for the growing numerical error and other non-linearities, which ends up triggering an emergency stop due to the increased risk of collision, (see Fig 5.9).

The resulting failure originates in the QP-based WBC and not the DCM linear feedback (5.47), so this doesn't contradict the proposed theoretical analysis. In simulations, this safety system is not triggered and we can observe in Fig. 5.8 that the tracking performance is maintained at a satisfactory level for sampling periods up to $\tau = 216$ ms while degrading sharply afterwards, validating strikingly well the theoretical analysis proposed earlier.

[1]Simulations and experiments in this section were provided courtesy of Johannes Englsberger at the DLR for the article [Villa 2019].

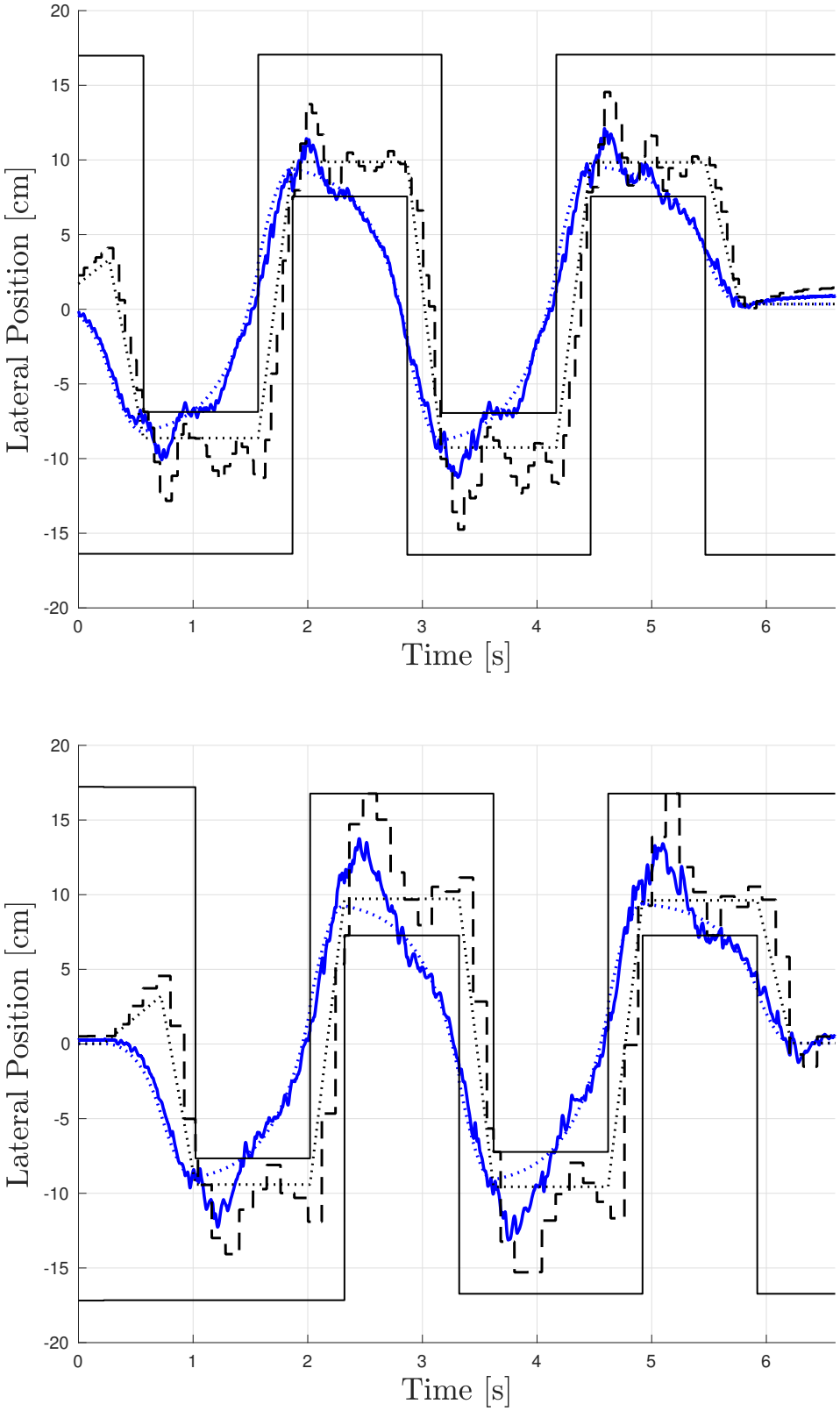

Figure 5.7: Long sampling period experiments. Lateral component of walking **experiments** with the humanoid robot Toro using a feedback gain $k = 2$ and sampling period $\tau = 51$ ms (up) or $\tau = 120$ ms (down). The DCM ξ is represented in blue, while the cCoP is in dashed black. The reference values ξ_{ref} and p_{ref} are indicated with dotted lines.

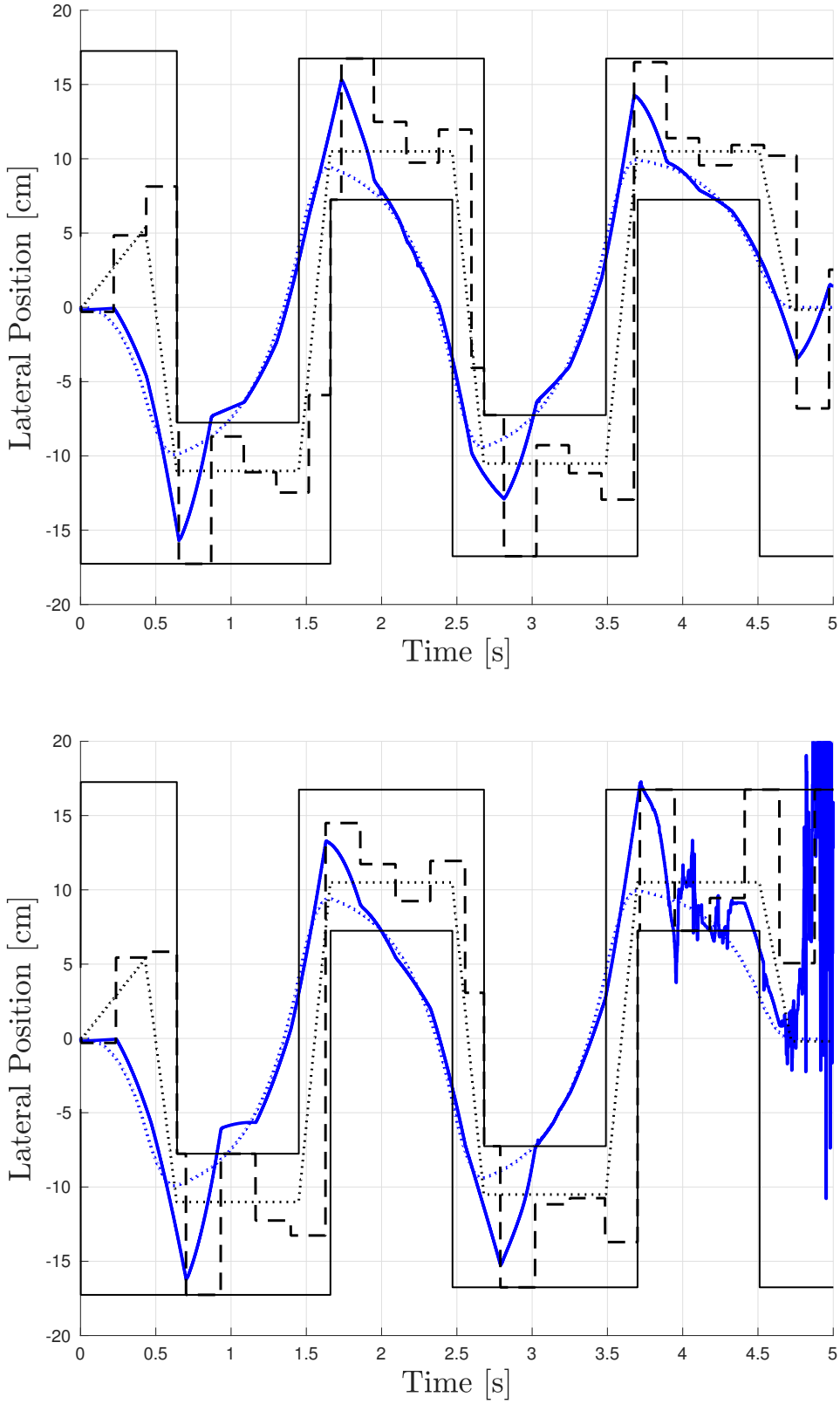

Figure 5.8: Long sampling period simulations. Lateral component of walking **simulations** with the humanoid robot Toro using a feedback gain $k = 2$ and sampling periods $\tau = 216$ ms (up) or $\tau = 232$ ms (down). The DCM ξ is represented in blue, while the cCoP is in dashed black. The reference values ξ_{ref} and p_{ref} are indicated with dotted lines. The numerical error results from the different functional form between black dotted and dashed curves during double support stages.

Figure 5.9: Emergency stop. Robot Toro triggering an emergency stop when the minimum allowed distance between arm and leg is reached.

5.4.1 Restrictiveness and Future Work

We can observe in Figs. 5.7 and 5.8, that the cCoP tracking error $\tilde{p}^c$ (difference between dotted and dashed black curves) grows, in average, with the sampling period τ. We show this in Fig. 5.10, indicating for each fraction of the tracking error bound $\tilde{p}^c_{\text{peak}}$, the percentage of the experiment (or simulation) time during which the tracking error $\tilde{p}^c$ has been maintained below. As an example, in the experiment using $\tau = 100$ ms, the tracking error $\tilde{p}^c$ was maintained below 20% of the bound $\tilde{p}^c_{\text{peak}}$ during 83% of the experiment time. We can observe that using longer sampling periods, higher tracking errors are reached more often, always respecting the upper bound $\tilde{p}_{\text{peak}}$. This bound is, however, independent of the sampling period τ when using feedback gains in regions I and II, as discussed in Sec. 5.3.3.

During the robot motion, disturbances normally do not follow the WCS, resulting in cCoP tracking errors $\tilde{p}^c$ that are, most of the time, smaller than the bound $\tilde{p}^c_{\text{peak}}$ as shown in Fig. 5.10. In order to guarantee a safe robot operation, the control system must be able to handle the maximum tracking error $\tilde{p}^c_{\text{peak}}$ since it could be reached with the WCS of disturbances. This implies restricting the reference constraints (4.70), (4.71) for the worst case. Since it is over-restricting most of the time, we still can improve the management of uncertainty while maintaining safety guarantees. As a future work, we consider:

- Introducing a saturation in the feedback term of (3.33) $\tilde{u}$, below the maximum value required $\tilde{u}_{\text{peak}}$, part of the disturbance may be postponed (evolving in open loop) up to a time in the future when the control $\tilde{u}$ is not saturated. This strategy can be complemented including a feedback term in the step placement, as usual in robots with point feet [Kim 2016], and using the larger support polygon $\mathcal{P}$ of the double support stages to compensate for bigger (or postponed) disturbances.

- Using a disturbance observer as the one presented in [Smaldone 2019], we can recognize early a WCS of disturbances to change the feedback gain $\boldsymbol{K}$ into a region with a different worst-case behavior, in the map of Figs. 5.1, 5.2, in order to avoid tracking error peaks.

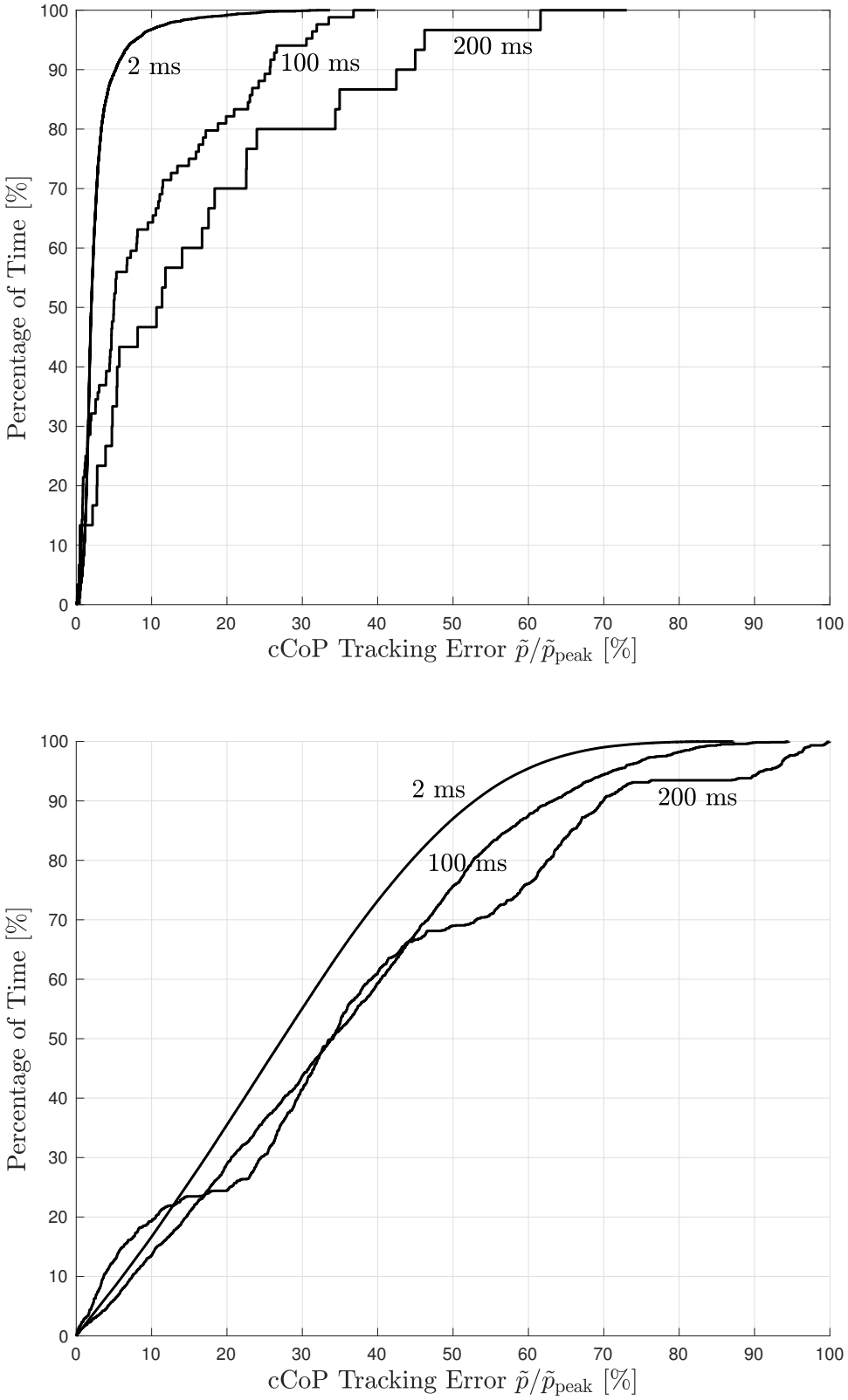

Figure 5.10: Cumulated time of each tracking error size. We show the portion of time during which the cCoP tracking errors $\tilde{p}^c$ is smaller than each given fraction of the bound value $\tilde{p}^c_{\text{peak}}$. This tracking error timing is shown for whole-body experiments ($\tau = 2$ and 100 ms) and simulation ($\tau = 200$ ms) (up); and for CoM simulations with disturbances such that $\hat{u} = \pm\hat{u}_{\text{peak}}$ where the sign $\pm$ is randomly decided every 50 ms (down). In all cases $k = 2$.

5.5 Compliant Ground Interaction

When the ground is not rigid, the dynamics of interaction with the ground produces a slower control of forces, and therefore of the CoP. We have a similar dynamics in position controlled robots, which typically rely on the deflection of a spring in the ankle to measure and exert ground contact forces. For these cases, we cannot neglect the dynamics of contact forces (3.4) [Kajita 2010]. In this section, we study how to minimize the effect from uncertainty sources on the cCoP tracking error using the system $\mathrm{P}_d{\to}\mathrm{XP}$ and the humanoid robot HRP-4 ($\omega \approx 3.54$) developed by Kawada Industries. However, once again, most part of the discussion applies to legged robots in general.

5.5.1 Tracking Error and Gain Regions

We show in Fig. 5.11 the ratio r (5.31) for every stable feedback gain $\boldsymbol{K}$ with soft ($\gamma = 2\omega$) and stiff ($\gamma = 40\omega$) ground interaction. It is minimum when both poles are zero $q_1 = q_2 = 0$, and grows towards the stability limits.

Including all sources of uncertainty (3.36), the cCoP tracking error bound (5.31) is

$$\tilde{p}^c_{\text{peak}} = r\left(\hat{a}_{\text{peak}} + \hat{n}_{\text{peak}} + \frac{\hat{\dot{n}}_{\text{peak}}}{\gamma}\right) + rk\hat{\xi}_{\text{peak}} + rk\lambda\hat{p}^c_{\text{peak}}. \tag{5.77}$$

From this expression we can expect the minimum tracking error to be reached with smaller gains k and λ than the minimum ratio r, depending on the proportion between uncertainties. We show in Fig. 5.12 level curves of the cCoP tracking error for stable gains with equivalent magnitudes for each uncertainty source:

$$\hat{a}_{\text{peak}} + \hat{n}_{\text{peak}} + \frac{\hat{\dot{n}}_{\text{peak}}}{\gamma} = \hat{\xi}_{\text{peak}} = \hat{p}^c_{\text{peak}}. \tag{5.78}$$

Soft ground interactions (small γ) reach the minimum bound $\tilde{p}^{c*}_{\text{peak}}$ in region C.C. where the closed-loop poles have complex-conjugate values. Hence, the ratio r must be computed numerically from the outer approximation proposed in Sec. 4.4.2. Stiffer ground interactions (high γ) reach the minimum bound $\tilde{p}^{c*}_{\text{peak}}$ in the region IV with real-valued poles and the ratio r is obtained from (4.34).

5.5.2 Optimal Gains

In the limit of rigid ground interaction ($\gamma \to \infty$), the control system $\mathrm{P}_d{\to}\mathrm{XP}$ (3.31)

$$\begin{bmatrix} \xi^+ \\ p^{c+} \end{bmatrix} = \begin{bmatrix} \mathrm{e}^{\omega\tau} & 0 \\ 0 & 0 \end{bmatrix} \begin{bmatrix} \xi \\ p^c \end{bmatrix} + \begin{bmatrix} 1 - \mathrm{e}^{\omega\tau} \\ 1 \end{bmatrix} p^c_{des} \tag{5.79}$$

is decoupled in a system of the form $\mathrm{P}{\to}\mathrm{X}$ (3.29) in the first row, and an instantaneous cCoP control in the second row:

$$p^{c+} = p^c_{des}. \tag{5.80}$$

In such case, moreover, the line of gains for a null pole $q_1 q_2 = 0$ (5.29) satisfies:

$$\begin{aligned} \lambda &= \lim_{\gamma\to\infty} \left(\frac{1 - k^{-1}}{\mathrm{e}^{\gamma\tau} - 1} - \frac{\gamma \mathrm{e}^{-\omega\tau} + \omega \mathrm{e}^{\gamma\tau}}{(\gamma + \omega)(\mathrm{e}^{\gamma\tau} - 1)} \right) \\ &= \lim_{\gamma\to\infty} -\left(\frac{\mathrm{e}^{-\omega\tau}}{(1 + \frac{\omega}{\gamma})(\mathrm{e}^{\gamma\tau} - 1)} + \frac{\omega}{(\gamma + \omega)(1 - \mathrm{e}^{-\gamma\tau})} \right) \\ &= 0, \end{aligned} \tag{5.81}$$

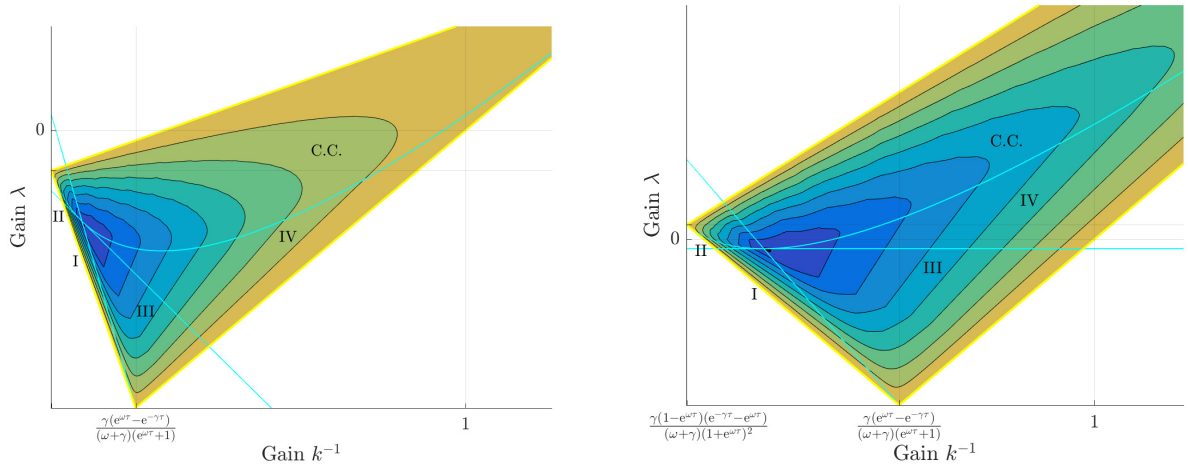

Figure 5.11: Level curves of the ratio r. We show soft $\gamma = 2\omega$ (left) and stiff $\gamma = 40\omega$ (right) ground interactions. In both cases the sampling period is $\tau = 87$ ms. The level is minimum in black and grows towards the stability limits in yellow. We also overlay the map of regions discussed earlier.

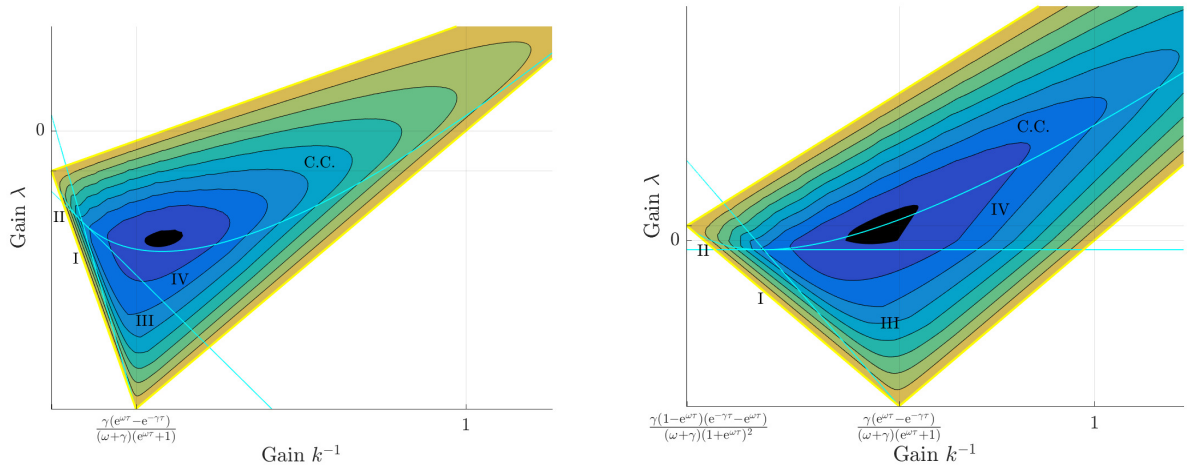

Figure 5.12: Level curves of the cCoP tracking error bound $\tilde{p}^c_{\text{peak}}$. We show soft $\gamma = 2\omega$ (left) and stiff $\gamma = 40\omega$ (right) ground contact. In both cases the sampling period is $\tau = 87$ ms. The level is minimum in black and grows towards the stability limits in yellow. We also overlay the map of regions discussed earlier.

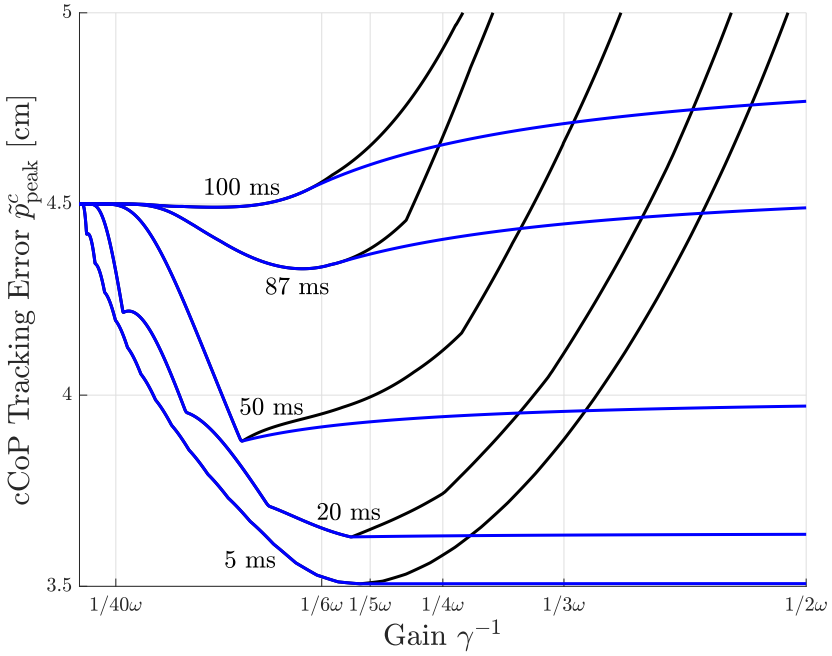

Figure 5.13: Relation between cCoP tracking error bound, compliance and sampling period. The minimum cCoP tracking error bound $\tilde{p}^{c*}_{\text{peak}}$ obtained numerically with uncertainty sources of up to 0.5 cm and sampling periods $\tau = 5$, 20, 50, 87 and 100 ms. Black curves corresponds to DCM-feedback law and blue curves show the case of complete state feedback.

so that both r and $rk\lambda$ have minimum values with $\lambda = 0$. Using this gain, the control law (3.33) is

$$p^c = p^c_{ref} + k\tilde{\xi} + \hat{u}, \tag{5.82}$$

that is equivalent to (5.47). So, all results of the Sec. 5.3.2 follows.

When γ has finite values, we consider both the DCM-feedback law (using $\lambda = 0$) (5.81) and the complete state feedback law (3.33) to generate the Fig. 5.13. Considering standard uncertainty amplitudes [Flayols 2017], [Benallegue 2015]:

$$\hat{a}_{\text{peak}} + \hat{n}_{\text{peak}} + \frac{\hat{\dot{n}}_{\text{peak}}}{\gamma} = \hat{\xi}_{\text{peak}} = \hat{p}^c_{\text{peak}} = 0.5 \text{ cm}, \tag{5.83}$$

in this figure, optimal feedback gains are obtained numerically to minimize the cCoP tracking error bound (5.77), which is shown as a function of the interaction compliance γ^{-1} for several sampling periods.

We can observe that the DCM-feedback law is close to optimal for hard ground interactions ($\gamma^{-1} < \frac{1}{5\omega}$) and degrades sharply when the interaction is softer.

We can also see that some degree of compliance in the ground interaction slightly reduces the size of the minimum cCoP tracking error $\tilde{p}^{c*}_{\text{peak}}$ with respect to the rigid case, from 4.5 cm down to 3.5 cm when

$$0 < \gamma^{-1} \leq \frac{1}{2\omega}, \qquad 0 < \tau \leq 87 \text{ ms}, \tag{5.84}$$

which contains most practical uses. For example, [Kajita 2010, Morisawa 2012] use $\gamma^{-1} = \frac{1}{5.6\omega}$ with $\tau = 5$ ms and [Caron 2019] uses $\gamma^{-1} = \frac{1}{2\omega}$ with $\tau = 5$ ms.

5.6 Discussion and Conclusions

Thanks to the conditions for a safe operation introduced in Ch. 4, we can safely manage uncertainties up to a maximum set $\mathcal{V}_{max}$ by restricting the robot motion for the worst case of maximum tracking error. We propose to minimize the tracking error bound $\tilde{p}^{c}_{\text{peak}}$ by an appropriate choice of feedback gain $\boldsymbol{K}$. Thus, we can generate less restricted motions or handle bigger uncertainties coming from, for example, cheaper sensors and actuators, while maintaining our safety guarantees.

When the ground interaction is rigid, the minimum tracking error bound $\tilde{p}^{c*}_{\text{peak}}$ (5.52) is obtained using the feedback gains $\boldsymbol{K}^*$ reported in (5.53). Feedback gains in the region I of Fig. 5.1, such as $\boldsymbol{K}^*$, produce tracking error bounds that are independent of the sampling period τ. For standard uncertainties $\hat{a}$, $\hat{n}$, $\hat{\boldsymbol{x}}$, we can use sampling periods as long as $\tau \approx 200$ ms with literally no impact on the tracking error bound $\tilde{p}^{c*}_{\text{peak}}$ and, therefore, on the guarantee that balance can be maintained safely. This provides some degree of freedom in the choice of sampling period, which could be used to avoid exciting structural vibration modes [Englsberger 2018] or to save energy computing less often the control law (3.33), since the CPU consumption has been observed to be a significant fraction of the whole power consumption of the robot Toro [Henze 2019].

When the ground interaction is compliant, the optimal feedback gain $\boldsymbol{K}^*$ can be obtained by minimizing numerically the tracking error bound (5.77). We have observed that the minimum tracking error bound $\tilde{p}^{c*}_{\text{peak}}$ is bounded by the rigid case for most standard compliance γ, sampling periods τ and uncertainties $\hat{a}$, $\hat{n}$, $\hat{\boldsymbol{x}}$.

In order to perform the analysis proposed in this chapter, we have developed maps of worst-case behavior of disturbances to identify the appropriate computation of the ratio r (5.31) from Sec. 4.4 and main characteristics of the tracking error obtained from a given feedback gain.

Chapter 6

Reference Motion Generation

6.1 Introduction

The reference motion is designed as a feasible trajectory for the robot to achieve some goal. It must satisfy the system dynamics (3.38) and tighter constraints (4.70), (4.71), to account for uncertainties. Considering the particular case of biped robots, we generate the reference motion based on the set of variables presented in Sec. 6.2. In order to compute it online considering its hard constraints, we use the method of Model Predictive Control MPC, that is briefly described in Sec. 6.3. Our implementation is detailed in Secs. 6.4, 6.3.2 and 6.3.3. We discuss, in Sec. 6.3.4 an initial constraint to feedback the current state of the robot in the motion generation scheme, which closes the dashed connection of Fig. 3.1. We compare in simulations the resulting "closed-loop" controller with the standard "open loop" implementation.

6.2 Walking Motion Configuration

Iterating with the dynamics (3.38), the reference trajectory $\boldsymbol{X}_{ref}$ with initial state $\boldsymbol{x}_{ref\cdot 0}$, is the sequence of states

$$\begin{bmatrix} \boldsymbol{x}_{ref\cdot 1} \\ \boldsymbol{x}_{ref\cdot 2} \\ \vdots \\ \boldsymbol{x}_{ref\cdot i} \\ \vdots \end{bmatrix} = \begin{bmatrix} \boldsymbol{A} \\ \boldsymbol{A}^2 \\ \vdots \\ \boldsymbol{A}^i \\ \vdots \end{bmatrix} \boldsymbol{x}_{ref\cdot 0} + \begin{bmatrix} \boldsymbol{B} & & & \boldsymbol{0} & \boldsymbol{0} & \boldsymbol{0} \\ \boldsymbol{AB} & \boldsymbol{B} & & & \boldsymbol{0} & \boldsymbol{0} \\ \vdots & & & \ddots & & \boldsymbol{0} \\ \boldsymbol{A}^{i\text{-}1}\boldsymbol{B} & \boldsymbol{A}^{i\text{-}2}\boldsymbol{B} & \cdots & \boldsymbol{B} & & \\ \vdots & & & & & \ddots \end{bmatrix} \begin{bmatrix} u_{ref\cdot 0} \\ u_{ref\cdot 1} \\ \vdots \\ u_{ref\cdot i} \\ \vdots \end{bmatrix}, \tag{6.1}$$

when a reference sequence of control actions $\boldsymbol{U}_{ref}$ is executed.

At every time instant, the robot motion $\boldsymbol{x}$, u must satisfy the physical constraints (2.26), (3.14), (2.27) reproduced here:

$$s \in \mathcal{S}(s_k) \tag{6.2}$$

$$p^c \in \mathcal{P}(s_k) - n \tag{6.3}$$

$$c \in \mathcal{C}(s_k). \tag{6.4}$$

Assuming rectangular sets as shown in Figs.6.1, 6.2, 6.3, the reference motion is constrained in the simple form (4.71), (4.70):

$$\underline{\Delta s} \leq \Delta s \leq \overline{\Delta s}, \tag{6.5}$$

$$\underline{\Delta p^c} + \tilde{p}^c_{\text{peak}} \leq \Delta p^c_{ref} \leq \overline{\Delta p^c} - \tilde{p}^c_{\text{peak}}, \tag{6.6}$$

$$\underline{\Delta c} + \tilde{c}_{\text{peak}} \leq \Delta c_{ref} \leq \overline{\Delta c} - \tilde{c}_{\text{peak}}, \tag{6.7}$$

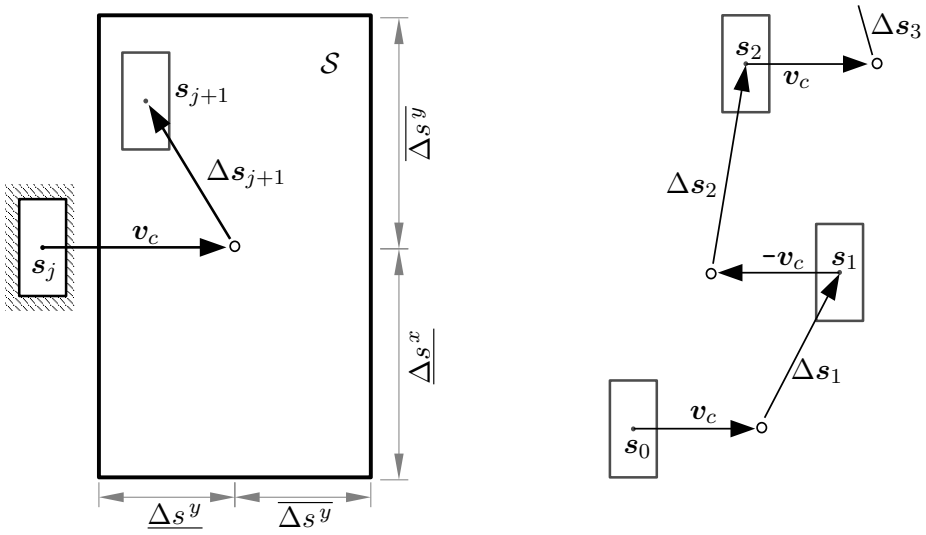

Figure 6.1: Stepping Area. On the left, we show the restriction in the placement of new steps, that we approximate with a rectangular region $\mathcal{S}$ on the ground. On the right, we present the first two steps of the summation (6.8).

where Δs, Δp and Δc are the CoF, CoP and CoM measured from the center of each respective constraint set with lower and upper limits indicated. Introducing these relative measures, during the j-th step, the global variables can be written as:

$$s_j \equiv s_0 + \sum_{b=1}^{j} \Big((\text{-}1)^b v_c + \Delta s_b \Big), \tag{6.8}$$

$$p^c \equiv s_j + \Delta p^c_{ref} + \tilde{p}^c, \tag{6.9}$$

$$c \equiv s_j + \Delta c_{ref} + \tilde{c}, \tag{6.10}$$

where constant vector v_c indicates the center of the next stepping area $\mathcal{S}$ measured from the center of the landed foot at each instant.

We need a sequence of control actions $u_{ref\cdot i}$ such that the resulting reference motion (6.1) satisfies the constraints (6.5), (6.6), (6.7). A trajectory predefined off-line can be used as done in [Choi 2006], or in [Song 2015] where a handcrafted trajectory is adapted to satisfy the walking constraints. For the on-line generation of the trajectory considering hard constraints, Model Predictive Control (MPC) is one of few suitable methods [Mayne 2000] and, therefore, has been used extensively for the control of legged robots. This allows generating walking motions online with automatic footstep placement [Herdt 2010], taking into account visual feedback [Dune 2011], avoiding collisions in a crowd [Bohórquez 2016], undertaking physical collaborations with humans [Agravante 2016], *etc.*

6.3 Model Predictive Control

At each time instant i, MPC generates the reference control action $u_{ref\cdot i}$ to be executed during the next time-step of duration T. This method takes into account a finite preview horizon of N time-steps starting at the current time i to generate an optimal control action $u_{ref\cdot i}$ following the steps [Fernandez-Camacho 1995]:

1 - A cost function is generated, based on the robot model and the initial state $\boldsymbol{x}_{ref\cdot i}$, having its minimum value in some aimed motion $\boldsymbol{x}_{aim\cdot(h|i)}$, $u_{aim\cdot(h|i)}$, where we use i to

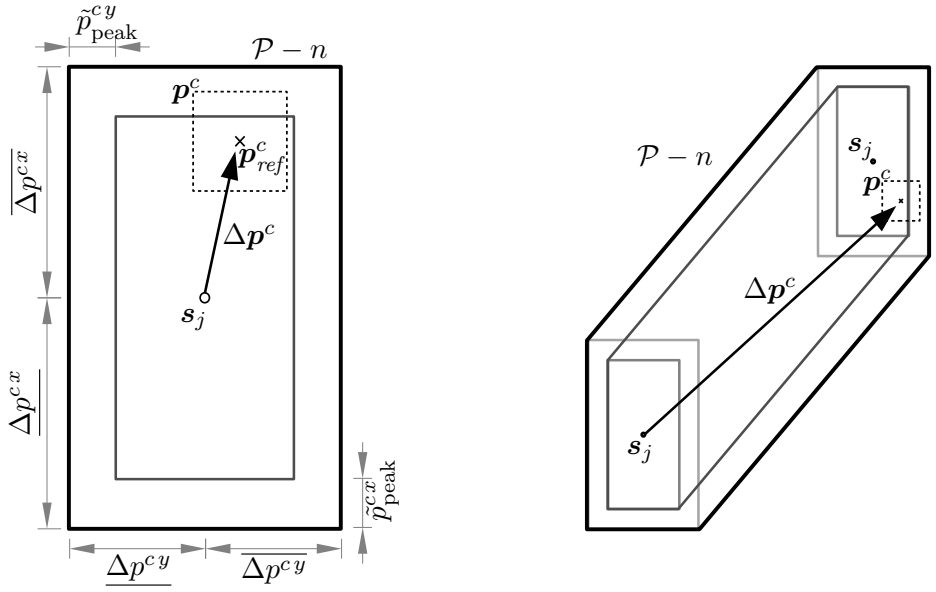

Figure 6.2: Support polygon. Assuming bounded disturbances, the cCoP $\boldsymbol{p}^c$ is bound to the region in dashed lines, which is always contained in the support polygon $\mathcal{P}-n$ (external rectangle) if we constrain the reference cCoP $\boldsymbol{p}^c_{ref}$ to the internal rectangle. The support polygon changes shape during the double support stage. Nevertheless, sampling the system right before and right after the change of supporting foot, we can implement the restrictions for the single support only. For this, we match the periods of discretization and double support ($T = 100$ ms) in the reference generation.

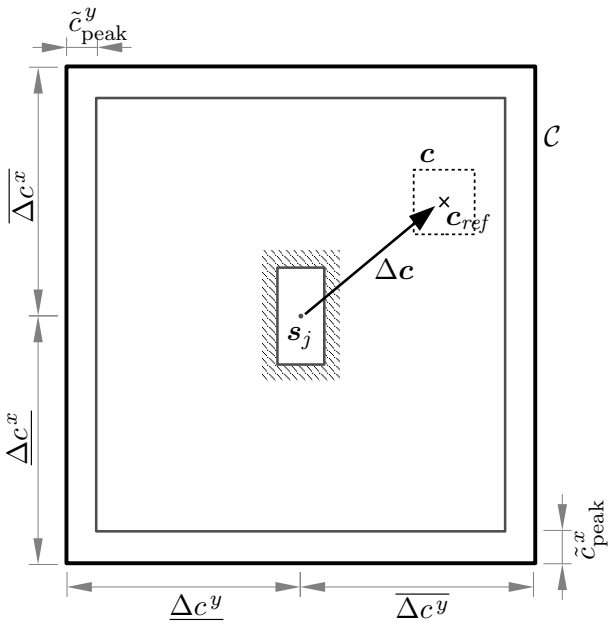

Figure 6.3: Kinematic Constraint. Leg lengths restrict the CoM $\boldsymbol{c}$ to lie in a region $\mathcal{C}$ around the landed foot $\boldsymbol{s}_j$, that we approximate with a square. We satisfy this limitation, with bounded uncertainties, by restricting the reference CoM $\boldsymbol{c}_{ref}$ to the internal square.

$t = i + h$	$t > t_{j+1}$	$\cdots$ $t > t_{j+2}$ $\cdots$	$t > t_{j+M}$
$i + 0$	0	0	0
$i + 1$	0	0	0
$\vdots$	**0**	$\cdots$ **0** $\cdots$	**0**
$t_{j+1} + 1$	1	0	0
$\vdots$	**1**	$\cdots$ $\vdots$ $\cdots$	**0**
$t_{j+M} + 1$	1	1	1
$\vdots$	**1**	$\cdots$ **1** $\cdots$	**1**
$i + N$	1	1	1

Table 6.1: The landed foot at each preview time h is determined from the condition associated to its corresponding column. As a result, we obtain the matrix $\boldsymbol{E}_i$.

$$\boldsymbol{E}_i = \begin{bmatrix} 0 & & 0 & 0 \\ & & & 0 \\ 1 & & & \vdots \\ \vdots & & & \\ & 1 & & \\ & \vdots & & \\ & & 1 & \\ & & \vdots & \\ 1 & 1 & 1 & 1 \end{bmatrix} \tag{6.17}$$

index the real time instant when the preview horizon starts, and $h \in \{0, \cdots, N\}$ to index future time instants in the preview horizon.

2 - An optimal sequence of control actions

$$\boldsymbol{U}_{ref \cdot i} \equiv \langle u_{ref \cdot (0|i)}, u_{ref \cdot (1|i)}, \ldots, u_{ref \cdot (N\text{-}1|i)} \rangle, \tag{6.11}$$

according to the system dynamics, is obtained minimizing the cost function within the system constraints (4.70), (4.71).

3 - The resulting control action $u_{ref \cdot i} \equiv u_{ref \cdot (0|i)}$ is executed during one time-step reaching a new state $x_{ref \cdot i+1}$, that is used to initialize the computation of the next control action $u_{ref \cdot i+1} \equiv u_{ref \cdot (0|i+1)}$ (which in principle may be different from $u_{ref \cdot (1|i)}$ because of the new information available).

6.3.1 Predicted Trajectory

Let's consider the relative variables Δs, Δu_{ref} to design the optimization problem required in MPC, where Δu_{ref} is the relative cCoP Δp^c_{ref} or its desired value $\Delta p^c_{des \cdot ref}$ depending on the system. We can write the predicted control sequence as:

$$\boldsymbol{U}_{ref \cdot i} = \boldsymbol{S}_i + \Delta \boldsymbol{U}_{ref \cdot i}, \tag{6.12}$$

where

$$\Delta \boldsymbol{U}_{ref \cdot i} \equiv \langle \Delta u_{ref \cdot (0|i)}, \Delta u_{ref \cdot (1|i)}, \ldots, \Delta u_{ref \cdot (N\text{-}1|i)} \rangle \in \mathbb{R}^N, \tag{6.13}$$

and $\boldsymbol{S}_i$ indicates the landed foot at each time h in the preview horizon, from (6.8) we have:

$$\boldsymbol{S}_i = \boldsymbol{S}_{0 \cdot i} + \boldsymbol{E}_i (\boldsymbol{V}_{c \cdot i} + \Delta \boldsymbol{S}_i) \in \mathbb{R}^N, \tag{6.14}$$

where $\boldsymbol{S}_{0 \cdot i} \in \mathbb{R}^N$ indicates in all its elements the global position $s_{(0|i)}$ of the foot that is landed when the preview horizon starts. The M predicted future steps

$$\boldsymbol{V}_{c \cdot i} \equiv \langle (\text{-}1)^{j(i)+1} v_c, (\text{-}1)^{j(i)+2} v_c, \ldots, (\text{-}1)^{j(i)+M} v_c \rangle \in \mathbb{R}^M, \tag{6.15}$$

$$\Delta \boldsymbol{S}_i \equiv \langle \Delta s_{(1|i)}, \Delta s_{(2|i)}, \ldots, \Delta s_{(M|i)} \rangle \in \mathbb{R}^M, \tag{6.16}$$

with the j-th step landed when the preview horizon starts, are adapted to their respective timing in the preview horizon using the matrix $\boldsymbol{E}_i$, obtained from a logic table as Tab. 6.1. We use predefined times t_j to change the supporting foot as in [Herdt 2010], but in principle, a

different criterion could be used, as for example based on the capturability area [Pratt 2006], or on the CoM potential energy [Imanishi 2018].

Iterating in the reference dynamics (3.38) with this predicted control sequence $\boldsymbol{U}_{ref\cdot i}$ as shown in (6.1), we can obtain the predicted trajectory:

$$\boldsymbol{X}_{ref\cdot i} = \boldsymbol{A}_N \boldsymbol{x}_{ref\cdot(0|i)} + \boldsymbol{B}_N \boldsymbol{U}_{ref\cdot i}, \tag{6.18}$$

where $\boldsymbol{A}_N$ and $\boldsymbol{B}_N$ are the extended matrices shown in (6.1) for N iterations.

We decide the control sequence $\boldsymbol{U}_{ref\cdot i}$ from an optimization problem with a cost function to penalize undesired states and restricted to produce only feasible motions as we describe in the following sections.

6.3.2 Cost Function

We penalize the states $\boldsymbol{x}_{ref\cdot(h|i)}$ and inputs $\Delta u_{ref\cdot(h|i)}$ along the preview horizon based on the distance to the aimed motion $\boldsymbol{x}_{aim\cdot(h|i)}$, $u_{aim\cdot(h|i)}$ using a cost function of the form

$$V_i(\boldsymbol{U}_{ref\cdot i}, \boldsymbol{x}_{ref\cdot(0|i)}) = \sum_{h=1}^{N} \sigma_x \|\boldsymbol{L}\boldsymbol{x}_{ref\cdot(h|i)} - \boldsymbol{L}\boldsymbol{x}_{aim\cdot(h|i)}\|^2 + \sum_{h=0}^{N-1} \sigma_u \|\Delta u_{ref\cdot(h|i)} - \Delta u_{aim\cdot(h|i)}\|^2, \tag{6.19}$$

where σ_x, $\sigma_u \in \mathbb{R}$ are predefined weights and we are keeping the notation introduced in Ch.4 for an arbitrary linear combination of state variables $\boldsymbol{L}\boldsymbol{x}_{ref\cdot(h|i)}$. Later in this chapter we present simulations using the system P→CC̈ where we aim for some desired DCM ξ_{aim} ($\boldsymbol{L} = \begin{bmatrix} 1 & \omega^{-1} \end{bmatrix}$) and for some desired CoM ($\boldsymbol{L} = \begin{bmatrix} 1 & 0 \end{bmatrix}$). Moreover, we normally aim to minimize the control input $\Delta \boldsymbol{U}_{aim} = \boldsymbol{0}$ in order to reduce the effort of motors, maintain p^c_{ref} far from its constraint bounds and produce smooth motions.

6.3.3 Terminal Constraint

At each iteration with MPC, we compute a sequence of N control actions $u_{ref\cdot(h|i)}$, then we only execute the first one $u_{ref\cdot(0|i)}$ and, at the next time-step $(i+1)$, we compute N new actions $u_{ref\cdot(h|i+1)}$. Thanks to this mechanism, we can be sure that feasible control actions $u_{ref\cdot(h|i)}$ could be executed, at least during N time-steps in the future. Feasibility in posterior times (so-called recursive feasibility) can be ensured by introducing a terminal constraint as

$$\boldsymbol{x}_{ref\cdot(N|i)} \in \mathcal{X}_{\text{TER}}, \tag{6.20}$$

to reach at the end of the preview horizon some set of states $\mathcal{X}_{\text{TER}}$ that satisfies all system constraints and where the robot can stay for indefinite time using some feasible control law.

In legged robots, it is normally achieved by imposing that the robot is able to stop at the end of the preview horizon [Sherikov 2014, Ciocca 2017] without execute additional steps. This constraint, called 0-step capturability [Koolen 2012], requires the DCM ξ_{ref} to be reachable (or "capturable") by the cCoP p^c_{ref} within the current support polygon (6.6) to stabilize the dynamics (2.15). In such case, the robot can stay standing with some simple control law.

When using terminal constraints, MPC restricts the robot motion to always keep the terminal set reachable at the end of the preview horizon. This restrictiveness can be reduced using longer preview horizons or bigger terminal sets $\mathcal{X}_{\text{TER}}$. Sticking to the objectives of this thesis, we propose, for each system, stopping terminal sets that reduce the motion restrictiveness while ensuring feasibility:

P→X

The set of states $\mathcal{X}_{\text{TER}}$ defined by physical and capturability constraints:

$$\underline{\Delta p^c} + \tilde{p}^c_{\text{peak}} < \Delta\xi_{ref} < \overline{\Delta p^c} - \tilde{p}^c_{\text{peak}}, \tag{6.21}$$

is a control positively invariant set as shown in the App. D. Therefore, we can ensure the long term feasibility of the motion generated using this set as terminal constraint.

P→CĊ

The set of states $\mathcal{X}_{\text{TER}}$ defined by physical and capturability constraints:

$$\underline{\Delta p^c} + \tilde{p}^c_{\text{peak}} < \Delta\xi_{ref} < \overline{\Delta p^c} - \tilde{p}^c_{\text{peak}}, \qquad \underline{\Delta c} + \tilde{c}_{\text{peak}} \leq \Delta c_{ref} \leq \overline{\Delta c} - \tilde{c}_{\text{peak}}, \tag{6.22}$$

is a control positively invariant set as shown in the App. D. Therefore, we can ensure the long term feasibility of the motion generated using this set, shown in Fig. 6.4, as terminal constraint.

$\mathbf{P}_d$→XP

The set of states $\mathcal{X}_{\text{TER}}$ defined by physical and capturability constraints:

$$\begin{aligned} &\underline{\Delta p^c} + \tilde{p}^c_{\text{peak}} \leq \Delta p^c_{ref} \leq \overline{\Delta p^c} - \tilde{p}^c_{\text{peak}}, \\ &\underline{\Delta p^c} + \tilde{p}^c_{\text{peak}} \leq \left(1 + \frac{\omega}{\gamma}\right)\Delta\xi_{ref} - \frac{\omega}{\gamma}\Delta p^c_{ref} \leq \overline{\Delta p^c} - \tilde{p}^c_{\text{peak}}, \end{aligned} \tag{6.23}$$

is a control positively invariant set as shown in the App. D. Therefore, we can ensure the long term feasibility of the motion generated using this set, shown in Fig. 6.5, as terminal constraint.

Alternatively, terminal constraints to ensure that the robot can continue walking after the horizon have been proposed in [Scianca 2019]. However, in a dynamic environment, the capability to perform emergency stops may be necessary for safety [Bohórquez 2016].

6.3.4 Initial Constraint

At each iteration, the MPC scheme generates a new trajectory along the preview horizon. Usually, this trajectory is initialized from the optimal state

$$\boldsymbol{x}_{ref\cdot(0|i)} = \boldsymbol{x}_{ref\cdot(1|i\text{-}1)} \tag{6.24}$$

obtained from the previous iteration i-1, regardless of the current state of the robot [Feng 2015]. In this case, as discussed in Sec. 4.2, once the current state is within a RPI set around the reference trajectory (4.7)

$$\boldsymbol{x}_{(0|i)} \in \boldsymbol{x}_{ref\cdot(0|i)} + \mathcal{Z}, \tag{6.25}$$

it stays bounded around the reference ensuring robust recursive feasibility for any disturbance $\hat{u} \in \mathcal{V}$ thanks to the robust positively invariance of the set $\mathcal{Z}$ [Langson 2004, prop. 2]. In this approach, however, we cannot ensure feasibility before the tracking error $\tilde{\boldsymbol{x}} = \boldsymbol{x}_{(0|i)} - \boldsymbol{x}_{ref\cdot(0|i)}$ reaches the set $\mathcal{Z}$. We call Open Loop MPC (OL-MPC) this initialization since it does not incorporate information from the current state of the robot.

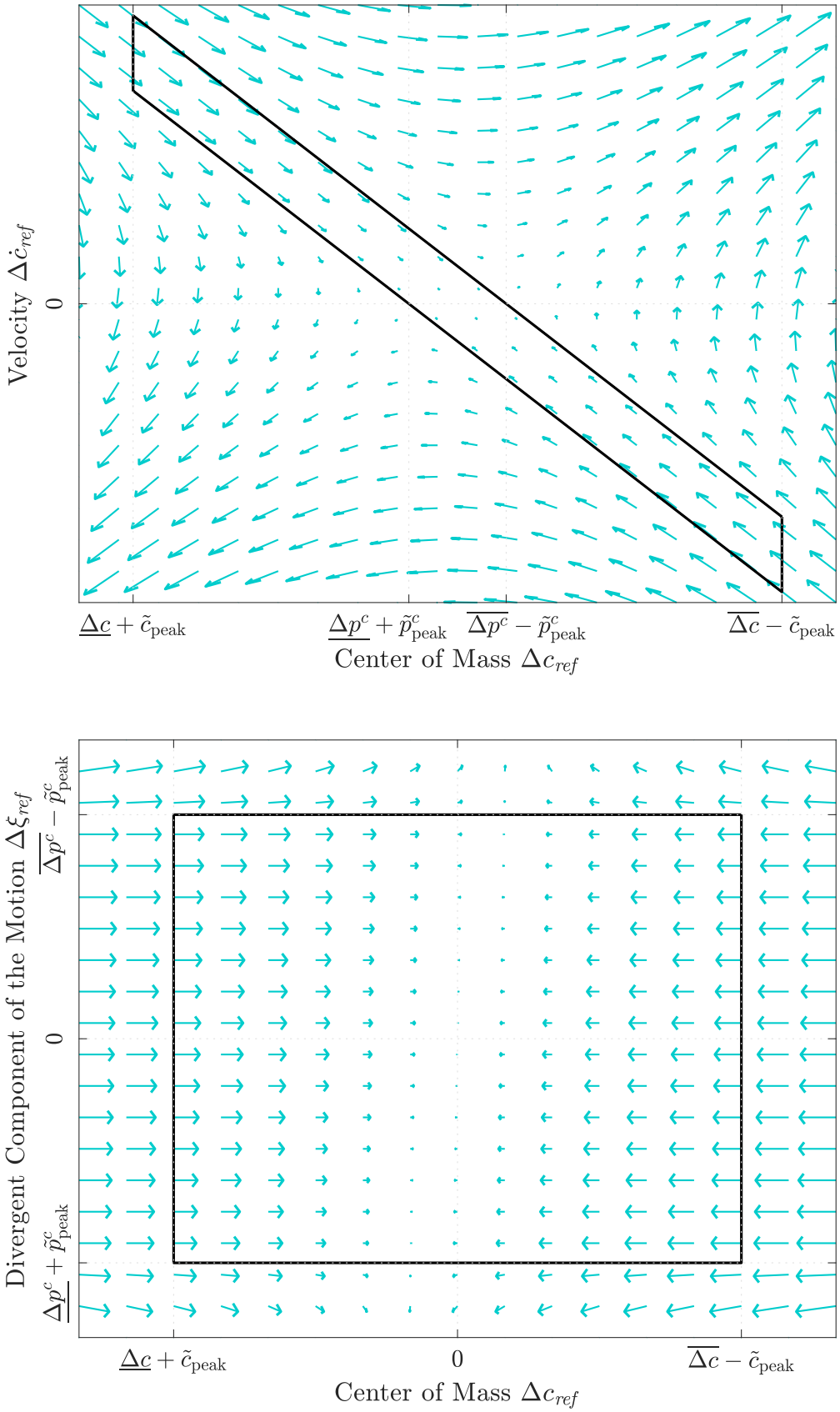

Figure 6.4: Terminal constraint of P→CĊ. We show the terminal set obtained in App. D for the system P→CĊ represented in the state space with variables Δc_{ref}, $\Delta\dot{c}_{ref}$ and Δc_{ref}, $\Delta\xi_{ref}$. Using the proposed feedback law (D.6), the closed-loop system evolves from each state as indicated with blue arrows $\boldsymbol{x}^+_{ref} - \boldsymbol{x}_{ref}$.

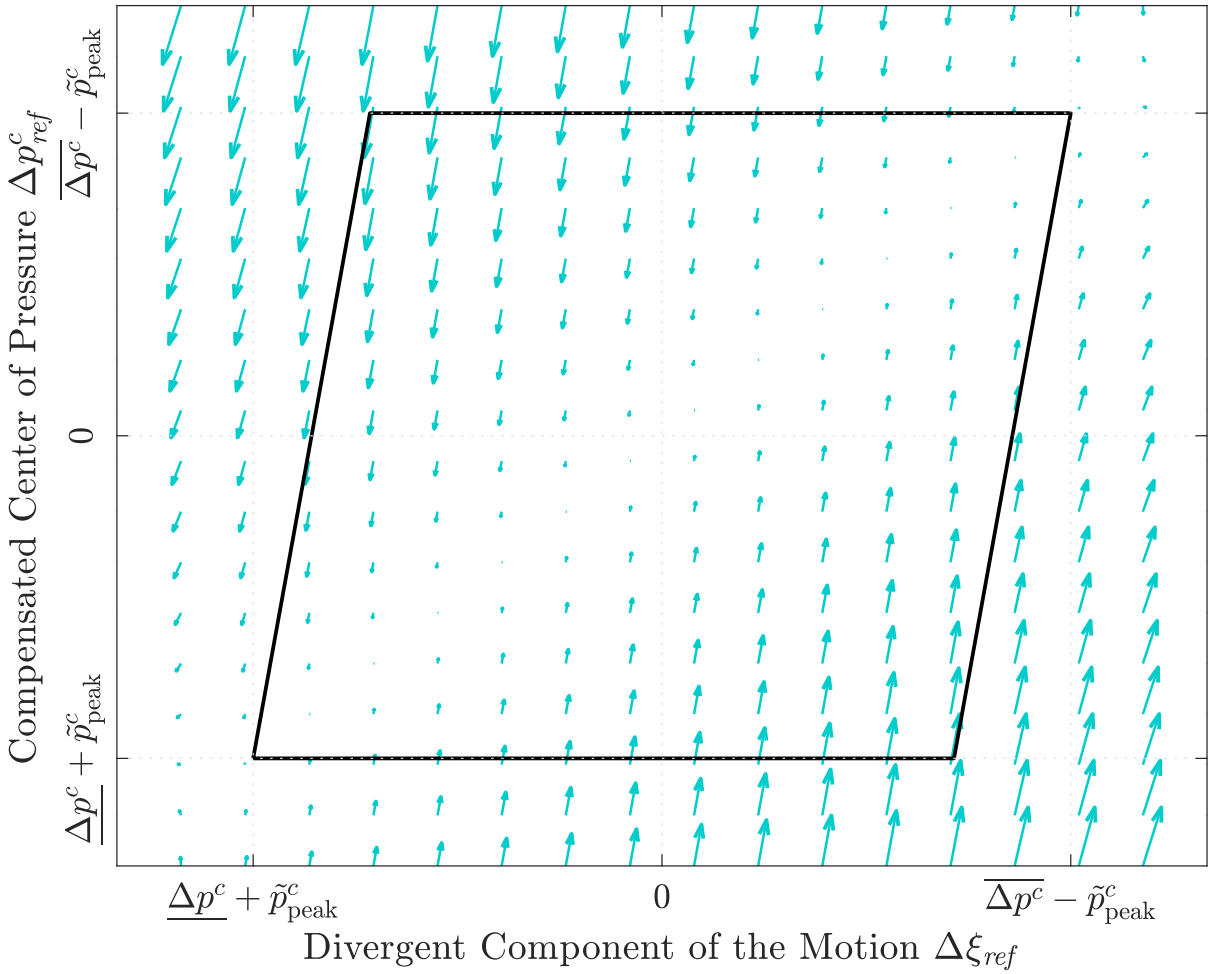

Figure 6.5: Terminal constraint of $\mathrm{P}_d \to \mathrm{XP}$. We show the terminal set obtained in App. D for the system $\mathrm{P}_d \to \mathrm{XP}$ represented in the state space with variables $\Delta\xi_{ref}$, Δp^c_{ref}. Using the proposed feedback law (D.7), the closed-loop system evolves from each state as indicated with blue arrows $\boldsymbol{x}^+_{ref} - \boldsymbol{x}_{ref}$.

In order to ensure the condition (6.25) from the beginning of the motion, we could initialize the trajectory directly from the current state

$$\boldsymbol{x}_{ref\cdot(0|i)} = \boldsymbol{x}_{(0|i)}, \tag{6.26}$$

which is also a common approach [Wieber 2006b], but since the current state may not satisfy the reference constraints, the controller can become infeasible even with a small disturbance. We call Direct Closed-Loop MPC (DCL-MPC) this initialization.

In the approach proposed in [Mayne 2005], the initial state $\boldsymbol{x}_{ref\cdot(0|i)}$ is optimally chosen to satisfy the reference constraint (4.70), taking into account the current state to accomplish the condition (6.25) at every iteration with the initial constraint

$$\boldsymbol{x}_{ref\cdot(0|i)} \in \boldsymbol{x}_{(0|i)} - \mathcal{Z}. \tag{6.27}$$

This way, even after an unexpected strong perturbation that pushes the tracking error away from $\mathcal{Z}$, if the state $\boldsymbol{x}$ is still feasible, the condition (6.25) is automatically recovered generating a reference motion that is reactive to disturbances. Robust recursive feasibility is ensured for any disturbance $\hat{u} \in \mathcal{V}$ [Mayne 2005, prop. 3]. We call Closed-Loop MPC (CL-MPC) this initialization.

Thanks to the extra degree of freedom introduced in the initial state by this latter approach, the MPC can get access to control also the feedback term $\boldsymbol{K}\tilde{\boldsymbol{x}}$, inserting artificially a tracking error $\tilde{x} \in \mathcal{Z}$. We show this property in the simulation of Fig. 6.6: Without disturbances, the DCM must be moved from the boundary of the reference constraint to the center of the support polygon. Using the standard OL-MPC (initialized in $\boldsymbol{x}_{ref\cdot(1|i-1)}$), this task is impossible since it requires the cCoP p^c_{ref} to be outside the reference constraint. CL-MPC, however, uses an additional input $\boldsymbol{K}\tilde{\boldsymbol{x}}$ to drive the DCM according to the aimed motion while keeping the reference cCoP p^c_{ref} within its restriction. Notice that in this case, since there are not disturbances, DCL-MPC behaves in the same form as OL-MPC.

As mentioned, the current state $\boldsymbol{x}_{(0|i)}$ is not always available to initialize the reference motion, but even when DCL-MPC is feasible, it annuls the tracking error

$$\boldsymbol{x}_{(0|i)} - \boldsymbol{x}_{ref\cdot(0|i)} = \tilde{\boldsymbol{x}} = 0, \tag{6.28}$$

and, therefore, the feedback term $\boldsymbol{K}\tilde{\boldsymbol{x}}$. Let's show how easily DCL-MPC can fail in the simulation of Fig. 6.7: We aim to maintain the DCM on the reference constraint boundary while disturbances affect the robot. We sample the feedback law (3.33) every $\tau = 5$ ms [Kajita 2010], while the MPC is recomputed every $T = 100$ ms [Wieber 2006b]. So, we can see that in each time-step T, the feedback term is annulled during 5 ms, which ends up producing the divergence of the DCM. We show in Fig. 6.8 how the same task can be achieved by OL-MPC and CL-MPC which produce the same result.

Let's compare more dynamically the robot behavior with these three initializations (6.24), (6.26), (6.27) in the walking scenario of Fig. 6.9: We aim to realize two steps on place, then move 0.5 m on the side, and walk on place six steps to stop and stay standing on the seventh step. Disturbances appear at time 5.6 s with a constant value until the end of the simulation. We can observe that the closed-loop scheme is able to avoid the overshot that appears at 4.5 s thanks to its less restricted motion and maintains the system stable while stopping on one foot.

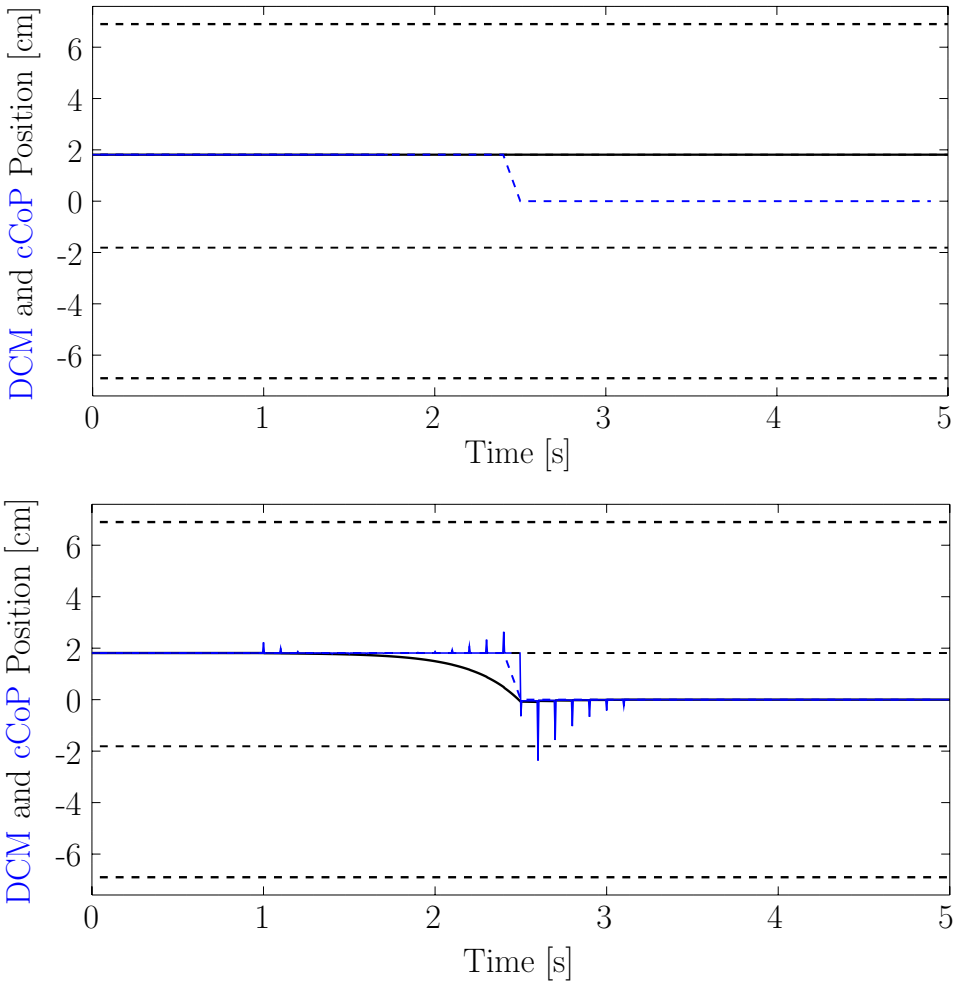

Figure 6.6: Standing simulation. without uncertainties, we aim (as shown in dashed blue lines) to move the DCM from the reference constraint boundary (dashed black line) towards the center of the foot. The required control action is infeasible for OL-MPC (top), while CL-MPC (bottom) uses the feedback term producing an artificial tracking error $\tilde{\boldsymbol{x}}$. Parameters: $\tau = 5$ ms, $T = 100$ ms, system P→C$\dot{\text{C}}$.

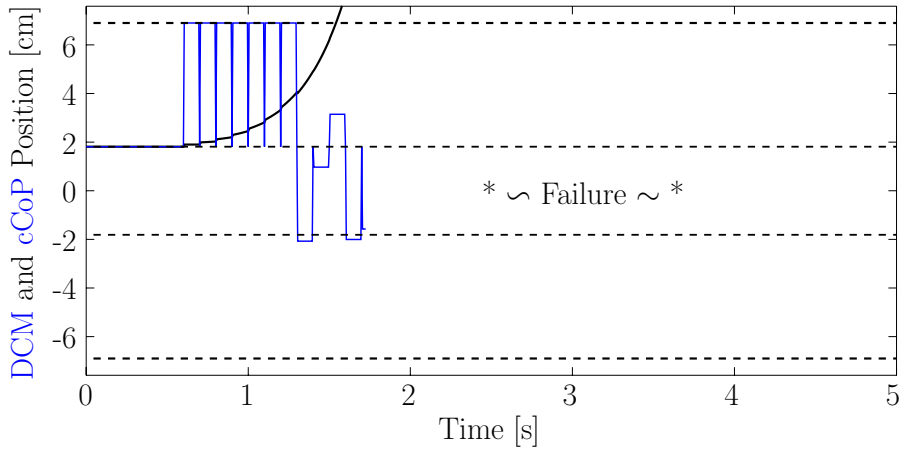

Figure 6.7: Standing Simulation. Using DCL-MPC (initialized as $\boldsymbol{x}_{ref\cdot(0|i)} = \boldsymbol{x}_{(0|i)}$) we aim to maintain the DCM on the reference constraint boundary (black dashed line). When disturbances appear at time 0.6 s, the commanded input $u_{ref\cdot(0|i)} + \boldsymbol{K}\tilde{\boldsymbol{x}}$ (shown in blue) stabilize the motion up to the time 0.7 s, when $\tilde{\boldsymbol{x}}$ is annulled and the DCM (shown with solid black curve) starts the divergence. In this simulation we relaxed the terminal constraint (6.20) for the feasibility of the reference motion after the first disturbance. Parameters: $\tau = 5$ ms, $T = 100$ ms, system P→CC̈.

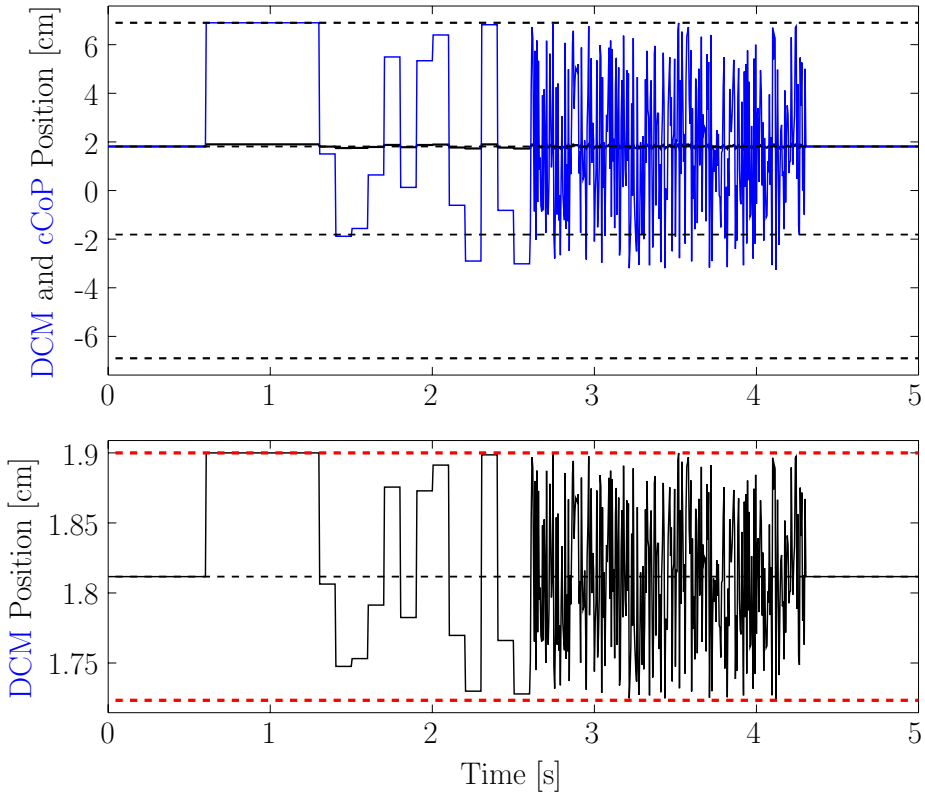

Figure 6.8: Standing simulation. Using OL-MPC or CL-MPC, we aim to maintain the DCM on the reference constraint boundary (black dashed line) while disturbances affect the robot. The DCM is maintained bounded in the set $[1 \quad \omega^{-1}]\mathcal{Z}$ (bottom) and the commanded cCoP (blue curve) in the support polygon (top). Parameters: $\tau = 5$ ms, $T = 100$ ms, system P→CC̈.

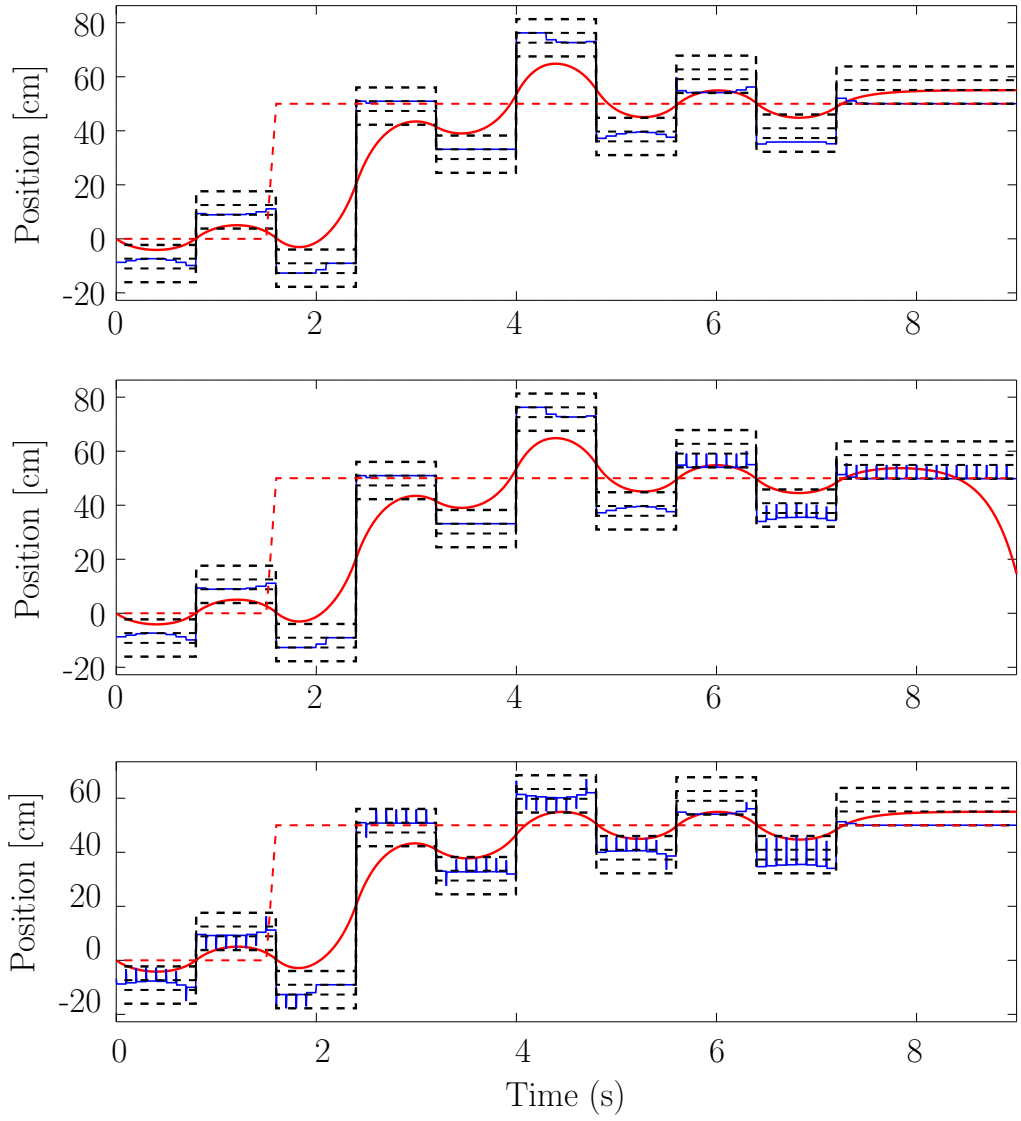

Figure 6.9: Walking simulation. We compare the walking motion generated when using OL-MPC (top), DCL-MPC (middle) and CL-MPC (bottom). Following the aimed CoM (red dashed lines), only CL-MPC is able to avoid the overshot at 4.5 s thanks to the input $\boldsymbol{K}\tilde{\boldsymbol{x}}$ used on previous steps. When disturbances appear at 5.6 s, only OL-MPC and CL-MPC maintain the stability. In the simulation with DCL-MPC, we relaxed the terminal constraint at the end of the simulation to avoid the infeasibility of the controller letting the simulation continue. Parameters: $\tau = 5$ ms, $T = 100$ ms, system P$\rightarrow$C$\dot{\text{C}}$.

6.4 Optimization Problem

Finally the optimization problem that we are considering to decide the control sequence $\boldsymbol{U}_{ref\cdot i}$ is of the form:

$$\begin{aligned} &\underset{\Delta \boldsymbol{U}_{ref\cdot i},\, \Delta \boldsymbol{S}_i,\, \boldsymbol{x}_{ref\cdot(0|i)}}{\text{minimize}} && V_i(\boldsymbol{U}_{ref\cdot i}, \boldsymbol{x}_{ref\cdot(0|i)}) : (6.19) \\ &\text{subject to} && \text{constraints} \begin{cases} \text{physical} : (6.5), (6.6), (6.7) \\ \text{terminal} : (6.20) \\ \text{initial} : (6.27). \end{cases} \end{aligned} \tag{6.29}$$

6.5 Conclusion

We have described a standard MPC scheme to generate reference motions satisfying the system dynamics (3.38). In order to ensure long term feasibility, reference motions generated by MPC must always be able to reach a given terminal set within the preview horizon time. The restrictiveness introduced in this way, to ensure feasibility, can be reduced using bigger terminal sets. We have proposed stopping terminal sets that minimize this restrictiveness for systems P→X and P→C$\dot{\text{C}}$ since they contain any feasible state (6.6) (6.7) for an standing still robot, and a quite loose terminal set for the system P_d→XP.

Every implementation of MPC in legged locomotion uses an initial state, determined by some sort of initial constraint, to compute the motion along each preview horizon. We have shown that the standard initial constraint $\boldsymbol{x}_{ref\cdot(0|i)} = \boldsymbol{x}_{ref\cdot(1|i\text{-}1)}$ is quite restrictive when working with uncertainties. Using the freer initial constraint (6.27), we can reduce this restrictiveness letting the MPC indirectly control the feedback term $\boldsymbol{K}\tilde{\boldsymbol{x}}$ and producing reference motions reactive to strong perturbations.

Chapter 7

Conclusions

This thesis aims to contribute to the development of conceivable legged robots in terms of robustness, operability, and cost for real applications.

As a first step in this discussion, we presented in Chapter 2 the complete CoM dynamics showing that most of the terms typically neglected are bounded, can be directly controlled, or have no effect on common scenarios. Errors in the estimation of these non-linear dynamics constitute, however, a source of uncertainties. Main sources of uncertainty along a standard control scheme have been reported in Chapter 3. Using a simple feedback law to track some desired reference motion, we obtained a stable closed-loop dynamics for the tracking error.

As a consequence of this stable dynamics, we showed in Chapter 4 that bounded uncertainties result in bounded tracking errors. We obtained analytically the tracking error bound and the worst sequence of disturbances depending on the closed-loop eigenstructure. Considering this bound on the tracking error we discussed the conditions to guarantee the safe operation of the robot. In order to understand better the relation between the tracking error bound and our choice of control parameters, we developed maps of the tracking error behavior in Chapter 5. Using these maps, we chose feedback gains that minimize the tracking error bound, reducing therefore the resources required to ensure the safe operation of the robot. We observed that the region of gains with minimum tracking error is independent of the sampling period and presents also minimum sensitivity to variations on the parameter ω introduced by the vertical motion of the robot. We also analyzed the effects of an arbitrary ground compliance on the tracking error bound with numerically optimized feedback gains, observing that it is normally bounded by the case of rigid ground interactions.

In order to ensure safety guarantees, the reference motion must be constrained taking into account the tracking error bound as we showed in the MPC scheme presented in Chapter 6. When the reference motion is generated online we have more information available, but how to introduce it in our MPC scheme is not intuitive. For this, we discuss the initial constraint proposed in [Mayne 2005] compared with standard choices in legged robot controllers. We have seen that this initial constraint also provide a valuable contribution to reduce the motion restrictiveness, reducing once again the resources required to ensure a safe operation of the robot.

Appendix A

Set Operations

We define the following set operations in order to maintain a simplified notation.

- **Product of scalar and set** ($c\mathcal{A}$)

$$\begin{gathered}\text{Given a scalar } c \in \mathbb{R} \text{ and a set } \mathcal{A} \subseteq \mathbb{R}^n, \\ \text{we denote } c\mathcal{A} \text{ to a new set defined as:} \\ c\mathcal{A} \equiv \{c\boldsymbol{a} \mid \boldsymbol{a} \in A\} \subseteq \mathbb{R}^n.\end{gathered}$$

- **Product of vector and set** ($\boldsymbol{v}\mathcal{A}$)

$$\begin{gathered}\text{Given a vector (or matrix) } \boldsymbol{v} \in \mathbb{R}^{n\times m} \text{ and a set } \mathcal{A} \subseteq \mathbb{R}^n, \\ \text{we denote } \boldsymbol{v}\mathcal{A} \text{ to a new set defined as:} \\ \boldsymbol{v}\mathcal{A} \equiv \{\boldsymbol{v}^\top \boldsymbol{a} \mid \boldsymbol{a} \in \mathcal{A}\} \subseteq \mathbb{R}^m.\end{gathered}$$

- **Sum of vector and set** ($\boldsymbol{v} + \mathcal{A}$)

$$\begin{gathered}\text{Given a vector } \boldsymbol{v} \in \mathbb{R}^n \text{ and a set } \mathcal{A} \subseteq \mathbb{R}^n, \\ \text{we denote } \boldsymbol{v} + \mathcal{A} \text{ to a new set defined as:} \\ \boldsymbol{v} + \mathcal{A} \equiv \{\boldsymbol{v} + \boldsymbol{a} \mid \boldsymbol{a} \in \mathcal{A}\} \subseteq \mathbb{R}^n.\end{gathered}$$

- **Minkowski sum** ($\mathcal{A} \oplus \mathcal{B}$)

$$\begin{gathered}\text{Given sets } \mathcal{A}, \mathcal{B} \subseteq \mathbb{R}^n, \\ \text{we denote } \mathcal{A} \oplus \mathcal{B} \text{ to a new set defined as:} \\ \mathcal{A} \oplus \mathcal{B} \equiv \{\boldsymbol{a} + \boldsymbol{b} \mid \boldsymbol{a} \in \mathcal{A},\ \boldsymbol{b} \in \mathcal{B}\} \subseteq \mathbb{R}^n.\end{gathered}$$

- **Pontryagin difference** ($\mathcal{A} \ominus \mathcal{B}$)

$$\begin{gathered}\text{Given sets } \mathcal{A}, \mathcal{B} \subseteq \mathbb{R}^n, \\ \text{we denote } \mathcal{A} \ominus \mathcal{B} \text{ to a new set defined as:} \\ \mathcal{A} \ominus \mathcal{B} \equiv \{\boldsymbol{x} \mid \boldsymbol{x} + \mathcal{B} \subseteq \mathcal{A}\} \subseteq \mathbb{R}^n.\end{gathered}$$

- **Intersection of sets** ($\mathcal{A} \cap \mathcal{B}$)

$$\begin{gathered}\text{Given sets } \mathcal{A}, \mathcal{B} \subseteq \mathbb{R}^n, \\ \text{we denote } \mathcal{A} \cap \mathcal{B} \text{ to a new set defined as:} \\ \mathcal{A} \cap \mathcal{B} \equiv \{\boldsymbol{x} \mid \boldsymbol{x} \in \mathcal{A} \quad \text{and} \quad \boldsymbol{x} \in \mathcal{B}\} \subseteq \mathbb{R}^n.\end{gathered}$$

Appendix B

Vertex Convergence

Using the diagonal form (4.22) of the closed-loop matrix, the stationary vertex $\boldsymbol{z}_0$ (4.45) is obtained from the convergence:

$$\begin{aligned}\boldsymbol{z}_0 &= \sum_{i=0}^{\infty} (\boldsymbol{A}+\boldsymbol{B}\boldsymbol{K})^i \boldsymbol{B}\hat{u}_{(i|0)} \\ &= \sum_{i=0}^{\infty} \boldsymbol{M}\begin{bmatrix} q_{\mathrm{M}}^i & 0 \\ 0 & q_m^i \end{bmatrix}\boldsymbol{M}^{-1}\boldsymbol{B}\, s_{\mathrm{M}}^i \,\mathrm{sign}(\alpha_{\mathrm{M}})\,\hat{u}_{\mathrm{peak}} \\ &= \boldsymbol{M}\begin{bmatrix} \sum\limits_{i=0}^{\infty} q_{\mathrm{M}}^i\, s_{\mathrm{M}}^i & 0 \\ 0 & \sum\limits_{i=0}^{\infty} q_m^i\, s_{\mathrm{M}}^i \end{bmatrix}\boldsymbol{M}^{-1}\boldsymbol{B}\,\mathrm{sign}(\alpha_{\mathrm{M}})\,\hat{u}_{\mathrm{peak}} \end{aligned} \tag{B.1}$$

So, iterating from $\boldsymbol{z}_0$ in the closed-loop dynamics (3.39) with disturbances of the sequence $\hat{\boldsymbol{U}}_0$ (4.38), we have:

$$\begin{aligned}&(\boldsymbol{A}+\boldsymbol{B}\boldsymbol{K})\boldsymbol{z}_0 + \boldsymbol{B}\hat{u}_{(1|0)} = (\boldsymbol{A}+\boldsymbol{B}\boldsymbol{K})\boldsymbol{z}_0 + \boldsymbol{B}\, s_{\mathrm{M}}\,\mathrm{sign}(\alpha_{\mathrm{M}})\,\hat{u}_{\mathrm{peak}} \\ &= \boldsymbol{M}\begin{bmatrix} q_{\mathrm{M}} & 0 \\ 0 & q_m \end{bmatrix}\boldsymbol{M}^{-1}\boldsymbol{M}\begin{bmatrix} \sum\limits_{i=0}^{\infty} q_{\mathrm{M}}^i\, s_{\mathrm{M}}^i & 0 \\ 0 & \sum\limits_{i=0}^{\infty} q_m^i\, s_{\mathrm{M}}^i \end{bmatrix}\boldsymbol{M}^{-1}\boldsymbol{B}\,\mathrm{sign}(\alpha_{\mathrm{M}})\,\hat{u}_{\mathrm{peak}} + \boldsymbol{B}\, s_{\mathrm{M}}\,\mathrm{sign}(\alpha_{\mathrm{M}})\,\hat{u}_{\mathrm{peak}} \\ &= \boldsymbol{M}\begin{bmatrix} \sum\limits_{i=0}^{\infty} q_{\mathrm{M}}^{i+1}\, s_{\mathrm{M}}^i & 0 \\ 0 & \sum\limits_{i=0}^{\infty} q_m^{i+1}\, s_{\mathrm{M}}^i \end{bmatrix}\boldsymbol{M}^{-1}\boldsymbol{B}\,\mathrm{sign}(\alpha_{\mathrm{M}})\,\hat{u}_{\mathrm{peak}} + \boldsymbol{M}\begin{bmatrix} q_{\mathrm{M}}^0\, s_{\mathrm{M}} & 0 \\ 0 & q_m^0\, s_{\mathrm{M}} \end{bmatrix}\boldsymbol{M}^{-1}\boldsymbol{B}\,\mathrm{sign}(\alpha_{\mathrm{M}})\,\hat{u}_{\mathrm{peak}} \\ &= \boldsymbol{M}\begin{bmatrix} \sum\limits_{i=0}^{\infty} q_{\mathrm{M}}^{i+1}\, s_{\mathrm{M}}^i + q_{\mathrm{M}}^0 s_{\mathrm{M}} & 0 \\ 0 & \sum\limits_{i=0}^{\infty} q_m^{i+1}\, s_{\mathrm{M}}^i + q_m^0 s_{\mathrm{M}} \end{bmatrix}\boldsymbol{M}^{-1}\boldsymbol{B}\,\mathrm{sign}(\alpha_{\mathrm{M}})\,\hat{u}_{\mathrm{peak}} \\ &= \boldsymbol{M}\begin{bmatrix} \sum\limits_{i=0}^{\infty} q_{\mathrm{M}}^i\, s_{\mathrm{M}}^{i-1} & 0 \\ 0 & \sum\limits_{i=0}^{\infty} q_m^i\, s_{\mathrm{M}}^{i-1} \end{bmatrix}\boldsymbol{M}^{-1}\boldsymbol{B}\,\mathrm{sign}(\alpha_{\mathrm{M}})\,\hat{u}_{\mathrm{peak}} \\ &= s_{\mathrm{M}}\boldsymbol{M}\begin{bmatrix} \sum\limits_{i=0}^{\infty} q_{\mathrm{M}}^i\, s_{\mathrm{M}}^i & 0 \\ 0 & \sum\limits_{i=0}^{\infty} q_m^i\, s_{\mathrm{M}}^i \end{bmatrix}\boldsymbol{M}^{-1}\boldsymbol{B}\,\mathrm{sign}(\alpha_{\mathrm{M}})\,\hat{u}_{\mathrm{peak}}, \end{aligned} \tag{B.2}$$

that is $s_{\mathrm{M}}\boldsymbol{z}_0$ from (B.1), so:

$$s_{\mathrm{M}}\boldsymbol{z}_0 = (\boldsymbol{A} + \boldsymbol{B}\boldsymbol{K})\boldsymbol{z}_0 + \boldsymbol{B}\hat{u}_{(1|0)}. \tag{B.3}$$

Similarly, we can obtain for the next iteration that:

$$\boldsymbol{z}_0 = s_{\mathrm{M}}^2\boldsymbol{z}_0 = (\boldsymbol{A} + \boldsymbol{B}\boldsymbol{K})s_{\mathrm{M}}\boldsymbol{z}_0 + \boldsymbol{B}\hat{u}_{(2|0)}. \tag{B.4}$$

We conclude, therefore, that applying the sequence $\hat{\boldsymbol{U}}_0$, the tracking error converges to a stationary condition in which alternates between $\boldsymbol{z}_0$ and $s_{\mathrm{M}}\boldsymbol{z}_0$.

Appendix C

Complex-Conjugate Coefficients

We determine in following the form of coefficients α_1, α_2 when poles q_1, q_2 are complex-conjugate.

Since matrices $\boldsymbol{L}$, $\boldsymbol{B}$ and $\boldsymbol{A}+\boldsymbol{B}\boldsymbol{K}$ are real-valued, we know that:

$$\boldsymbol{L}\boldsymbol{B} \in \mathbb{R} \tag{C.1}$$

$$\boldsymbol{L}(\boldsymbol{A}+\boldsymbol{B}\boldsymbol{K})\boldsymbol{B} \in \mathbb{R}. \tag{C.2}$$

Let's consider coefficients of the form $\alpha_1 = a_1 + jb_1$ and $\alpha_2 = a_2 + jb_2$. From the definition of these coefficients (4.24), in (C.1) we have:

$$\begin{aligned}
\boldsymbol{L}\boldsymbol{B} =& \boldsymbol{L}\boldsymbol{M}\boldsymbol{M}^{-1}\boldsymbol{B} && \text{(C.3)}\\
=& \boldsymbol{L}\boldsymbol{M}_{\mathtt{c},1}\boldsymbol{M}_{\mathtt{r},1}^{-1}\boldsymbol{B} + \boldsymbol{L}\boldsymbol{M}_{\mathtt{c},2}\boldsymbol{M}_{\mathtt{r},2}^{-1}\boldsymbol{B} && \text{(C.4)}\\
=& \alpha_1 + \alpha_2 && \text{(C.5)}\\
=& a_1 + a_2 + j(b_1 + b_2) \in \mathbb{R}, && \text{(C.6)}
\end{aligned}$$

which means that $b_1 = -b_2 = b$. Diagonalizing the matrix $\boldsymbol{A}+\boldsymbol{B}\boldsymbol{K}$ (4.22) in (C.2) we have:

$$\begin{aligned}
\boldsymbol{L}(\boldsymbol{A}+\boldsymbol{B}\boldsymbol{K})\boldsymbol{B} =& \boldsymbol{L}\boldsymbol{M}\begin{bmatrix} q_1 & 0 \\ 0 & q_2 \end{bmatrix}\boldsymbol{M}^{-1}\boldsymbol{B} && \text{(C.7)}\\
=& \alpha_1 q_1 + \alpha_2 q_2 \in \mathbb{R}, && \text{(C.8)}
\end{aligned}$$

considering poles of the form $q_{1,\,2} = q\,\mathrm{e}^{\pm j\theta}$, it is:

$$\alpha_1 q_1 + \alpha_2 q_2 = \left(a_1 \mathrm{e}^{j\theta} + a_2 \mathrm{e}^{-j\theta}\right) q + jb\left(\mathrm{e}^{j\theta} - \mathrm{e}^{-j\theta}\right) q \in \mathbb{R} \tag{C.9}$$

since $jb\left(\mathrm{e}^{j\theta} - \mathrm{e}^{-j\theta}\right) = -2b\sin(\theta) \in \mathbb{R}$, it requires that

$$a_1 \mathrm{e}^{j\theta} + a_2 \mathrm{e}^{-j\theta} \in \mathbb{R}, \tag{C.10}$$

which means that $a_1 = a_2 = a$. We conclude, therefore, that the coefficients α_1, α_2 are also complex-conjugate:

$$\alpha_1 = a + jb \qquad\qquad \alpha_2 = a - jb. \tag{C.11}$$

Appendix D

Terminal Constraints

D.1 Definitions

Definition D.1. ***Positively Invariant Set*** *[Kerrigan 2000]. The non-empty set $\mathcal{X}_{\text{TER}}$ is positively invariant for the closed-loop system*

$$\boldsymbol{x}_{ref}^{+} = (\boldsymbol{A} + \boldsymbol{B}\boldsymbol{K})\boldsymbol{x}_{ref}, \tag{D.1}$$

if and only if it satisfies the reference constraints

$$\mathcal{X}_{\text{TER}} \subset \mathcal{X} \ominus \mathcal{Z}, \tag{D.2}$$
$$\boldsymbol{K}\mathcal{X}_{\text{TER}} \subset \mathcal{U} \ominus \boldsymbol{K}\mathcal{Z} \ominus \mathcal{V}, \tag{D.3}$$

and any state $\boldsymbol{x}$ in the set, evolves always contained in the set:

$$\boldsymbol{x}_{ref} \in \mathcal{X}_{\text{TER}} \implies \boldsymbol{x}_{ref}^{+} \in \mathcal{X}_{\text{TER}}. \tag{D.4}$$

Definition D.2. ***Control Positively Invariant Set*** *[Kerrigan 2000]. The non-empty set $\mathcal{X}_{\text{TER}}$ is control positively invariant for the system*

$$\boldsymbol{x}_{ref}^{+} = \boldsymbol{A}\boldsymbol{x}_{ref} + \boldsymbol{B}u_{ref}, \tag{D.5}$$

if and only if there exists a feedback control law $u_{ref} = f(\boldsymbol{x}_{ref})$ such that this set is positively invariant for the resulting closed-loop system.

D.2 Terminal Sets

We justify, in following, our choice of terminal constraint considering the control law [Sugihara 2009]:

$$\Delta p_{ref}^{c} = k_{ref}\Delta\xi_{ref}, \qquad \text{with} \qquad 1 < k_{ref} < \frac{\mathrm{e}^{\omega\tau}}{\mathrm{e}^{\omega\tau} - 1}, \tag{D.6}$$

for systems P→X and P→C$\dot{\text{C}}$, and the control law

$$\Delta p_{des\cdot ref}^{c} = \left(1 + \frac{\omega}{\gamma}\right)\Delta\xi_{ref} - \frac{\omega}{\gamma}\Delta p_{ref}^{c}, \tag{D.7}$$

for the system P_d→XP.

P→X

From the closed-loop form (3.54), we can write this closed-loop system as

$$\Delta\xi^{+}_{ref} = \big(1 - (\mathrm{e}^{\omega\tau} - 1)(k_{ref} - 1)\big)\Delta\xi_{ref}, \tag{D.8}$$

where the DCM evolves towards the CoF from any state in the set $\mathcal{X}_{\text{TER}}$ defined by the feasible inputs (6.6):

$$\underline{\Delta p^{c}} + \tilde{p}^{c}_{\text{peak}} \leq k_{ref}\Delta\xi_{ref} \leq \overline{\Delta p^{c}} - \tilde{p}^{c}_{\text{peak}}, \tag{D.9}$$

with feedback gains k_{ref} in (D.6). We can obtain the biggest feasible control positively invariant set when k_{ref} tends to 1:

$$\underline{\Delta p^{c}} + \tilde{p}^{c}_{\text{peak}} < \Delta\xi_{ref} < \overline{\Delta p^{c}} - \tilde{p}^{c}_{\text{peak}}. \tag{D.10}$$

P→CĊ

Changing variables, the closed-loop system is equivalently:

$$\begin{bmatrix}\Delta c^{+}_{ref}\\ \Delta\xi^{+}_{ref}\end{bmatrix} = \begin{bmatrix}\mathrm{e}^{-\omega\tau} & \sinh(\omega\tau)\\ 0 & \mathrm{e}^{\omega\tau}\end{bmatrix}\begin{bmatrix}\Delta c_{ref}\\ \Delta\xi_{ref}\end{bmatrix} + \begin{bmatrix}1-\cosh(\omega\tau)\\ 1-\mathrm{e}^{\omega\tau}\end{bmatrix}k_{ref}\Delta\xi_{ref}. \tag{D.11}$$

The DCM (second row) evolves towards the CoF from any state as shown in (D.8). Working on the first row, a given position Δc^{+}_{ref} can only be reached from:

$$\Delta c_{ref} = \left(\mathrm{e}^{\omega\tau} - \frac{\mathrm{e}^{\omega\tau}-1}{2}\Big((\mathrm{e}^{\omega\tau}+1) - k_{ref}(\mathrm{e}^{\omega\tau}-1)\Big)\frac{\Delta\xi_{ref}}{\Delta c^{+}_{ref}}\right)\Delta c^{+}_{ref}, \tag{D.12}$$

So, the CoM can only reach its feasibility boundary $\overline{\Delta c} - \tilde{c}_{\text{peak}}$ (6.7) from outside:

$$\begin{aligned}\Delta c_{ref} &= \left(\mathrm{e}^{\omega\tau} - \frac{\mathrm{e}^{\omega\tau}-1}{2}\Big((\mathrm{e}^{\omega\tau}+1) - k_{ref}(\mathrm{e}^{\omega\tau}-1)\Big)\frac{(\overline{\Delta p^{c}} - \tilde{p}^{c}_{\text{peak}})/k_{ref}}{\overline{\Delta c} - \tilde{c}_{\text{peak}}}\right)(\overline{\Delta c} - \tilde{c}_{\text{peak}})\\ &> \left(\mathrm{e}^{\omega\tau} - \frac{\mathrm{e}^{\omega\tau}-1}{2}\Big((\mathrm{e}^{\omega\tau}+1) - k_{ref}(\mathrm{e}^{\omega\tau}-1)\Big)\right)(\overline{\Delta c} - \tilde{c}_{\text{peak}})\\ &> \overline{\Delta c} - \tilde{c}_{\text{peak}},\end{aligned} \tag{D.13}$$

where we first use that $(\overline{\Delta p^{c}} - \tilde{p}^{c}_{\text{peak}})/k_{ref} < \overline{\Delta c} - \tilde{c}_{\text{peak}}$, and then, that the stable gains are such that $1 < k_{ref}$ (D.6). Therefore, the control law (D.6) maintains the state contained in the feasible set $\mathcal{X}_{\text{TER}}$ defined as:

$$\underline{\Delta p^{c}} + \tilde{p}^{c}_{\text{peak}} \leq k_{ref}\Delta\xi_{ref} \leq \overline{\Delta p^{c}} - \tilde{p}^{c}_{\text{peak}}, \quad \underline{\Delta c} + \tilde{c}_{\text{peak}} \leq \Delta c_{ref} \leq \overline{\Delta c} - \tilde{c}_{\text{peak}}, \tag{D.14}$$

We can obtain the biggest feasible control positively invariant set when $k_{ref} \to 1$:

$$\underline{\Delta p^{c}} + \tilde{p}^{c}_{\text{peak}} < \Delta\xi_{ref} < \overline{\Delta p^{c}} - \tilde{p}^{c}_{\text{peak}}, \quad \underline{\Delta c} + \tilde{c}_{\text{peak}} \leq \Delta c_{ref} \leq \overline{\Delta c} - \tilde{c}_{\text{peak}}. \tag{D.15}$$

$\mathbf{P}_d \rightarrow \mathbf{XP}$

From this system dynamics (3.31), the DCM evolves as

$$\begin{aligned}\Delta\xi^{+}_{ref} =& \frac{\omega\Delta p^{c}_{ref} + \gamma\Delta p^{c}_{des\cdot ref}}{\omega+\gamma} + \mathrm{e}^{\omega\tau}\left(\Delta\xi_{ref} - \frac{\omega\Delta p^{c}_{ref} + \gamma\Delta p^{c}_{des\cdot ref}}{\omega+\gamma}\right) \\ &+ \frac{\omega(1-\mathrm{e}^{-\gamma\tau})}{\omega+\gamma}(\Delta p^{c}_{des\cdot ref} - \Delta p^{c}_{ref}),\end{aligned} \tag{D.16}$$

that considering the control law (D.7), becomes

$$\Delta\xi^{+}_{ref} - \Delta\xi_{ref} = (1-\mathrm{e}^{-\gamma\tau})(\Delta p^{c}_{des\cdot ref} - \Delta\xi_{ref}), \tag{D.17}$$

and the cCoP evolves as

$$\Delta p^{c+}_{ref} - \Delta p^{c}_{ref} = (1-\mathrm{e}^{-\gamma\tau})(\Delta p^{c}_{des\cdot ref} - \Delta p^{c}_{ref}). \tag{D.18}$$

Both converge to the desired cCoP $\Delta p^{c}_{des\cdot ref}$, which stays constant according to the control law (D.7):

$$\begin{aligned}\Delta p^{c+}_{des\cdot ref} =& \left(1+\frac{\omega}{\gamma}\right)\Delta\xi^{+}_{ref} - \frac{\omega}{\gamma}\Delta p^{c+}_{ref} \\ =& \left(1+\frac{\omega}{\gamma}\right)\left(\Delta\xi_{ref} + (1-\mathrm{e}^{-\gamma\tau})(\Delta p^{c}_{des\cdot ref} - \Delta\xi_{ref})\right) \\ &- \frac{\omega}{\gamma}\left(\Delta p^{c}_{ref} + (1-\mathrm{e}^{-\gamma\tau})(\Delta p^{c}_{des\cdot ref} - \Delta p^{c}_{ref})\right) \\ =& (1-\mathrm{e}^{-\gamma\tau})\Delta p^{c}_{des\cdot ref} + \mathrm{e}^{-\gamma\tau}\left(\left(1+\frac{\omega}{\gamma}\right)\Delta\xi_{ref} - \frac{\omega}{\gamma}\Delta p^{c}_{ref}\right) \\ =& \Delta p^{c}_{des\cdot ref}.\end{aligned} \tag{D.19}$$

Therefore, any state in the set $\mathcal{X}_{\text{TER}}$ defined as

$$\underline{\Delta p^{c}} + \tilde{p}^{c}_{\text{peak}} \leq \Delta p^{c}_{ref} \leq \overline{\Delta p^{c}} - \tilde{p}^{c}_{\text{peak}}, \tag{D.20}$$

$$\underline{\Delta p^{c}} + \tilde{p}^{c}_{\text{peak}} \leq \left(1+\frac{\omega}{\gamma}\right)\Delta\xi_{ref} - \frac{\omega}{\gamma}\Delta p^{c}_{ref} = \Delta p^{c}_{des\cdot ref} \leq \overline{\Delta p^{c}} - \tilde{p}^{c}_{\text{peak}}. \tag{D.21}$$

is maintained in this set by the control law (D.7). We conclude, then, that this set is a control positively invariant set.

In all cases (6.21), (6.22), (6.23) $\mathcal{X}_{\text{TER}}$ is a control positively invariant set since it is feasible and there exist some control law (D.6), (D.7) such that any state in this set evolves always contained in this set.

Bibliography

[Agravante 2016] D. J. Agravante, A. Sherikov, P.-B. Wieber, A. Cherubini and A. Kheddar. *Walking pattern generators designed for physical collaboration.* In IEEE International Conference on Robotics and Automation (ICRA), pages 1573–1578, 2016. (Cited on pages 6, 10, and 55.)

[Benallegue 2015] M. Benallegue, A. Mifsud and F. Lamiraux. *Fusion of force-torque sensors, inertial measurements units and proprioception for a humanoid kinematics-dynamics observation.* In IEEE-RAS International Conference on Humanoid Robots (Humanoids), pages 664–669, 2015. (Cited on page 52.)

[Bohórquez 2016] N. Bohórquez, A. Sherikov, D. Dimitrov and P.-B. Wieber. *Safe navigation strategies for a biped robot walking in a crowd.* In EEE-RAS International Conference on Humanoid Robots (Humanoids), pages 379–386, 2016. (Cited on pages 7, 8, 10, 55, and 59.)

[Bohorquez 2018] N. Bohorquez. *Design of safe control laws for the locomotion of biped robots.* PhD thesis, Université Grenoble Alpes, 2018. (Cited on page 12.)

[Bolotnikova 2017] A. Bolotnikova, K. Chappellet, A. Paolillo, A. Escande, G. Anbarjafari, A. Suarez-Roos, P. Rabaté and A. Kheddar. *A circuit-breaker use-case operated by a humanoid in aircraft manufacturing.* In IEEE Conference on Automation Science and Engineering (CASE), pages 15–22, 2017. (Cited on page 1.)

[Brasseur 2015] C. Brasseur, A. Sherikov, C. Collette, D. Dimitrov and P.-B. Wieber. *A robust linear MPC approach to online generation of 3D biped walking motion.* In IEEE-RAS International Conference on Humanoid Robots (Humanoids), pages 595–601, 2015. (Cited on pages 7, 8, 12, and 44.)

[Brossette 2017] S. Brossette and P.-B. Wieber. *Collision avoidance based on separating planes for feet trajectory generation.* In IEEE-RAS International Conference on Humanoid Robotics (Humanoids), pages 509–514, 2017. (Cited on page 10.)

[Caron 2015] S. Caron, Q.-C. Pham and Y. Nakamura. *Stability of surface contacts for humanoid robots: Closed-form formulae of the contact wrench cone for rectangular support areas.* In IEEE International Conference on Robotics and Automation (ICRA), pages 5107–5112, 2015. (Cited on page 8.)

[Caron 2019] S. Caron, A. Kheddar and O. Tempier. *Stair climbing stabilization of the HRP-4 humanoid robot using whole-body admittance control.* In IEEE International Conference on Robotics and Automation (ICRA), pages 277–283, 2019. (Cited on page 52.)

[Choi 2006] Y. Choi, D. Kim and B.-J. You. *On the walking control for humanoid robot based on the kinematic resolution of com jacobian with embedded motion.* In IEEE International Conference on Robotics and Automation (ICRA), pages 2655–2660, 2006. (Cited on pages 7 and 55.)

[Ciocca 2017] M. Ciocca, P.-B. Wieber and T. Fraichard. *Strong recursive feasibility in model predictive control of biped walking.* In IEEE-RAS International Conference on Humanoid Robotics (Humanoids), pages 730–735, 2017. (Cited on page 58.)

[Ciocca 2019] M. Ciocca, P.-B. Wieber and T. Fraichard. *Effect of Planning Period on MPC-based Navigation for a Biped Robot in a Crowd.* In IEEE/RSJ International Conference on Intelligent Robots and Systems (IROS), pages 491–496, 2019. (Cited on page 8.)

[Dune 2011] C. Dune, A. Herdt, E. Marchand, O. Stasse, P.-B. Wieber and E. Yoshida. *Vision based control for humanoid robots.* In IROS Workshop on Visual Control of Mobile Robots (ViCoMoR), pages 19–26, 2011. (Cited on page 55.)

[Englsberger 2011] J. Englsberger, C. Ott, M. A. Roa, A. Albu-Schäffer and G. Hirzinger. *Bipedal walking control based on capture point dynamics.* In IEEE/RSJ International Conference on Intelligent Robots and Systems (IROS), pages 4420–4427, 2011. (Cited on pages 7 and 40.)

[Englsberger 2014] J. Englsberger, A. Werner, C. Ott, B. Henze, M. A. Roa, G. Garofalo, R. Burger, A. Beyer, O. Eiberger, K. Schmid*et al.* *Overview of the torque-controlled humanoid robot TORO.* In IEEE-RAS International Conference on Humanoid Robots (Humanoids), pages 916–923, 2014. (Cited on page 10.)

[Englsberger 2015] J. Englsberger, C. Ott and A. Albu-Schäffer. *Three-dimensional bipedal walking control based on divergent component of motion.* IEEE Transactions on Robotics, vol. 31, no. 2, pages 355–368, 2015. (Cited on page 10.)

[Englsberger 2016] J. Englsberger. *Combining reduced dynamics models and whole-body control for agile humanoid locomotion.* PhD thesis, Technische Universität München, 2016. (Cited on page 4.)

[Englsberger 2018] J. Englsberger, G. Mesesan, A. Werner and C. Ott. *Torque-based dynamic walking-A long way from simulation to experiment.* In IEEE International Conference on Robotics and Automation (ICRA), pages 440–447, 2018. (Cited on pages 45 and 53.)

[Fang 2018] H. Fang, M. A. Haile and Y. Wang. *Robustifying the Kalman Filter against Measurement Outliers: An Innovation Saturation Mechanism.* In IEEE Conference on Decision and Control (CDC), pages 6390–6395, 2018. (Cited on page 12.)

[Feng 2015] S. Feng, E. Whitman, X. Xinjilefu and C. G. Atkeson. *Optimization-based Full Body Control for the DARPA Robotics Challenge.* Journal of Field Robotics, vol. 32, no. 2, pages 293–312, 2015. (Cited on page 59.)

[Feng 2016a] S. Feng. *Online hierarchical optimization for humanoid control.* PhD thesis, Carnegie-Mellon Univ. Pittsburgh PA Robotics Inst, 2016. (Cited on page 5.)

[Feng 2016b] S. Feng, X. Xinjilefu, C. G. Atkeson and J. Kim. *Robust dynamic walking using online foot step optimization.* In IEEE/RSJ International Conference on Intelligent Robots and Systems (IROS), pages 5373–5378, 2016. (Cited on pages 1 and 7.)

[Fernandez-Camacho 1995] E. Fernandez-Camacho and C. Bordons-Alba. Model predictive control in the process industry. Springer, 1995. (Cited on page 55.)

[Flayols 2017] T. Flayols, A. Del Prete, P. Wensing, A. Mifsud, M. Benallegue and O. Stasse. *Experimental evaluation of simple estimators for humanoid robots.* In IEEE-RAS International Conference onHumanoid Robotics (Humanoids), pages 889–895, 2017. (Cited on pages 42 and 52.)

[Gehring 2019] C. Gehring, P. Fankhauser, L. Isler, R. Diethelm, S. Bachmann, M. Potz, L. Gerstenberg and M. Hutter. *ANYmal in the Field: Solving Industrial Inspection of an Offshore HVDC Platform with a Quadrupedal Robot.* In Conference on Field and Service Robotics (FSR), 2019. (Cited on page 1.)

[Grandia 2019] R. Grandia, F. Farshidian, A. Dosovitskiy, R. Ranftl and M. Hutter. *Frequency-Aware Model Predictive Control.* IEEE Robotics and Automation Letters (RA-L), vol. 4, no. 2, pages 1517–1524, 2019. (Cited on pages 8, 10, and 11.)

[Henze 2019] B. Henze, M. A. Roa, A. Werner, A. Dietrich, C. Ott and A. Albu-Schäffer. *Experiments with human-inspired behaviors in a humanoid robot: Quasi-static balancing using toe-off motion and stretched knees.* In IEEE International Conference on Robotics and Automation (ICRA), pages 2510–2516, 2019. (Cited on page 53.)

[Herdt 2010] A. Herdt, H. Diedam, P.-B. Wieber, D. Dimitrov, K. Mombaur and M. Diehl. *Online walking motion generation with automatic footstep placement.* Advanced Robotics, vol. 24, no. 5-6, pages 719–737, 2010. (Cited on pages 8, 55, and 57.)

[Herr 2008] H. Herr and M. Popovic. *Angular momentum in human walking.* Journal of experimental biology, vol. 211, no. 4, pages 467–481, 2008. (Cited on page 7.)

[Hurmuzlu 2004] Y. Hurmuzlu, F. GéNot and B. Brogliato. *Modeling, stability and control of biped robots—a general framework.* Automatica, vol. 40, no. 10, pages 1647–1664, 2004. (Cited on pages 4 and 5.)

[Hutter 2016] M. Hutter, C. Gehring, D. Jud, A. Lauber, C. D. Bellicoso, V. Tsounis, J. Hwangbo, K. Bodie, P. Fankhauser, M. Bloesch*et al.* *Anymal-a highly mobile and dynamic quadrupedal robot.* In IEEE/RSJ International Conference on Intelligent Robots and Systems (IROS), pages 38–44, 2016. (Cited on page 10.)

[Ibanez 2012] A. Ibanez, P. Bidaud and V. Padois. *Unified preview control for humanoid postural stability and upper-limb interaction adaptation.* In IEEE/RSJ International Conference on Intelligent Robots and Systems, pages 1801–1808, 2012. (Cited on page 10.)

[Imanishi 2018] K. Imanishi and T. Sugihara. *Autonomous Biped Stepping Control Based on the LIPM Potential.* In IEEE-RAS International Conference on Humanoid Robots (Humanoids), pages 280–283, 2018. (Cited on page 58.)

[Jung 2004] B.-J. Jung, J.-S. Kong, B.-H. Lee, S.-M. Ahn and J.-G. Kim. *Backlash compensation for a humanoid robot using disturbance observer.* In Conference of IEEE Industrial Electronics Society (IECON), volume 3, pages 2142–2147, 2004. (Cited on page 11.)

[Jury 1962] E. Jury. *A simplified stability criterion for linear discrete systems.* Proceedings of the IRE, vol. 50, no. 6, pages 1493–1500, 1962. (Cited on page 16.)

[Kajita 2010] S. Kajita, M. Morisawa, K. Miura, S. Nakaoka, K. Harada, K. Kaneko, F. Kanehiro and K. Yokoi. *Biped walking stabilization based on linear inverted pendulum tracking.* In IEEE/RSJ International Conference on Intelligent Robots and Systems (IROS), pages 4489–4496, 2010. (Cited on pages 7, 10, 11, 50, 52, and 62.)

[Kemp 2008] C. Kemp, P. Fitzpatrick, H. Hirukawa, K. Yokoi, K. Harada and Y. Matsumoto. *Humanoids.* In B. Siciliano and O. Khatib, editors, Springer Handbook of Robotics, pages 361–389. Springer Berlin Heidelberg, 2008. (Cited on page 1.)

[Kerrigan 2000] E. C. Kerrigan and J. M. Maciejowski. *Invariant sets for constrained nonlinear discrete-time systems with application to feasibility in model predictive control.* In IEEE Conference on Decision and Control (Cat. No. 00CH37187), volume 5, pages 4951–4956, 2000. (Cited on page 72.)

[Kheddar 2019] A. Kheddar, S. Caron, P. Gergondet, A. Comport, A. Tanguy, C. Ott, B. Henze, G. Mesesan, J. Englsberger, M. Roa*et al.* *Humanoid robots in aircraft manufacturing.* 2019. (Cited on page 1.)

[Kim 2016] D. Kim, Y. Zhao, G. Thomas, B. R. Fernandez and L. Sentis. *Stabilizing series-elastic point-foot bipeds using whole-body operational space control.* IEEE Transactions on Robotics, vol. 32, no. 6, pages 1362–1379, 2016. (Cited on page 48.)

[Koenemann 2015] J. Koenemann, A. Del Prete, Y. Tassa, E. Todorov, O. Stasse, M. Bennewitz and N. Mansard. *Whole-body model-predictive control applied to the HRP-2 humanoid.* In IEEE/RSJ International Conference on Intelligent Robots and Systems (IROS), pages 3346–3351, 2015. (Cited on page 16.)

[Kolmanovsky 1998] I. Kolmanovsky and E. G. Gilbert. *Theory and computation of disturbance invariant sets for discrete-time linear systems.* Mathematical problems in engineering, vol. 4, no. 4, pages 317–367, 1998. (Cited on page 20.)

[Koolen 2012] T. Koolen, T. De Boer, J. Rebula, A. Goswami and J. Pratt. *Capturability-based analysis and control of legged locomotion, Part 1: Theory and application to three simple gait models.* The International Journal of Robotics Research, vol. 31, no. 9, pages 1094–1113, 2012. (Cited on page 58.)

[Langson 2004] W. Langson, I. Chryssochoos, S. Raković and D. Q. Mayne. *Robust model predictive control using tubes.* Automatica, vol. 40, no. 1, pages 125–133, 2004. (Cited on page 59.)

[Lee 2012] S.-H. Lee and A. Goswami. *A momentum-based balance controller for humanoid robots on non-level and non-stationary ground.* Autonomous Robots, vol. 33, no. 4, pages 399–414, 2012. (Cited on page 7.)

[Li 2013] C. Li, T. Zhang and D. I. Goldman. *A terradynamics of legged locomotion on granular media.* science, vol. 339, no. 6126, pages 1408–1412, 2013. (Cited on page 10.)

[Mayne 2000] D. Q. Mayne, J. B. Rawlings, C. V. Rao and P. O. Scokaert. *Constrained model predictive control: Stability and optimality.* Automatica, vol. 36, no. 6, pages 789–814, 2000. (Cited on page 55.)

[Mayne 2005] D. Q. Mayne, M. M. Seron and S. Raković. *Robust model predictive control of constrained linear systems with bounded disturbances.* Automatica, vol. 41, no. 2, pages 219–224, 2005. (Cited on pages 2, 62, and 67.)

[Mifsud 2017] A. Mifsud. *Estimating and stabilizing the status of a combining humanoid robot*. These, Institut national polytechnique de Toulouse (INPT), 2017. (Cited on page 12.)

[Morisawa 2012] M. Morisawa, S. Kajita, F. Kanehiro, K. Kaneko, K. Miura and K. Yokoi. *Balance control based on capture point error compensation for biped walking on uneven terrain*. In IEEE-RAS International Conference on Humanoid Robots (Humanoids), pages 734–740, 2012. (Cited on pages 11, 40, and 52.)

[Nakaoka 2011] S. Nakaoka, K. Miura, M. Morisawa, F. Kanehiro, K. Kaneko, S. Kajita and K. Yokoi. *Toward the use of humanoid robots as assemblies of content technologies*. Synthesiology English edition, vol. 4, no. 2, pages 87–98, 2011. (Cited on page 1.)

[Ogata 1995] K. Ogata. Discrete-time control systems, volume 8. Prentice-Hall Englewood Cliffs, NJ, 1995. (Cited on pages 13 and 32.)

[Okada 2006] K. Okada, M. Kojima, Y. Sagawa, T. Ichino, K. Sato and M. Inaba. *Vision based behavior verification system of humanoid robot for daily environment tasks*. In IEEE-RAS International Conference on Humanoid Robots, pages 7–12, 2006. (Cited on page 10.)

[Pandey 2014] A. K. Pandey, R. Gelin, R. Alami, R. Viry, A. Buendia, R. Meertens, M. Chetouani, L. Devillers, M. Tahon, D. Filliat*et al.* *Romeo2 project: Humanoid robot assistant and companion for everyday life: I. situation assessment for social intelligence*. 2014. (Cited on page 1.)

[Pratt 2002] J. Pratt, B. Krupp and C. Morse. *Series elastic actuators for high fidelity force control*. Industrial Robot: An International Journal, vol. 29, no. 3, pages 234–241, 2002. (Cited on page 10.)

[Pratt 2006] J. Pratt, J. Carff, S. Drakunov and A. Goswami. *Capture point: A step toward humanoid push recovery*. In IEEE-RAS International Conference on Humanoid Robots (Humanoids), pages 200–207, 2006. (Cited on page 58.)

[Pucci 2017] D. Pucci, S. Traversaro and F. Nori. *Momentum control of an underactuated flying humanoid robot*. IEEE Robotics and Automation Letters (RA-L), vol. 3, no. 1, pages 195–202, 2017. (Cited on page 5.)

[Rakovic 2005] S. V. Rakovic, E. C. Kerrigan, K. I. Kouramas and D. Q. Mayne. *Invariant approximations of the minimal robust positively invariant set*. IEEE Transactions on Automatic Control, vol. 50, no. 3, pages 406–410, 2005. (Cited on pages 21, 26, 27, and 29.)

[Ramos 2015] O. Ramos, N. Mansard, O. Stasse, S. Hak, L. Saab and C. Benazeth. *Dynamic whole body motion generation for the dance of a humanoid robot*. IEEE Robotics & Automation Magazine (RAM), 2015. (Cited on page 1.)

[Sardain 2004] P. Sardain and G. Bessonnet. *Forces acting on a biped robot. Center of pressure-zero moment point*. IEEE Transactions on Systems, Man, and Cybernetics-Part A: Systems and Humans, vol. 34, no. 5, pages 630–637, 2004. (Cited on page 6.)

[Schneider 1993] R. Schneider. Convex bodies: The brunn-minkowski theory. Encyclopedia of Mathematics and its Applications. Cambridge University Press, 1993. (Cited on page 21.)

[Scianca 2019] N. Scianca, D. De Simone, L. Lanari and G. Oriolo. *MPC for Humanoid Gait Generation: Stability and Feasibility.* IEEE Transactions on Robotics, 2019. (Cited on page 59.)

[Semini 2011] C. Semini, N. G. Tsagarakis, E. Guglielmino, M. Focchi, F. Cannella and D. G. Caldwell. *Design of HyQ–a hydraulically and electrically actuated quadruped robot.* Proceedings of the Institution of Mechanical Engineers, Part I: Journal of Systems and Control Engineering, vol. 225, no. 6, pages 831–849, 2011. (Cited on pages 10 and 11.)

[Serra 2016] D. Serra, C. Brasseur, A. Sherikov, D. Dimitrov and P.-B. Wieber. *A Newton method with always feasible iterates for Nonlinear Model Predictive Control of walking in a multi-contact situation.* In IEEE-RAS International Conference on Humanoid Robots (Humanoids), pages 932–937, 2016. (Cited on page 12.)

[Sherikov 2014] A. Sherikov, D. Dimitrov and P.-B. Wieber. *Whole body motion controller with long-term balance constraints.* In IEEE-RAS International Conference on Humanoid Robots (Humanoids), pages 444–450, 2014. (Cited on page 58.)

[Sherikov 2015] A. Sherikov, D. Dimitrov and P.-B. Wieber. *Balancing a humanoid robot with a prioritized contact force distribution.* In IEEE-RAS International Conference on Humanoid Robots (Humanoids), pages 223–228, 2015. (Cited on pages 5 and 12.)

[Sherikov 2016] A. Sherikov. *Balance preservation and task prioritization in whole body motion control of humanoid robots.* PhD thesis, Université Grenoble Alpes, 2016. (Cited on pages 5 and 7.)

[Smaldone 2019] F. M. Smaldone, N. Scianca, V. Modugno, L. Lanari and G. Oriolo. *Gait Generation using Intrinsically Stable MPC in the Presence of Persistent Disturbances.* In IEEE-RAS International Conference on Humanoid Robots (Humanoids), pages 682–687, 2019. (Cited on page 48.)

[Song 2015] S. Song, J. Kim and K. Yamane. *Development of a bipedal robot that walks like an animation character.* In IEEE International Conference on Robotics and Automation (ICRA), pages 3596–3602, 2015. (Cited on page 55.)

[Sugihara 2002] T. Sugihara and Y. Nakamura. *Whole-body cooperative balancing of humanoid robot using cog jacobian.* In IEEE/RSJ international conference on intelligent robots and systems, volume 3, pages 2575–2580, 2002. (Cited on page 7.)

[Sugihara 2009] T. Sugihara. *Standing stabilizability and stepping maneuver in planar bipedalism based on the best COM-ZMP regulator.* In IEEE International Conference on Robotics and Automation (ICRA), pages 1966–1971, 2009. (Cited on pages 40 and 72.)

[Takenaka 2009] T. Takenaka, T. Matsumoto and T. Yoshiike. *Real time motion generation and control for biped robot-1 st report: Walking gait pattern generation.* In IEEE/RSJ International Conference on Intelligent Robots and Systems, pages 1084–1091, 2009. (Cited on page 7.)

[Villa 2017] N. A. Villa and P.-B. Wieber. *Model predictive control of biped walking with bounded uncertainties.* In IEEE-RAS International Conference on Humanoid Robotics (Humanoids), pages 836–841, 2017. (Not cited.)

[Villa 2019] N. A. Villa, J. Englsberger and P.-B. Wieber. *Sensitivity of legged balance control to uncertainties and sampling period*. IEEE Robotics and Automation Letters (RA-L), vol. 4, no. 4, pages 3665–3670, 2019. (Cited on page 45.)

[Westervelt 2018] E. R. Westervelt, J. W. Grizzle, C. Chevallereau, J. H. Choi and B. Morris. Feedback control of dynamic bipedal robot locomotion. CRC press, 2018. (Cited on page 5.)

[Wieber 2006a] P.-B. Wieber. *Holonomy and nonholonomy in the dynamics of articulated motion*. In Fast motions in biomechanics and robotics, pages 411–425. Springer, 2006. (Cited on pages 4 and 6.)

[Wieber 2006b] P.-B. Wieber. *Trajectory free linear model predictive control for stable walking in the presence of strong perturbations*. In IEEE-RAS International Conference on Humanoid Robots, pages 137–142, 2006. (Cited on pages 7 and 62.)

[Wieber 2016] P.-B. Wieber, R. Tedrake and S. Kuindersma. *Modelling and control of legged robots*. In Springer Handbook of Robotics, pages 1203–1234. Springer, 2016. (Cited on pages 4, 5, 6, 7, 8, and 14.)

[Winter 1998] D. A. Winter, A. E. Patla, F. Prince, M. Ishac and K. Gielo-Perczak. *Stiffness control of balance in quiet standing*. Journal of neurophysiology, vol. 80, no. 3, pages 1211–1221, 1998. (Cited on page 7.)

[Xinjilefu 2015] X. Xinjilefu. *State estimation for humanoid robots*. PhD thesis, Carnegie-Mellon Univ. Pittsburgh PA Robotics Inst, 2015. (Cited on page 12.)